Single Electron Probes of Fractional Quantum Hall States

Amir Yacoby Vivek Venkatachalam

Single Electron Probes of Fractional Quantum Hall States

Abstract

When electrons are confined to a two dimensional layer with a perpendicular applied magnetic field, such that the ratio of electrons to flux quanta (ν) is a small integer or simple rational value, these electrons condense into remarkable new phases of matter that are strikingly different from the metallic electron gas that exists in the absence of a magnetic field. These phases, called integer or fractional quantum Hall (IQH or FQH) states, appear to be conventional insulators in their bulk, but behave as a dissipationless metal along their edge. Furthermore, electrical measurements of such a system are largely insensitive to the detailed geometry of how the system is contacted or even how large the system is... only the order in which contacts are made appears to matter. This insensitivity to local geometry has since appeared in a number of other two and three dimensional systems, earning them the classification of "topological insulators" and prompting an enormous experimental and theoretical effort to understand their properties and perhaps manipulate these properties to create robust quantum information processors. The focus of this thesis will be two experiments designed to elucidate remarkable properties of the metallic edge and insulating bulk of certain FQH systems.

To study such systems, we can use mesoscopic devices known as single electron transistors (SETs). These devices operate by watching single electrons hop into and out of a confining box and into a nearby wire (for measurement). If it is initially unfavorable for an electron to leave the box, it can be made favorable by bringing another charge nearby, modifying the energy of the confined electron and pushing it out of the box and into the nearby wire. In this way, the SET can measure nearby charges. Alternatively, we can heat up the nearby wire to make it easier for electrons to enter and leave the box. In this way, the SET is a sensitive thermometer.

First, by operating the SET as an electrometer, we measure the local charge of the $\nu = 5/2$ FQH state. An immediate consequence of measuring fractionally quantized conductance plateaus is that the charge of local excitations should be a fraction of e, the charge of an electron. The simplest charge that would be expected at $\nu = 5/2$ would $e/2$. However, if the charged particles that condense into the $\nu = 5/2$ FQH state are

paired, the expected local charge becomes $e/4$. By watching these local charges being added to compressible puddles at $\nu = 5/2$ and $\nu = 7/3$, we find that the local charge at $\nu = 5/2$ is indeed $e/4$, indicating that objects of charge e are pairing to form the ground state of the system. This has implications for the future possibility of detecting non-Abelian braiding statistics in this state, and is described in detail in Chapter 2.

By further monitoring how eagerly these $e/4$ particles enter puddles as we increase the temperature, we can attempt to identify the presence of some excess entropy related to an unconventional degeneracy of their ground state. Such an entropy would be expected if the $\nu = 5/2$ state exhibited non-Abelian braiding statistics. Progress on these experiments and prospects for building a quantum computer are presented in Chapter 3.

Next, by operating the SET as a thermometer, we monitor heat flow along the compressible edge and through the bulk of IQH and FQH states. As an edge is heated and charge on that edge is swept downstream by the external magnetic field, we expect that charge to carry the injected energy in the same downstream direction. However, for certain FQH states, this is not the case. By heating an edge with a quantum point contact (QPC) and monitoring the heat transported upstream and downstream, we find that heat can be transported upstream when the edge contains structure related to $\nu = 2/3$ FQH physics. Surprisingly, this can be present even when the bulk is in a conventional insulating (IQH) state. Additionally, we unexpectedly find that the $\nu = 1$ bulk is capable of transporting heat, while the $\nu = 2$ and $\nu = 3$ bulk are not. These experiments are presented in Chapter 4.

Finally, in Chapter 5, we describe preliminary work on a very different type of topological material, the quantum spin Hall (QSH) insulator. Here, the spin of electrons takes the place of the external magnetic field, creating edge states that propagate in both directions. Each of these edges behaves as an ideal one-dimensional mode, with predicted resistance h/e^2. By creating well-defined regions where these modes can exist, we identify and characterize the conductance associated with topological edges.

Contents

1 Fractionally Charged Quasiparticles **1**

1.1 Why is charge quantized? 2
1.2 The Fractional Quantum Hall Effect 2
1.3 Laughlin's Case for Fractionally Charged Quasiparticles 4
1.4 Localized States in the Quantum Hall Effect 6
1.5 Measuring Localized Fractional Charges 11

2 Local Charge of the $\nu = 5/2$ Quantum Hall State **17**

2.1 Experiment and Data 18
2.2 Charging Model 23
2.3 Molecular Beam Epitaxy Information 26
2.4 Supplement: Correlation Extraction Procedure 26

3 Local Probes of Non-Abelian Statistics at $\nu = 5/2$ **32**

3.1 Measuring Entropy via Chemical Potential 33
3.2 Directly Measuring $\mu(T)$ 34
3.3 Measuring $\mu(T)$ locally 34
3.4 Topological Quantum Computing With Disorder Localized Quasiparticles 36

4 Local Thermometry of Neutral Modes on the Quantum Hall Edge **42**

4.1 Charge Transport 43
4.2 Heat Transport 47
4.3 Chemical Potential Measurements and Thermometry 53
4.4 Power carried by Non-Equilibrium Edges 60
4.5 Bulk Heat Transport 65

4.6 The Fractional Quantum Hall Edge at $\nu = 1$ 75
4.7 Length Dependence of R_L 77
4.8 Molecular Beam Epitaxy Information 78

5 The Quantum Spin Hall Effect in HgTe Quantum Wells **80**
5.1 Outline of previous work 81
5.2 Measuring Quantum Spin Hall Electrical Resistances 82
5.3 Characterizing Fluctuations 85

A Fabrication Procedures **91**
A.1 Photolithography 91
A.2 Electron Beam Lithography 93
A.3 Removing Material (Etching, Polishing, and Milling) 94
A.4 Metal Evaporation 96

B Fridge Wiring **97**

C Special Measure **100**
C.1 Pseudocode 101

References **103**

Author List

Chapter 2: Text and figures prepared by Vivek Venkatachalam. Manuscript published as

Vivek Venkatachalam, Amir Yacoby, Loren Pfeiffer, and Ken West. Local charge of the $\nu = 5/2$ fractional quantum Hall state. *Nature*, 469(7329):185–188, January 2011. ISSN 0028-0836. URL http://dx.doi.org/10.1038/nature09680.

Chapter 4: Text and figures prepared by Vivek Venkatachalam and Sean Hart. A modified version will appear as an article in *Nature Physics*, and the current version is available as

Vivek Venkatachalam, Sean Hart, Loren Pfeiffer, Ken West, and Amir Yacoby. Local thermometry of neutral modes on the quantum Hall edge, Feb. 2012. URL http://arxiv.org/abs/1202.6681.

Chapter 5: Data obtained by: Vivek Venkatachalam, Sean Hart, Timo Wagner, Hechen Ren

Listing of figures

1.2.1 The Fractional Quantum Hall Effect 3
1.3.1 Laughlin's Argument 4
1.4.1 Electrostatics Governs Localization (Schematic) 9
1.4.2 Seeing Disorder in a Hall Trace 13
1.4.3 SEM of an Aluminum SET with Transport Characteristic 14
1.4.4 Electrostatics Governs Localization (Experiment) 15
1.5.1 Charge Comparison Schematic 16

2.1.1 Filling puddles with fractional charge 19
2.1.2 Incompressibility and localized states at 5/2 21
2.1.3 Comparison of spectra at 5/2 and 7/3 22
2.2.1 Summary of Charging Data and Model 24
2.3.1 Wafer Structure: LP 9-21-07.1 27
2.4.1 Sample Incompressibility Data 28
2.4.2 Charge Extraction Details (Example 1) 29
2.4.3 Charge Extraction Details (Example 2) 30
2.4.4 Histogram for uncorrelated charge comparison 31

3.3.1 Temperature Evolution of Charging Spectrum (schematic) 35
3.3.2 Comparison of Backgated Samples in Transport Quality 36
3.3.3 Temperature Evolution of Charging Spectrum (Preliminary Data) . . 37
3.4.1 Control Space for a Topological Qubit 39
3.4.2 Sketch of a Disorder-Based Quantum Computer 41

4.1.1 Heat Transport Device 45
4.1.2 Global and Local Hall Traces 46

4.2.1 Heat Transport Data 48
4.2.2 Edge Structure Schematic 51
4.3.1 Quantum Dot Zero Bias Variation 54
4.3.2 Coulomb Blockade Calibration 56
4.3.3 Coulomb Blockade Fits 57
4.3.4 Coulomb Blockade Calibration 59
4.4.1 Non Equilibrium Fermi Occupations 63
4.4.2 Equilibrium Temperatures for Non-uniform Transmission at QPC . . 64
4.5.1 Two Temperature CB Fits 67
4.5.2 Two Temperature Fits versus Injected Power 68
4.5.3 Device with Vertical Heat Barriers 69
4.5.4 Heat Transport Across a Barrier 70
4.5.5 Device with Smaller Deflector 73
4.5.6 Heat Transport with Smaller Deflectors 74
4.6.1 Device with Mesa Edges 75
4.6.2 Heat transport of Sharp Edge 76
4.7.1 Length Dependence of R_L 78
4.8.1 Wafer Structure: LP 11-18-08.1 79

5.1.1 Six Terminal QSH Geometry 83
5.2.1 Growth Structure of HgTe Wafer 84
5.2.2 Schematic of QSH edge devices 87
5.2.3 Observation of QSH Conductance 88
5.2.4 QSH Edge Resistances for eight 2 μm edges 89
5.2.5 QSH Edge Resistances versus Gate voltage 90
5.3.1 QSH Conductance Fluctuations 90

B.1 Fridge Wiring 98
B.2 Coldfinger 99

Dedicated to my parents, for their endless love and support

Acknowledgments

Many people have contributed to the work in this thesis, and many more contributed to work not in it. First and foremost, I thank my advisor, Amir Yacoby. He is fantastically creative and is always looking for slightly offbeat approaches to important problems. Perhaps equally importantly, he has put together one of the most exciting groups of people to work with and one of the best physical environments to do great science.

I was trained to make small things by Jeff Miller (from early in the Harvard incarnation of the Marcus lab), and Basile Verdene (from late in the Weizmann incarnation of the Yacoby group). Most importantly, Basile showed me how to make and measure single electron transistors. He had painstakingly tested many backgated wafers to find the best candidates to study 5/2 physics. Without the groundwork he laid, the local charge measurements would have been impossible.

Sandra Foletti showed me how to make the quantum dots that were eventually used to measure neutral modes, and Gilad Barak taught me a lot of physics that I was supposed to already know. Jens Martin was one of the most accomplished experimentalists I've met, and a huge asset to the lab. He showed me how to run a dilution fridge without breaking it.

The Harvard incarnation of the lab grew quickly, with a great group of new scientists. Hendrik Bluhm, Patrick Maletinsky, Thomas Weitz, Lan Luan, Sungkun Hong, Ben Feldman, Mike Grinolds, Sean Hart, Mikey Shulman, Monica Allen, Beni Krauss, Dan Fudenberg, and Mallika Randeria have all been great to work with.

Hendrik, a MATLAB guru besides an expert physicist, taught me the importance of versatile measurement software, and now Special Measure (the MATLAB version) is

now being used in several labs around the world. Patrick introduced me to optics and confocal microscopy as best he could. Hopefully I won't have to come to him for help in my future. Both of them provided excellent role models as efficient and enthusiastic researchers. I can't wait to see what exciting things come out of their new labs.

The heat transport measurements would never have been done without the help of Sean Hart, one of the most talented students I have met. Within two months of arriving in our lab, he had constructed a four channel lockin amplifier using an FPGA we had bought. He then learned how to make and measure devices without being taught (conveniently for me). The experiment had many ups and downs, but it certainly wouldn't have come out so beautifully without his persistent care and attention. Team topology is in excellent hands.

A lot of work has gone into refining the construction of our charge-sensing SETs. In chronological order, this was done by Jonah Waismann, Johannes Nübler, Daniel Fudenberg, Lan Luan, and Mallika Randeria. After a lot of fine tuning, the devices now have more charging energy and higher yield than ever before. Thanks guys!

Johannes, along with Jurgen Smet, showed me how to study microwave-induced physics in 2D electron systems when I visited them in Stuttgart in 2010. Ding Zhang, another student of Jurgen, used our SETs for charge sensing measurements of the $\nu_T = 1$ state in bilayer 2D systems, which he took the time to teach me about when I was visiting.

The last years of my PhD involved starting fresh with an exciting new material (HgTe quantum wells for the quantum spin Hall effect), and I am very thankful to Mathias Mühlbauer from the group of Laurens Molenkamp for taking the time to show me how to process these fragile new toys. I've made several voyages to Würzburg to glean knowledge from him, and he has consistently put aside a lot of time to ensure that I learned all the specialized knowledge he and his group had worked so hard to construct.

I have had the pleasure of working with very talented and responsive growers. Loren Pfeiffer and Ken West made some of the best materials for studying the fractional quantum Hall effect. I am especially thankful for the time Loren took to explain his growth strategies to me, and for always generously inviting me to visit when I was in New Jersey. Ken took the time to teach me how to safely (?) thin wafers down to 50 microns using bromine and methanol, a promising technique to study compressibility of more fragile FQH states. Christoph Brüne, from Würzburg, has generously shared

precious material with us, even when the machines used for growth are often down.

One of the biggest advantages of working at Harvard has been having the Marcus lab downstairs. As a pool of scientific and technical know-how, they have been invaluable. Especially important has been the sharing of fabrication and electron-cooling knowledge back and forth with Doug McClure, Yiming Zhang, Angela Kou, and Willy Chang.

Working in the background, the Yacoby lab has had many talented and efficient assistants, but Carolyn Moore has been especially indispensable in helping me get stuff done (and just get stuff). I owe her a special thank you.

Finally, and most importantly, I thank my parents, Sai and Venkat, my sister Veena, and my wife Jennifer. I couldn't have made it without your love and support.

"Quarks!"

Daniel Tsui

1 Fractionally Charged Quasiparticles

By 1920, it was believed that all electrical charges came in discrete multiples of e, a fundamental unit equal to roughly 1.602×10^{-19} Coulombs. Protons and electrons, the two charged building blocks of all matter, had charges of $+e$ and $-e$, respectively. In 1968, using methods similar to those championed by Rutherford to identify atomic nuclei, experiments at the Stanford Linear Accelerator Center (SLAC) were able to identify internal structure in protons. This structure was soon associated with two quark flavors, which had electrical charges of $2e/3$ and $-e/3$, respectively. These fractionally charged particles were among the most dramatic manifestations of quantum chromodynamics (QCD), a theory that clarified the generality of geometric gauge theories. These quarks, however, are strongly confined within composite particles and have not yet been measured in isolation[1]. There is no evidence to date of any such internal structure for electrons. None the less, electrons won the race to produce measurable fractionally charged particles. How is that possible?

[1] Attempts have been made to create a quark gluon plasma, with no definitive success to date

1.1 Why is charge quantized?

We don't yet know.

Electrical charge is something we measure and something that appears to be conserved. Therefore, it is plausible (but not necessary) by Noether's theorem that charge is the generator of some physical symmetry. This symmetry turns out to be slightly more abstract than the usual space translation or time translation symmetries that we are used to– it corresponds to the freedom to choose an angle $\theta(x) \in [0, 2\pi)$[2] at every point of spacetime. When this spatially varying $U(1)$ symmetry is given to the electron field, another quantum field, $A(x)$, appears in the electron's kinetic energy term: $p \to p + eA(x)$, giving rise to the conventional laws of electricity and magnetism. The value of e here is arbitrary, and is taken to be an experimentally determined input to the Standard Model. However, the value is fixed for all space and time so every electron (quantum of field excitation) has the same charge.

There are, however, other particles. If we assume protons (or quarks) have the same $U(1)$ symmetry[3], the prescription for replacing p with $p + qA(x)$ could be done with q different from e. Charges of πe or $e/4$ are just as valid as e and $-2e/3$. This arbitrariness remains if we consider the fuller electroweak symmetry group $SU(2) \times U(1)$ or even the full standard model symmetry $SU(3) \times SU(2) \times U(1)$.

Dirac had an important observation related to this problem in 1931. He pointed out that if a single magnetic monopole existed with charge φ_0, the electrical charge for all charged particles would necessarily be quantized to integer multiples of h/φ_0 [21]. From the observed rational ratios of particle charges, it seems likely that there exists some symmetry beyond what is explained by the Standard Model [62].

1.2 The Fractional Quantum Hall Effect

In 1982, Tsui, Stormer, and Gossard reported startling behavior of electrons confined to a two dimensional interface between GaAs and $Al_xGa_{1-x}As$ (a two-dimensional electron system or 2DES) [55]. The experiments, carried out at high magnetic field, were designed to probe the extreme quantum limit. This corresponds to the realm where kinetic energy has been removed by the application of a perpendicular magnetic

[2] This is just the phase of a charged particle's wavefunction

[3] The same $\theta(x)$, not a different one

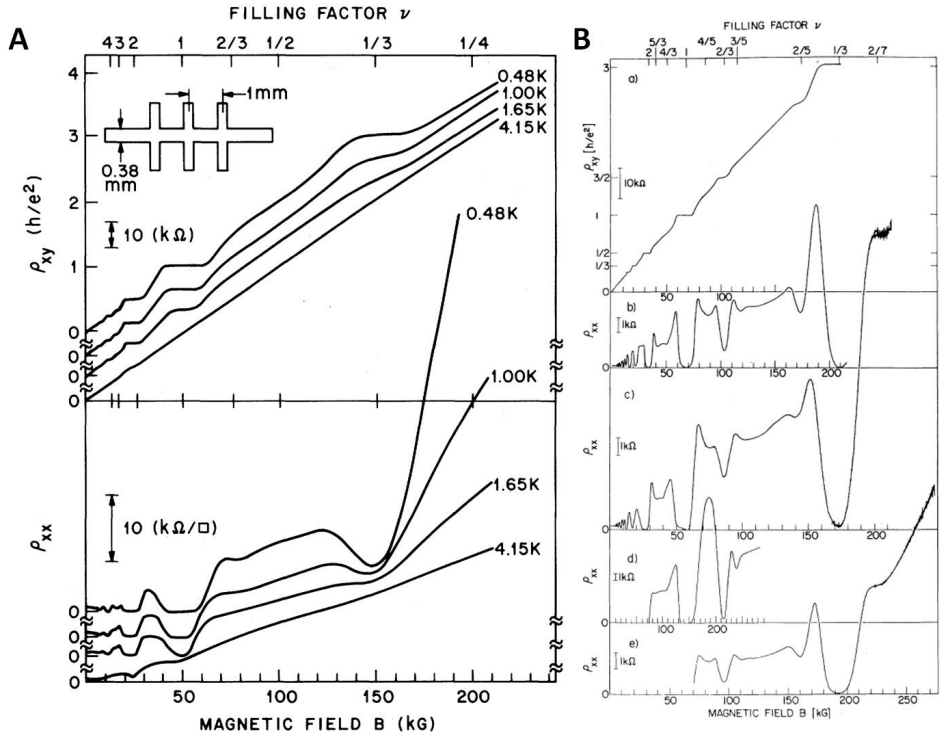

Figure 1.2.1: A) The first reported measurement in 1982 of the $\nu = 1/3$ FQH effect, characterized by $R_{xy} = 3h/e^2$ and $R_{xx} \to 0$. Taken from [55] B) States at 2/5 and 2/3 were advertised almost immediately afterwards, in 1983. It is clear from this data that R_{xx} at 1/3 is vanishing. Taken from [53]

field and Coulomb interactions are stronger than disorder. When the ratio of electrons (areal density n) to flux quanta (areal flux density $B \times e/h$) was near $1/3$, they observed a sharp quantization of the transverse conductance (in units of $\frac{e^2}{h}$)[4] to $\sigma_{xy} = \frac{1}{3}$. Previously, quantized conductivity had only been seen at integer values (in any system). The longitudinal resistance vanished at $\nu = 1/3$, similar to what had been observed at integer plateaus in R_{xy} previously. The original data, along with an improved version from a year later, are presented in Figure 1.2.1.

[4]Electrical conductance has the same units as q_e/φ_0, the ratio of Dirac's fundamental electric and magnetic charges

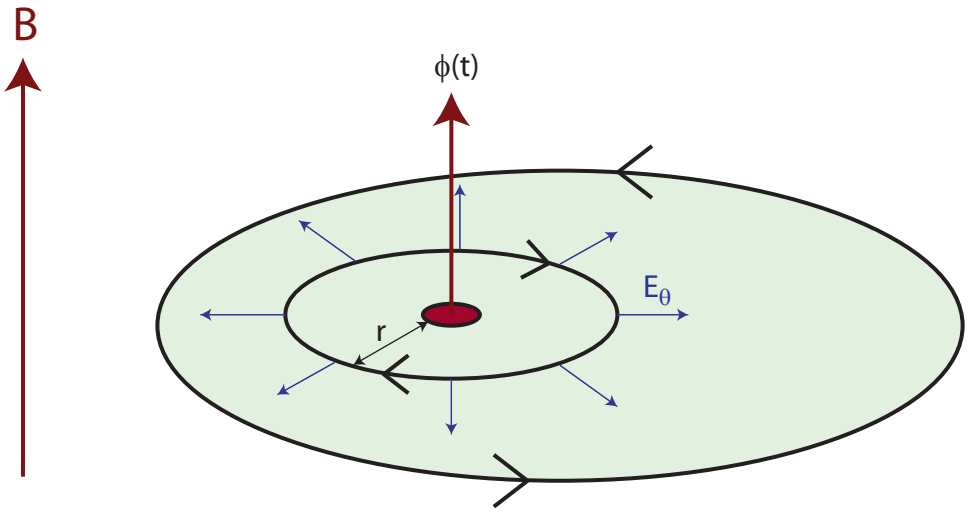

Figure 1.3.1: Adiabatically inserting a flux through a hole in an incompressible quantum Hall fluid moves *ve* charge from the inner boundary to the outer boundary. The flux can be gauged away, leaving an excited state with a local charge of *ve*.

1.3 Laughlin's Case for Fractionally Charged Quasiparticles

Shortly after this discovery, Bob Laughlin pointed out that excitations in this electron system should correspond to fractionally charged particles [39]. His argument is worth understanding to assess the precise implications (and non-implications) of local charge measurements, so we will discuss it carefully.

Consider a two-dimensional electron gas with a small hole in its interior, and imagine slowly threading a solenoid through this hole (see Figure 1.3.1). If the system started in its ground state, and if the flux insertion is slow enough (compared to all the energy splittings in the system), the adiabatic theorem will ensure that the system remains in an eigenstate throughout the process. Outside the immediate neighborhood of the hole, we will assume the system is incompressible with an ideal hall conductivity tensor ($\sigma_{xx} = 0$ $\sigma_{xy} = \nu$).

From Faraday's Law, we know that a changing flux will generate an electric field (see Fig. 1.3.1):

$$E_\theta = \frac{1}{2\pi r}\frac{d\varphi}{dt} = \frac{\varphi_0}{2\pi r}. \tag{1.1}$$

The conductivity tensor allows us to convert this into a radial current:

$$j_r = \sigma_{xy} E_\theta = \nu \frac{e^2}{h} \frac{\varphi_0}{2\pi r}. \tag{1.2}$$

Finally, we can integrate the current to obtain the total amount of charge transferred through any loop containing the hole (consider a circle for simplicity):

$$Q = \int 2\pi r j_r \, dt = \nu \frac{e^2}{h} \frac{h}{e} = \nu e. \tag{1.3}$$

So in this adiabatic process, we have moved a total amount of charge νe from the region with the solenoid to the edge of the sample. However, we may still have a different Hamiltonian from the one we started with, due to the additional gauge field $\boldsymbol{\delta A}(x)$ from the flux tube that is free to affect electrons in the incompressible FQH state. If a quantum mechanical particle with electric charge e is moving near a magnetic field, the spatial rate of phase accumulation is given by the canonical momentum $\mathbf{p} - e\mathbf{A}$. If the particle moves around the hole, the phase picked up is

$$\begin{aligned}
\Phi &= \frac{1}{\hbar} \oint (\mathbf{p} - e\mathbf{A} - e\boldsymbol{\delta A}) \cdot d\mathbf{x} = \frac{1}{\hbar} \oint (\mathbf{p} - e\mathbf{A}) \cdot d\mathbf{x} - \frac{1}{\hbar} \oint e\boldsymbol{\delta A} \cdot d\mathbf{x} \\
&= \frac{1}{\hbar} \oint (\mathbf{p} - e\mathbf{A}) \cdot d\mathbf{x} - \frac{e}{\hbar} \int \boldsymbol{\delta B} \cdot d\mathbf{S} \\
&= \frac{1}{\hbar} \oint (\mathbf{p} - e\mathbf{A}) \cdot d\mathbf{x} - \frac{e}{\hbar} \frac{h}{e} \\
&= \frac{1}{\hbar} \oint (\mathbf{p} - e\mathbf{A}) \cdot d\mathbf{x} - 2\pi \cong \frac{1}{\hbar} \oint (\mathbf{p} - e\mathbf{A}) \cdot d\mathbf{x}.
\end{aligned}$$

If the particle does not move around the hole, the additional phase picked up is 0 ($\int \boldsymbol{\delta B} \cdot d\mathbf{S} = 0$).

Therefore, if we start in a stationary state of the system and proceed with this flux insertion procedure, we will end up in a state where all phase accumulations are identical (and therefore the Hamiltonian is identical) to the original configuration. However, because we have transferred charge from the inner to the outer edge, we cannot be in the same state that we started in. This new stationary state differs from the previous one by the presence of a charge νe at the location of flux insertion, and an equal but opposite fractional charge on the outer boundary. Thus, fractional charges

should be observable when looking both at localized states (in the bulk) and extended states (on the edge).

The value of charge transported by the flux insertion procedure is ve, so a state of charge $2e/3$ would be guaranteed at $\nu = 2/3$ and a state of local charge $5e/2$ would be guaranteed at $\nu = 5/2$. This does not preclude charges of smaller value (such as $e/3$ at $2/3$ and $e/4$ at $5/2$), but it doesn't predict them either. It does predict, however, that the fundamental charge must divide ve.

1.4 Localized States in the Quantum Hall Effect

It may appear that the geometry used in Laughlin's argument is contrived. Must we drill a hole in a quantum Hall system to see fractional charges? Thankfully not. To observe an incompressible quantum Hall state via transport, it suffices to have an incompressible region that forms a connected region in the plane and touches (electrochemically equilibrates with) all ohmic contacts participating in the transport measurement (a classical percolation transition). This incompressible region must remain percolating throughout a quantum Hall plateau. If there is some way for compressible islands to appear within this incompressible sea, those islands should house fractional charges. For now, consider an integer quantum Hall system. Our goal is to understand the roles of disorder and electrostatic screening in the physics of localization. This is carefully discussed in [32].

For a two-dimensional electron moving in a uniform perpendicular magnetic field ($\mathbf{B} = B\hat{\mathbf{z}}$, $\mathbf{A} = \frac{1}{2}rB\hat{\boldsymbol{\theta}}$), the quantum phase accumulated as it travels in its classical circular orbit must be a multiple of 2π:

$$\frac{1}{\hbar}\oint(\mathbf{p} - e\mathbf{A})\cdot d\mathbf{x} = \frac{1}{\hbar}\oint(erB\hat{\boldsymbol{\theta}} - \frac{1}{2}erB\hat{\boldsymbol{\theta}})\cdot\hat{\boldsymbol{\theta}}ds = 2\pi n \tag{1.4}$$

Simplifying this gives the rule $\Phi = BA = n\varphi_0$, where A is the area of the electron's orbit and $\varphi_0 = h/e$ is the magnetic flux quantum, as before. The least energy occurs for $n = 1$, where the electron orbits a single flux quantum. A two dimensional system populated by a single electron would have a large number of possible states for that electron to sit, corresponding to the different fluxes threading the interior [5]. Which flux that electron chooses to orbit is dictated by disorder.

[5] The orbits need not be perfect circles. Nearby circular states with the same energy can easily hybridize to form delocalized states, which can transport current over larger distances.

Disorder in the 2DES introduced by ionized donors, impurities, and crystal defects creates a slowly varying electrostatic potential landscape. The first electron will, in equilibrium, localize to the lowest point in this potential [energy] landscape (see Figure 1.4.1). We will assume that all electron wavefunctions are smaller than the characteristic length scale of the disorder variation, a reasonable assumption if the disorder potential is produced by ionized donors and is sufficiently low-pass filtered when it is imaged on the plane of the 2DES. There are two possible pictures for what happens next.

1.4.1 Localization Without Screening

If we ignore Coulomb interactions between electrons, the next particle will simply find the state with the next lowest electrostatic energy from the bare potential. Disconnected puddles in valleys will slowly get filled this way and eventually the sample switches from a percolating $\nu = 0$ insulator to a percolating $\nu = 1$. At this point, the transverse conductance should increase abruptly from 0 to 1, in units of $\frac{e^2}{h}$.

Additional electrons will be added to potential hills, above the percolation energy, until all states are filled ($\nu = 1$ everywhere). The process will then repeat for the transition from $\nu = 1$ to $\nu = 2$.

There are two important consequences of this single particle picture. First, the transitions between percolating insulating states should be very sharp (as a function of adding electrons). This corresponds to a sharp step in the quantized resistance. Second, the number of localized states in any given region should increase as the areal size of electronic states decreases, or as B is increased: $BA = \varphi_0$ at $\nu = 1$. Monitoring localized states should reveal an increasing number of spatially smaller states at higher magnetic fields.

1.4.2 Localization With Coulomb Screening

Another limit to consider is the situation where each additional electron feels the electrostatic potential from previously added electrons. The second electron added to the 2DES will localize to the flux with the second lowest potential energy, taking into account the electrostatic potential contributed from the first electron. In this way, added electrons will attempt to screen the valleys in the disorder potential. Again, there are two possibilities.

If the number of electrons needed to perfectly screen the disorder potential $\Delta n_{disorder}$ is less than half the number of electrons needed to fill a Landau level $\frac{1}{2}\Delta n = \nu B/(2\varphi_0)$, we will reach a situation where the disorder potential is almost perfectly screened by an inhomogeneous electron distribution. At this point, the added electrons will no longer occupy localized states and will instead begin to occupy extended states, leading to a change from incompressible to compressible behavior in the 2DES.

Eventually, the electrons in some region will fill up all the available fluxes. At that point in space, adding an extra electron will cost kinetic energy or zeeman/exchange energy (in the spinful case). We'll assume that those energies are large compared to disorder and Coulomb energy scales. Therefore, the density in that region will become flatter as added electrons move elsewhere (to compressible regions). As a consequence, the underlying disorder potential will begin to reveal itself in the now incompressible region with $n = n_{max}$. At some point this incompressible region will percolate and additional electrons will once again have to be added to localized states located where the potential landscape originally had hills. Those are the last remaining compressible regions as we approach occupation of every flux ($\nu \equiv 1$). As electrons are added to these hills, the hills become less and less compressible (they get unscreened). Alternatively, by removing electrons (adding holes) to these hills starting from $\nu \equiv 1$, we would be screening the disorder hills.

The other possibility in this Coulomb screening picture is that $\Delta n_{disorder} > \frac{1}{2}\Delta n$. In this limit of strong disorder, perfect screening never occurs and a sharp percolation transition at half filling, similar to the single particle picture, reappears.

Regardless of how strong disorder is, a central prediction of Coulomb screening is that the number of localized states around any given filling factor does not change as the magnetic field is increased. Every disorder valley or hill behaves as a quantum dot or antidot, and the number of particles needed to screen the potential depends only on the charge of those particles, not on the spatial size of any single particle states.

1.4.3 Identifying Localized States from Transport

It is possible to make some observations about the nature of localization by looking at magnetotransport data from a 2DES. Here we will compare a strongly disordered (unscreenable) sample to a cleaner sample where disorder is screened for an

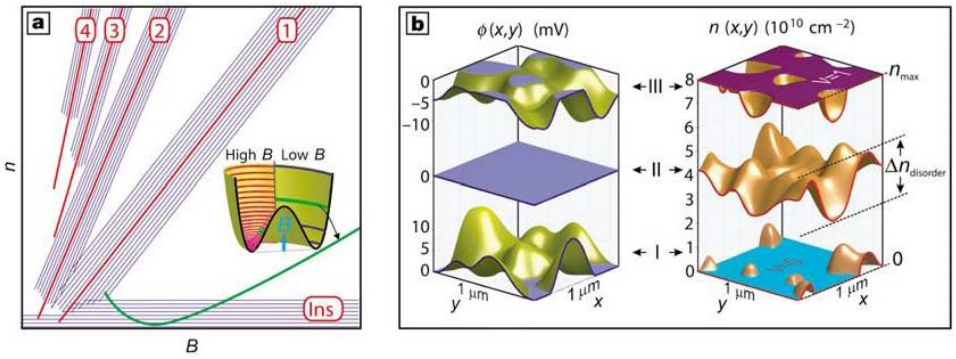

Figure 1.4.1: Theoretical models for localized states. **a**, Schematic illustration of the measured charging lines in the n B plane (blue) compared with a calculated single-particle charging line (green) of a model Mexican hat potential (inset). The single-particle states of the Mexican hat are depicted for low B (blue) and high B (magenta). The specific state that gives rise to the green charging line is marked for both low and high B. Its energy approaches the top of the potential hill in the limit of strong B. This energy is intermediate between the bottom and top of the disorder potential, and therefore leads to a nonquantized asymptotic slope whose value is between $\nu = 0$ and $\nu = 1$. The scatter of potential peak heights in a typical disorder will therefore result in charging lines having arbitrary slopes in the range $\nu = 0 \to 1$. **b**, The density profiles, $n(x, y)$, and electrostatic potential profiles, $\varphi(x, y)$, calculated self-consistently within the Thomas Fermi scheme, for an almost-empty (I), half-full (II) and almost-full Landau level (III), in a typical disorder potential. Following [25], the regions in which the electron density is free to fluctuate are taken as infinitely compressible. Near half-filling, the amplitude of the density fluctuations is $\Delta n_{disorder}$ and the potential is completely screened. Near the bottom of the Landau level ($n = 0$) and its top ($n = n_{max}$) the potential is screened only in compressible pockets, which are surrounded by incompressible regions, marked as $\nu = 0$ or $\nu = 1$. Figure from [32].

appreciable range of filling. Sample A is a CdTe/HgCdTe quantum well grown at the Unversity of Wurzburg with a mobility and density of $\mu = 94,000 \frac{\text{cm}^2}{\text{Vs}}$ and $n = 3.78 \times 10^{11} \text{cm}^{-2}$. Sample B is a GaAs/AlGaAs quantum well grown at Bell Laboratories (Murray Hill) and has a mobility and density of $\mu = 17,800,000 \frac{\text{cm}^2}{\text{Vs}}$ and $n = 1.75 \times 10^{11} \text{cm}^{-2}$. Hall traces for the two samples are presented in Figure 1.4.2.

Above $\nu = 4$, both samples demonstrate sharp percolation transitions, corresponding to strong disorder ($\Delta n_{disorder} > \frac{1}{2}\Delta n$). At higher fields (lower filling factors), the high mobility GaAs 2DES begins to show larger transition regions, corresponding to strong electron correlations favoring condensation into fractional

quantum Hall states. None the less, using the schematic from Figure 1.4.4, we can calculate lower bounds on the number of localized states. Note that in the single particle situation we have $\Delta n_{incompressible} = B/\varphi_0 = n/\nu$. In the case of weaker disorder (nearly full screening), we have $\frac{1}{2}\Delta n_{incompressible} = \Delta n_{disorder}$. In the presence of competing FQH states at low filling factors (generally below $\nu = 4$), this incompressible plateau can get narrowed, leading to the general rule $\frac{1}{2}\Delta n_{incompressible} < \Delta n_{disorder}$, or

$$\Delta n_{disorder} > \frac{1}{2}\Delta n_{incompressible} = \frac{1}{2}\frac{\Delta B_{incompressible}}{B}n = \frac{1}{2}\frac{\Delta \nu_{incompressible}}{\nu}n \qquad (1.5)$$

Using this relation with the $\nu = 2$ plateau of the low mobility sample (blue trace in Figure 1.4.2c), we can say that the density required to perfectly screen the bare disorder is bounded by $\Delta n_{disorder} > \frac{1}{4}n = 0.95 \times 10^{11} cm^{-2}$. From the $\nu = 1$ plateau of the high mobility sample (red trace in Figure 1.4.2c), we can bound the density required for perfect screening by $\Delta n_{disorder} > 0.18n = 0.32 \times 10^{11} cm^{-2}$.

1.4.4 Identifying Localized States via Local Charge Sensing

To determine for certain whether the occupation of a given set of localized states is governed by charging physics, one should attempt to monitor charging behavior as a function of magnetic field. The density of single particle states (per area) is proportional to B, for both integer and fractional quantum Hall states. If the number of states in a fixed density range Δn is independent of field, we can conclude that those states are governed by quantum dot charging physics, as discussed above.

To monitor the charging behavior of any localized states, one needs a local probe capable of sensing (or manipulating) charge. For our purposes, a single electron transistor (SET) is the ideal candidate. By placing and SET near a 2DES, we can collect electric field lines from any charge that moves nearby. If an electron or fractionally charged quasiparticle localizes near the SET, the electric field lines generated by the particle will terminate partially on the SET island. As a result, the electrostatic potential of the island will be slightly modified. Because of the large transconductance of the device, this leads to a dramatic change in current through the device (see Figure 1.4.3).

When these SETs are used to monitor local charging of disorder puddles as the density n and magnetic field B are varied, it is clear that the lines corresponding to single charging events are parallel to lines of constant filling factor in the nB-plane (see Figure 1.4.4). This indicates that the additional density (or chemical potential) required to add a localized state at a given filling factor is independent of the size of single particle states. Such a situation is consistent with the quantum dot picture of localization described above: the additional energy required to add a particle depends only on the number of particles present and not the size of single particle states.

1.5 Measuring Localized Fractional Charges

If we are in a regime where disorder creates quantum dots that can be charged by IQH electrons or FQH quasiparticles (parallel charging lines in the nB-plane), we can hope measure the charge of those quasiparticles. Charge will be added to these quantum dots in such a way as to minimize the free energy

$$F(Q) = \frac{(Q - Q_{ind})^2}{2C_\Sigma} = \frac{(Q - C_{BG}V_{BG})^2}{2C_\Sigma}. \tag{1.6}$$

Here the capacitance to the backgate (C_{BG}) and the backgate voltage (V_{BG}) determine the induced charge on the island (Q_{ind}). The quantum dot tries to match this. If charge is added only in units of e^*, the dot will charge every time $F(ne^*) = F((n+1)e^*)$. Changing e^* results in a different density of charging events (see Figure 1.5.1b,d).

1.5.1 Fractional Charge at $\nu = 1/3$ and $\nu = 2/3$

This strategy for measuring local charge was used successfully to identify $e/3$ quasiparticles at $\nu = 1/3$ and $\nu = 2/3$ [44]. This was accomplished by comparing spectra of electrons charging a disorder dot to spectra of quasiparticles at $\nu = 1/3$ charging the same dot. In these measurements, both the density of charging events and the amplitude of those events displayed the expected $1:3$ ratio (see Figure 1.5.1). The measurement of localized $e/3$ quasiparticles at $\nu = 1/3$ exactly match Laughlin's prediction. At $\nu = 2/3$, Laughlin's argument only guarantees local objects with charge $2e/3$. A smaller charge must divide this, but the existence of such a smaller charge

warrants some explanation. If full electrons are allowed to leave the correlated $\nu = 2/3$ state to charge a disorder-defined quantum dot, then adding a full electron while removing a $2e/3$ particle will result in a charge increase of $e/3$. This smaller charge unit will always be favored because it will result in a smaller free energy for any value of induced charge (see Eqn. 1.6). By relying on charging energy to isolate and measure quasiparticles, this charge-sensing approach will always identify the smallest possible discretization of charge.

1.5.2 Fractional Charge at $\nu = 5/2$

Chapter 2 describes measurements of the local charge at $\nu = 5/2$ by comparison of charging spectra at $\nu = 7/3$ and $\nu = 5/2$. Comparing to $\nu = 7/3$ is ideal because of the similarity of the gaps in these two states. If the percolating incompressible region is actually slightly compressible ($R_{xx} > 0$, for example), the compressible dots within this region can be slightly screened by a capacitance to this compressible bulk. This will alter the spacing of charging events in a manner unrelated to local charge quantization. Choosing states with similar gaps helps control for this effect.

The result of this comparison was the finding that the local charge is quantized in a minimum unit of $e/4$. Like at $\nu = 2/3$, this is half the value guaranteed by the Laughlin argument. Here, however, allowing for electrons to charge the island does not explain why such a halving of the charge may occur.

If a state with a local charge of $e/4$ corresponds adiabatically to a state of the same Hamiltonian with no excess local charge, the flux inserted (in Laughlin's argument) to transport that charge must have been half as much ($\frac{h}{2e}$ instead of $\frac{h}{e}$). This insertion would be trivial (gauge-equivalent to the identity) if all particles obtaining phase by encircling the compressible puddle had charge $2e$ instead of e. The pairing of electrons (or other charge e objects) to form a strongly correlated ground state is the most striking suggestion of a charge $e/4$ measurement at $\nu = 5/2$. Furthermore, several candidate theories describing the state at $\nu = 5/2$ anticipated a local charge of $e/4$. Some of these theories are quite exotic [46], predicting that these $e/4$ quasiparticles can be braided to transform the system between orthogonal ground states. How to identify a ground state degeneracy via charge sensing, and how such a degeneracy may be leverage to make a topological quantum computer is discussed in Chapter 3.

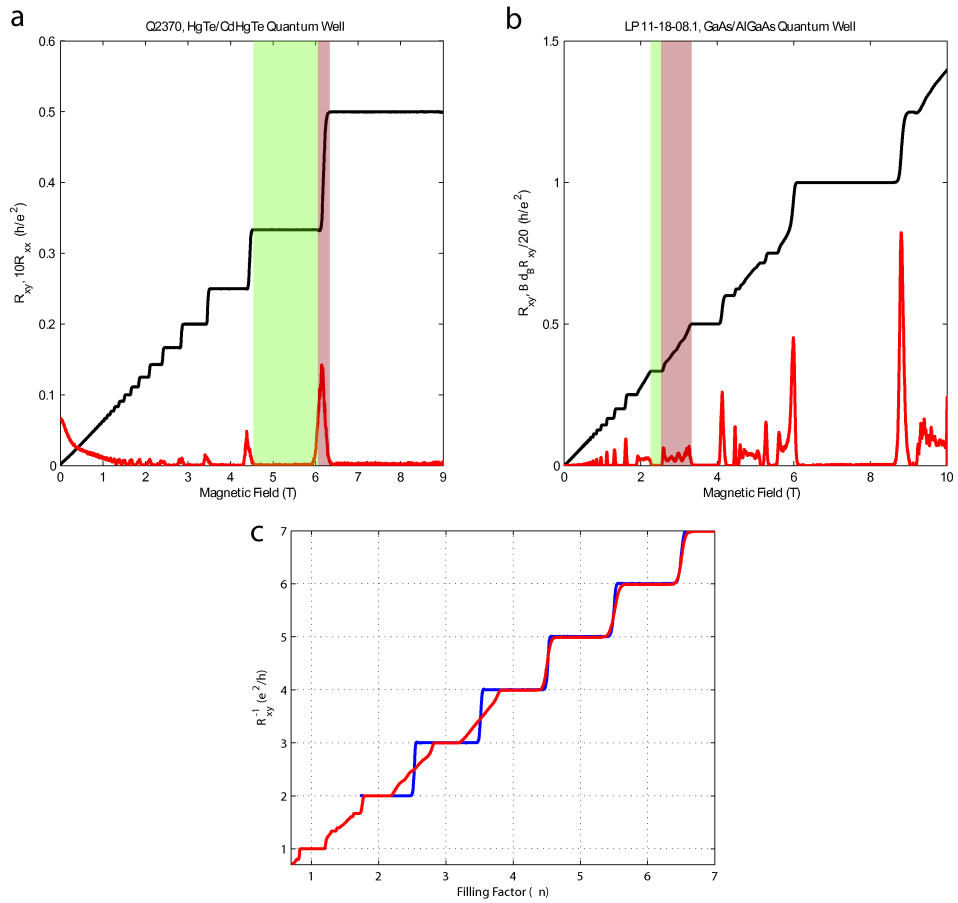

Figure 1.4.2: a, Magnetotransport (R_{xx} and R_{xy}) for a HgTe/CdHgTe 2DES confined in a quantum well, grown at the University of Wurzburg and measured here in a dilution refrigerator at 20 mK. The sample has a measured mobility of $94,000 \frac{\text{cm}^2}{\text{Vs}}$ and density of $3.78 \times 10^{11} \text{cm}^{-2}$. **b,** R_{xy} and its derivative for a high mobility GaAs/AlGaAs quantum well grown by Loren Pfeiffer and Ken West at Bell Laboratories ($\mu = 17,800,000 \frac{\text{cm}^2}{\text{Vs}}$, $n = 1.75 \times 10^{11} \text{cm}^{-2}$). The $\nu = 3$ incompressible quantum Hall state has been highlighted in both traces (green), and the corresponding percolation transition from $\nu = 2$ to $\nu = 3$ has been highlighted in red. A sharp transition indicates that disorder is never completely screened. **c,** The same data, plotted against $\nu = n/B$ for both samples. Above $\nu = 4$, both samples demonstrate imperfect screening. Below $\nu = 4$, the high mobility GaAs sample is compressible for appreciable ranges of ν due to the presence of competing fractional quantum Hall phases.

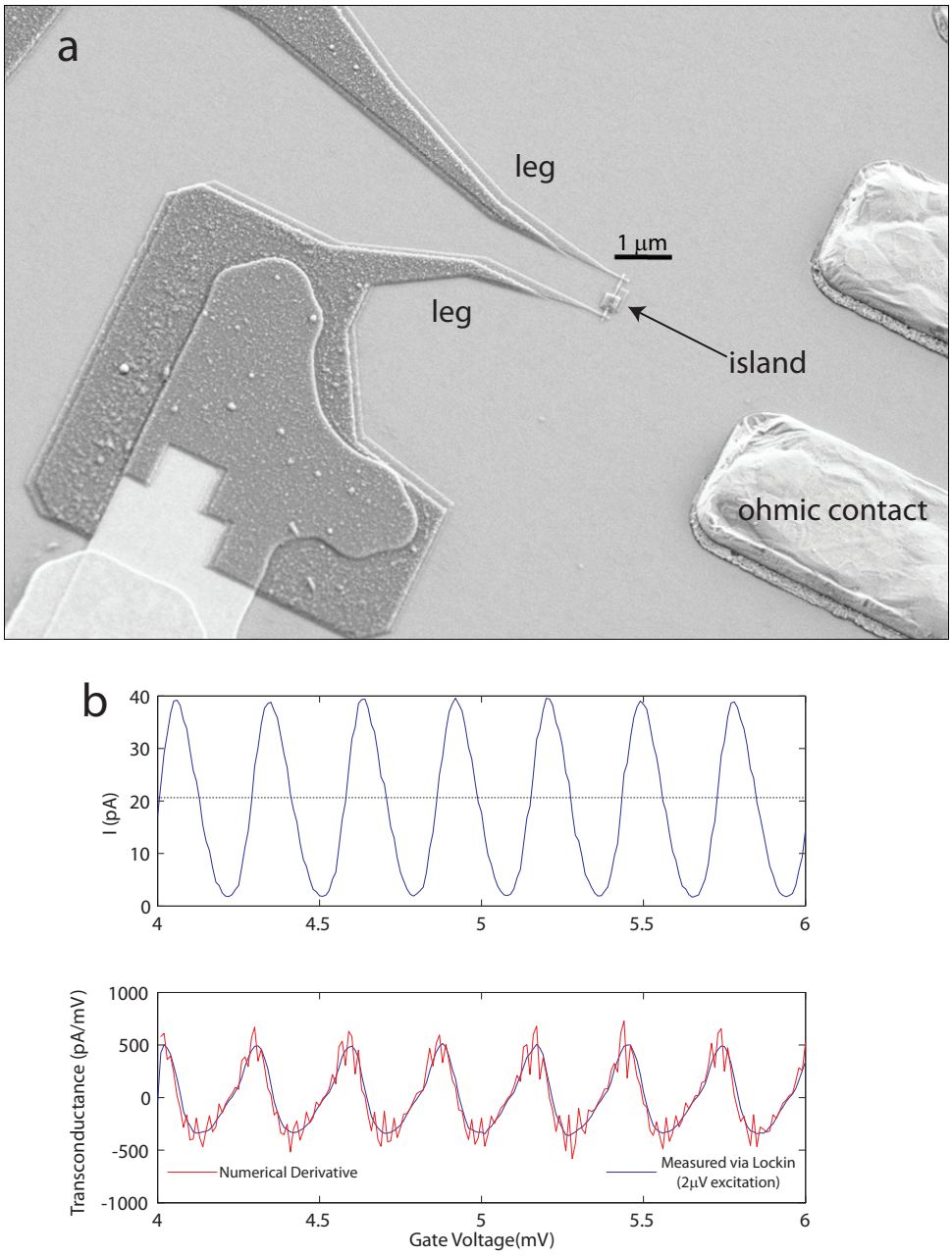

Figure 1.4.3: **a** An SET atop a GaAs/AlGaAs 2DES. Ohmic contacts define the global electrochemical potential of the 2DES, and the island of the SET is capacitively coupled to a local region of the 2DES. If the local electrostatic potential of the electron system changes, the electrostatic potential of the SET island changes as well, resulting in a periodic current response fashion shown in **b**. The large transconductance of the device allows for sensitive measurements of local charges.

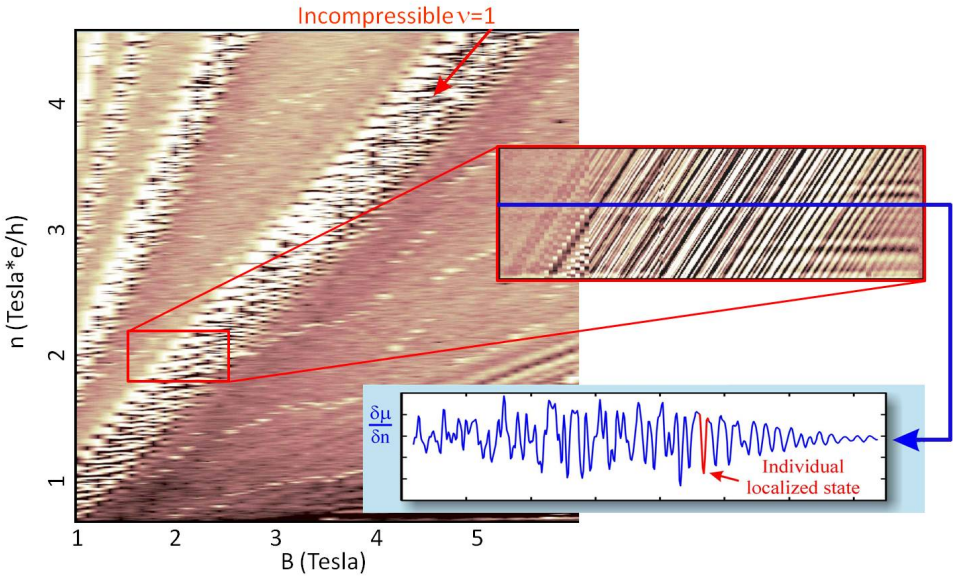

Figure 1.4.4: Measurements of the derivative $\frac{d\mu}{dV_{BG}}$ at an arbitrary position above the 2DES as function of magnetic field (B) and density (n). This derivative is measured with a single electron transistor (SET), which offers a spatial resolution of 100 nm and a voltage sensitivity of $1\,\mu\mathrm{V\,Hz^{-1/2}}$. A measurement over a large range in B and n demonstrating the alternating pattern of incompressible (bright) and compressible (dark) regions. The bright regions correspond to the QH phases of the system. Detailed measurement of the $\nu = 1$ incompressible region reveals a rich fine structure of parallel (black) lines, each representing the charging line of an individual localized state. All charging lines within a certain group have exactly the same slope in the nB-plane. The data in this figure was presented in [32], where further discussion can be found.

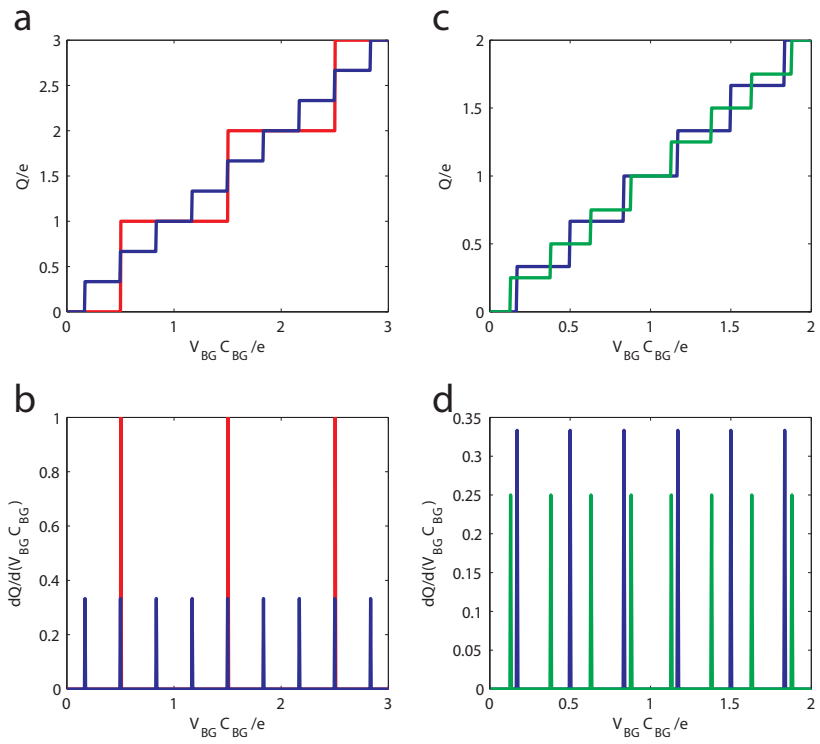

Figure 1.5.1: As a gate is swept and charge is induced on a quantum dot, the dot will increase its charge to minimize its free energy. This will occur in steps governed by the fundamental unit of charge for that dot. **a,b** In the same range of induced charge, we expect three times as many charging events for $e/3$ particles (blue) as for electrons (red). **c,d** The ratio expected for $e/3$ particles versus $e/4$ particles (green), is $4:3$. These ratios are independent of the backgate capacitance C_{BG}. Note that another measure of relative charge can be obtained by analyzing the heights of the jumps (amplitudes in panels b and d). In practice, this is more challenging.

2

Local Charge of the $\nu = 5/2$ Quantum Hall State

When a two-dimensional electron system (2DES) is subject to a strong perpendicular magnetic field, the physics that emerges is controlled by interelectron Coulomb interactions. If the 2DES is tuned such that the ratio of electrons to magnetic flux quanta in the system (ν) is near certain rational values, the electrons condense into so-called fractional quantum Hall (FQH) phases [27]. These strongly-correlated states are gapped and incompressible in the bulk of the sample, but metallic and compressible along the sample boundary, allowing current to flow around the perimeter in such a way that the transverse conductance is precisely quantized to $G_{xy} = \nu(e^2/h)$. Additionally, the electronic correlations encoded in FQH states give rise to local excitations with a fraction of an electron charge and braiding statistics that fall outside the conventional classification of bosonic or fermionic. The state at $\nu = \frac{5}{2}$, unlike its conventional odd-denominator relatives, is predicted to have the additional property that particle interchange can evolve the system adiabatically between orthogonal ground states [46]. This property, dubbed non-abelian braiding statistics,

has been proposed as the basis for a topological quantum computer that would be insensitive to environmental decoherence [19, 47, 57, 58].

One necessary (but insufficient) condition for exotic braiding statistics at $\nu = \frac{5}{2}$ is for the ground state to support local excitations with a charge of $e^*_{5/2} = e/4$, where e is the charge of an electron [46]. Though a charge of $e/4$ had previously been measured using shot noise techniques [22], more recent data from the same group [23] suggest that the value of the measured charge changes continuously as the point contact conductance and temperature are varied, reaching an inferred charge of unity in the weak and strong tunneling limits. Unexpected charges have also been reported for the more conventional fractions at $1/3$, $2/3$, and $7/3$ [10, 23]. Moreover, DC conductance measurements in the weak tunneling regime [50] suggest a quasiparticle charge of $e^*_{5/2} = 0.17e$, in stark contrast to the shot noise results.

Clearly, a better understanding of the tunneling processes that take place between quantum Hall edges in the quantum point contact is needed in order to interpret the shot noise results. Alternatively, one can employ a thermodynamic approach [44] that probes the quasiparticle charge in the bulk of the sample in order to infer quasiparticle charge. Here we use a single electron transistor as a sensitive electrometer to measure the equilibrium charge distribution in the bulk and its dependence on the average density and magnetic field. Our results provide clear evidence for localized charge $e/4$ quasiparticles at $\nu = 5/2$.

2.1 Experiment and Data

Our measurement employs a fixed single electron transistor (SET) as a gated device capable of sensitively measuring the local incompressibility ($\kappa^{-1} = \frac{\partial \mu}{\partial n}$) of a high-mobility 2DES [31]. The 2DES has a 200 nm deep, 30 nm wide MBE-grown GaAs/AlGaAs quantum well, with symmetric Si δ-doping layers 100 nm on either side. A metallic backgate grown 2 μm below the 2DES allows us to tune the global density, n, in the well over a typical range of $2.3 - 2.5 \times 10^{15}\mathrm{m}^{-2}$, with some variation between samples. The SET is fabricated on top of the sample using standard electron beam lithography and shadow-evaporation techniques (Figure 2.1.1), creating an island with dimensions 500 nm $\times$ 80 nm. All measurements were carried out in a dilution refrigerator with an electron temperature of 20 mK, verified using standard Coulomb

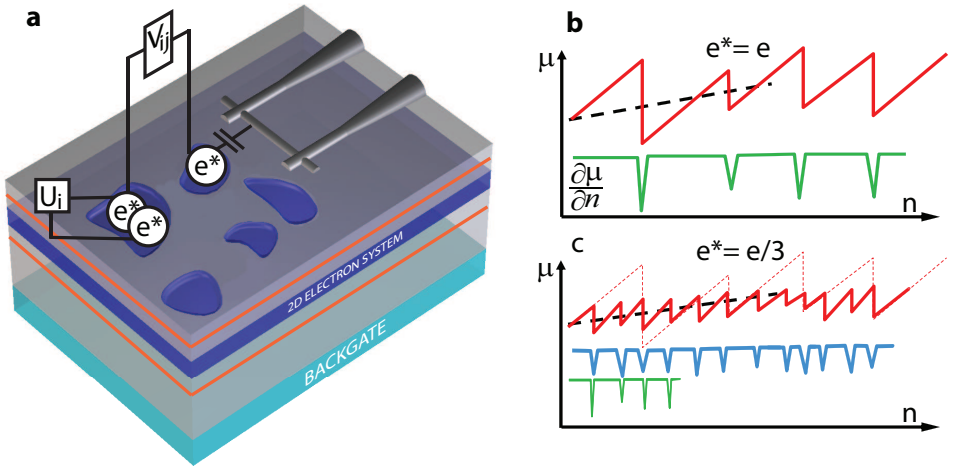

Figure 2.1.1: Filling puddles with fractional charge. **a**, The sample well width is 30 nm, with symmetric Si δ-doping layers 100 nm on either side indicated by orange bands. Donors in these layers create a disorder potential in the 2DES, which produce puddles of localized states when the bulk is tuned to an incompressible, percolating Hall state. These puddles have some charging energy associated with adding electrons (U_i), and possibly some interaction with surrounding puddles (V_{ij}). Incompressibility ($\kappa^{-1} = \frac{\partial \mu}{\partial n}$) is measured using an SET fabricated on the surface. **b,** While the global chemical potential should increase smoothly with density (black dashed line), the local chemical potential will increase in jumps (red line), with charge being added when the global chemical potential aligns with a localized state. **c,** Repeating the charging of an identical puddle with charge $e/3$ objects instead of charge e objects results in three times as many charging events in the same range of global density. Scaling the density axis of the charge e spectrum by $1/3$ and shifting by some amount (green curve) should result in good overlap of the incompressibility spectra.

blockade techniques.

As we adjust the density and magnetic field we expect to see regions of incompressibility when a gap is present, which will only happen precisely when the system is in a QH state. The slope of these incompressible regions in the nB-plane corresponds to the filling factor of the state [32]. Figure 2.1.2 shows incompressibility versus density and magnetic field between $\nu = 2$ and $\nu = 3$, with the two highlighted regions corresponding to FQH states at $\nu = 5/2$ and $\nu = 7/3$.

Additionally, due to the rough disorder potential created by remote donors, we can expect different points in space to develop gaps at different values of the global density. Because of this, we expect a well-developed QH state to have a percolating incompressible region punctured by small compressible puddles which behave as either dots or anti-dots [32]. As the global density is varied, a given compressible puddle will occasionally be populated by quasiparticles or quasiholes of the surrounding incompressible state. This creates a jump in the local chemical potential, $\mu(n)$, and a spike in the local incompressibility $\frac{\partial \mu}{\partial n}$. The magnitude and spacing of these spikes is determined by the charging spectrum of the puddle, which in turn is dictated by the quasiparticle charge in the surrounding incompressible region. Namely, if the quasiparticle charge were reduced by a factor of three for a fixed disorder potential, we should see three times as many compressible spikes as a function of global electron density (Figure 2.1.1 b,c).

This difference in spike frequencies has previously been used to measure the local charge at $\nu = 1/3$ and $\nu = 2/3$ [44]. Unlike shot noise measurements [10], these local compressibility measurements find a quasiparticle charge of $e/3$ at both filling factors. Additionally, because of the spatial resolution afforded by the scanning technique in that measurement, it was possible to establish that the disorder potential landscape does not change as the electron system is tuned between Hall states with comparable gaps. Transport measurements confirm that the gap inferred from activation of R_{xx} minima is comparable for the states at $5/2$ and $7/3$ [16, 20], so we can expect similar potential landscapes for the two states.

Our procedure begins with obtaining charging spectra (incompressibility versus density) at $\nu = 5/2$ and $\nu = 7/3$. Because the gap for these states is comparable, and the disorder potential is not altered as we change the magnetic field or density, we expect the spacing between charging features to reflect the quasiparticle charge in each

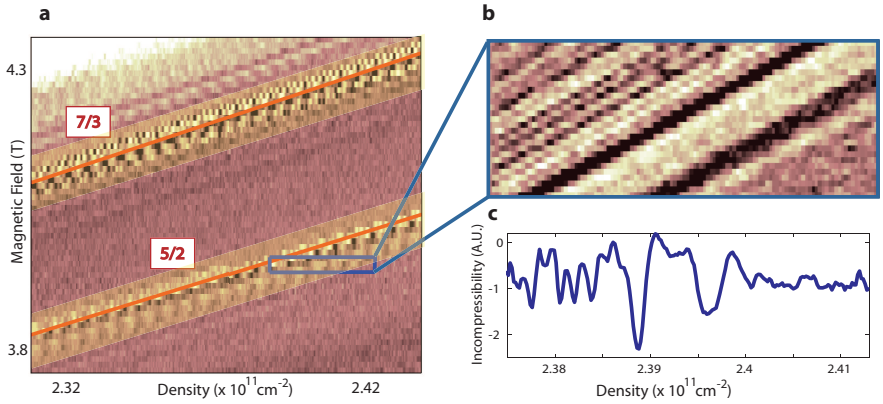

Figure 2.1.2: Incompressibility and localized states at 5/2. **a**, By varying the magnetic field and the backgate voltage (density), we can identify incompressible phases of the 2DES. Our samples show clear incompressible FQH states at 5/2 and 7/3, with the expected slopes in the nB-plane. **b**, Zooming in shows repeatable charging events associated with quasiparticles localizing in puddles under the SET, stable on a timescale of days. **c**, A linecut showing the charging spectrum of any puddles coupled to the SET. Downwards spikes correspond to quasiparticles entering puddles beneath the SET.

state. In the limit of an isolated compressible puddle surrounded by an incompressible fluid, this relationship is particularly simple - if the ratio of local charges between the two spectra is β, the spectra should be identical after one of the density axes is rescaled by a factor of β, and shifted by some amount (Figure 2.1.3a). To proceed, we choose a value of β and stretch one of the spectra by this factor. We then calculate the correlation $\left(\frac{\langle C_1(x)\, C_2(x) \rangle}{\sqrt{\langle C_1(x)^2 \rangle \langle C_2(x)^2 \rangle}} \right)$ between the two spectra as a function of density offset and record the highest value. Finally, we repeat this for many scaling factors to obtain quality-of-fit versus β, as depicted in Figure 2.1.3b.

This procedure was repeated for 20 different disorder configurations, obtained by changing samples, measuring with different SETs, or thermal cycling to change the disorder. A summary of the data is shown in Figure 2.2.1a, with an average over the measured ensemble in Figure 4b. The peak observed at $\beta = 1.31$ suggests a charge ratio of 4:3 between the two states, and a qualitative inspection of spectra overlap (as in Figure 2.1.3a) corroborates this. To determine the significance of the peak value, we repeated our analysis with pairs of spectra from different disorder configurations,

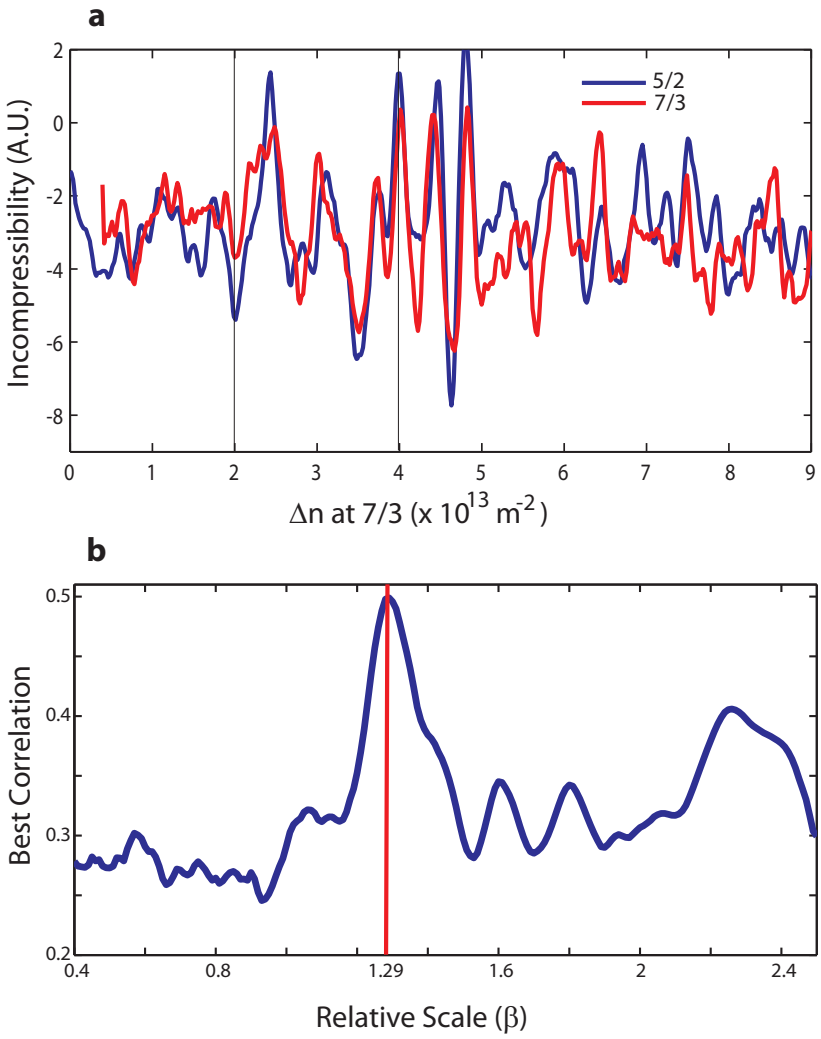

Figure 2.1.3: Comparison of spectra at 5/2 and 7/3. **a**, To determine the charge, we first choose a relative scale between the two density axes (β), and determine the offset between the two spectra that maximizes the cross-covariance. Here the density for the spectrum at 5/2 is scaled up by a factor of 1.29 and shifted to match up with the spectrum at 7/3. The guide lines show the density change required to add 1 electron to an area of 100 nm x 500 nm, approximately the size of our SET. We would therefore expect, very roughly, 3 e/3 charging events in a window this size. **b**, Repeating this for many values of β suggests that a relative scale of 1.29 best describes this data set.

which should be less correlated. For each scale, we characterized the distribution of best correlations with a mean and standard deviation. These, in turn, can be simply converted to the expected mean and standard error for our data (if it were uncorrelated). The 1σ region around the uncorrelated mean is depicted in red in Figure 2.1.3b. Our averaged correlation at $\beta = 1.31$ lies 3.8 standard errors above the uncorrelated mean, corresponding to a one-tailed P-value of 7×10^{-5}. Assuming a charge of $e^*_{7/3} = e/3$, this measured value of β suggests $e^*_{5/2} = (e/3)/(1.31) = 0.254e$, in agreement with the Moore-Read prediction of $e^*_{5/2} = e/4$ [46].

2.2 Charging Model

To better understand why some configurations seem to provide weaker (and sometimes different) measurements of β, it helps to abandon the assumption that we are charging and monitoring single puddles, as well as the assumption that quasiparticles in different puddles do not interact. A free energy for our system that takes these into account is given by

$$F = \frac{e^*}{e}\sum_i (\varepsilon_i - V_{BG})n_i + \frac{1}{2}\left(\frac{e^*}{e}\right)^2 \sum_i U_i n_i(n_i - 1) + \left(\frac{e^*}{e}\right)^2 \sum_{i<j} V_{ij} n_i n_j - \sum_i \Delta \left\lfloor \frac{n_i}{2} \right\rfloor . \tag{2.1}$$

Here, U_i and ε_i are the onsite interaction (self-capacitance) and bare disorder potential for puddle i respectively. V_{ij} is a pairwise interaction, or cross-capacitance, between puddles i and j, and Δ is the energy gained by forming a bound pair of quasiparticles. Both U_i and V_{ij} are energies for a pair of electrons, and need to be scaled by $(e^*/e)^2$ when considering quasiparticles. For now, we will let $\Delta = 0$. We assume that some subset of the puddles is capacitively coupled to and measured by the SET.

To compute charging spectra from this model, we first choose values of U, V, and ε for each puddle from Gaussian distributions. We then discretize e^* into units of $e/3$ or $e/4$ and determine how many units of charge to put in each puddle to minimize the above free energy. This is done for each value of V_{BG} and converted into a charging spectrum. Finally, we can take the resulting spectra and repeat the processing performed on data to obtain summary statistics for comparison. The result, with $\varepsilon = 0 \pm .3U$ and $V_{ij} = 0.3U \pm 0.2U$, is shown in Figure 2.2.1c. Results for other parameter choices in a large range are qualitatively similar, with smaller values of σ_ε and

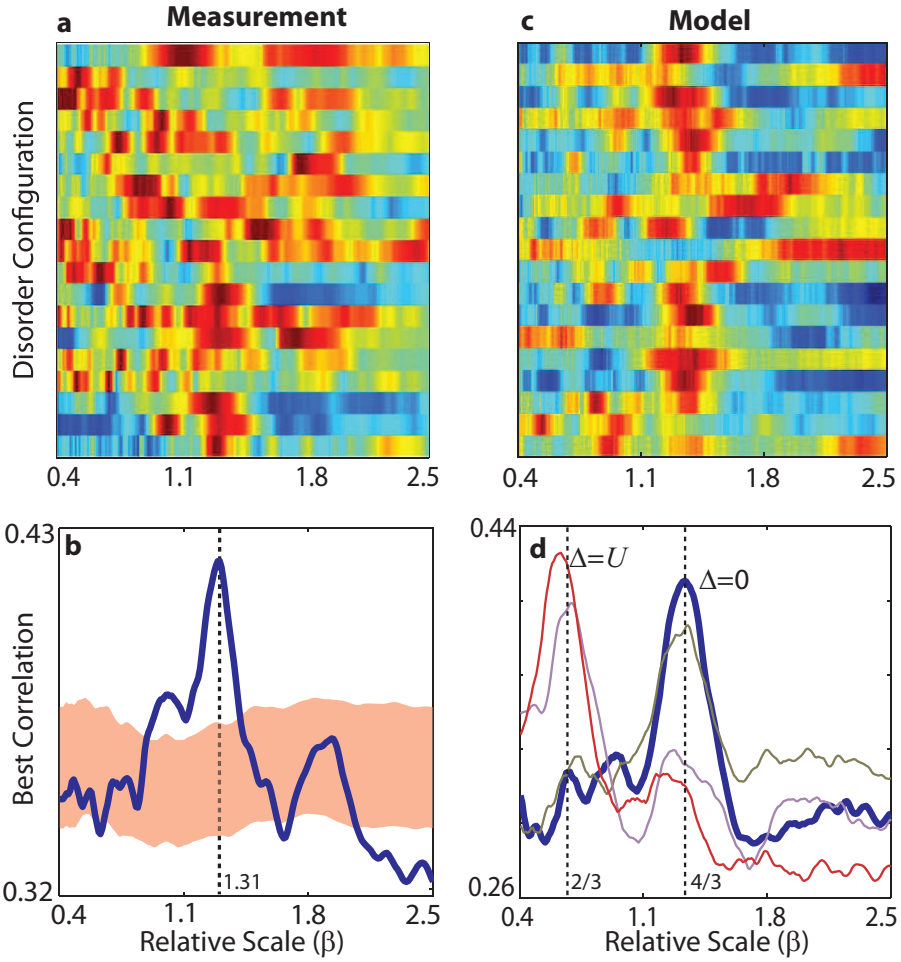

Figure 2.2.1: Summary of Charging Data and Model. **a**, Repeating the measurement over many disorder configurations and samples shows that the peak at $4/3$ is usually present. **b**, Averaging over all measurements yields a clear peak at $\beta = 1.31$, 3.8σ above the uncorrelated background for that scale ($P = 7 \times 10^{-5}$), suggesting a local charge ratio of $4/3$. **c, d**, Running our model with parameters $\varepsilon = 0 \pm .3$, $V = 0.3 \pm 0.2$, and $\Delta_{5/2} = 0.01,\ 0.1$, and 1.0 (all in units of U, the on-site charging energy). We simulated charging of four puddles, of which two were capacitively coupled to the SET.

V_{ij} corresponding to sharper peaks and less spread. As expected, these simulations tell us that both ε and V_{ij} can distort spectra in such a way that the maximum cross-covariance will shift slightly or even dramatically away from $4/3$. Still, we should always expect some weight at $4/3$, and this can be extracted by averaging over disorder configurations (Figure 2.2.1d).

Recently, there has been some suggestion that $e/2$ quasiparticles at the $\nu = 5/2$ edge may be present and relevant to interference measurements [11]. In the context of our model, we can consider the effect weak binding of quasiparticles would have on measured spectra. This binding is parameterized by Δ above, and we only consider the case where pairing affects the $e/4$ quasiparticles. As the strength of pairing is increased relative to the onsite interaction (Figure 2.2.1d), we expect weight to shift from the peak at $4/3$ to a peak at $2/3$ (corresponding to $e/2$ quasiparticles), with considerable weight at $2/3$ even when $\Delta = 0.1\,U$. Our data show no appreciable evidence for a peak at $2/3$, suggesting that the only quasiparticles participating in localization are have charge $e/4$.

These measurements constitute the first direct measurement of incompressibility and localized states at $\nu = 5/2$, and provide an equilibrium probe of the local charge that is insensitive to complications that arise from measurements of transport through nanostructures. The measured value, $e^*_{5/2} = e/4$, indicates that the FQH state at $\nu = 5/2$ demonstrates pairing, in agreement with proposed non-Abelian variational wavefunctions and different from other observed FQH states. Finally, the localization of $e/4$ quasiparticles is essential to the development of interferometers capable of detecting and exploiting these exotic braiding properties [12, 52], and our measurements suggest that e/4 localization does indeed occur in a well-behaved way.

Acknowledgements: We would like to acknowledge Basile Verdene, Jonah Waissman, and Johannes Nübler for technical assistance, and we are grateful to Bertrand Halperin for theoretical discussions. This research has been funded by Microsoft Corporation Project Q.

2.3 Molecular Beam Epitaxy Information

All samples used in this experiment were obtained from the wafer LP 9-21-07.1, grown at Bell Laboratories in Murray Hill, NJ, by Loren Pfeiffer and Kenneth West. Figure 2.3.1 has the details of the growth.

2.4 Supplement: Correlation Extraction Procedure

Here we will walk through the exact procedure used to determine the ratio of charges, using the data sets third and fourth from the bottom of Figure 2.2.1a. We begin with raw spectra from $5/2$ and $7/3$. First, we fit and subtract a quadratic polynomial from each set to account for the general trend in the incompressibility background, unrelated to the charging physics that we are studying here [26].

We then choose a scale, β, to test. We multiply the backgate-values at $5/2$ by β, and if $\beta < 1$ (> 1), we resample the data at $7/3$ ($5/2$) to match the finer gate-spacing of the $5/2$ ($7/3$) set. Next, we choose a gate-voltage offset for the two datasets and restrict each of them to the region where they overlap (for that offset). Finally, we calculate the correlation $\left(\frac{\langle C_1(x)\, C_2(x) \rangle}{\sqrt{\langle C_1(x)^2 \rangle \langle C_2(x)^2 \rangle}} \right)$, where $C_1(x)$ and $C_2(x)$ are the restricted datasets. Figures 2 and 3 show the result for several different choices of β in two data sets. The first column shows correlation as a function of offset and the second column shows how the datasets match up at the best correlation.

In order to determine the significance of these results, we repeated the analysis comparing data sets from different disorder configurations, where correlations were expected to be much weaker. If $C_{5/2}(i)$ is the ith data set at $5/2$, our signal is from comparisons like $\langle C_{5/2}(i)\, C_{7/3}(i) \rangle$. For our background we used comparisons of the form $\langle C_{5/2}(i)\, C_{7/3}(j) \rangle$, $\langle C_{5/2}(i)\, C_{5/2}(j) \rangle$, and $\langle C_{7/3}(i)\, C_{7/3}(j) \rangle$ where $i \neq j$. No significant correlations were measurable in any of these last three sets (though some certainly may be expected simply from disorder statistics). We used 548 distributions to generate the uncorrelated background distribution for each scale. The background distribution for $\beta = 4/3$ is presented in Figure 2.2.1.

9_21_07.1.act.txt

9_21_07.1 - Actual Results
Substrate: WT 18152 #17
As Temp: 331
As Set: 1.402-5
Comments: Amir repeat of 5-1-07.1 with Ga5+7 and more Si
omitting pauses

label	relay	rate	temp	set pt
Al8	1	0.8967	1095.000	19.580
Ga7	2	1.3805	927.000	927.000
Ga5	3	1.4528	947.000	946.000

Layer#	Layer Type	Thickness	Time	Total Time	Al8	Sub (V)	Si (A)	C (A)
1	chgSi chgC As11	0.00	60.00	60.00	---	26.414	7.411	0.009
2*	Ga7Ga5SiAs11	1000.00	352.95	412.95	---	26.411	7.409	0.007
3* (10)	PauseAs11	0.00	100.00	512.95	---	26.407	7.416	0.006
22	chgSi As11	0.00	10.00	4599.45	---	26.405	0.000	0.006
23*	Al8As11	5.30	5.91	4605.36	---	26.413	0.001	0.007
24*	Ga7Ga5As11	11.60	4.09	4609.46	---	26.413	0.001	0.006
25* (766)	PauseAs11	0.00	10.00	4619.46	---	26.411	0.002	0.006
2321	Al8Ga7Ga5As11	2580.00	691.69	20614.76	0.240	26.411	0.002	0.007
2322	Al8As11	19.81	22.09	20636.86	---	26.410	0.001	0.006
2323	Ga7Ga5As11	5.66	2.00	20638.85	---	26.410	0.002	0.007
2324	t-632.8	0.00	10.00	20648.85	---	26.411	0.000	0.006
2325	chgTemp As11	0.00	90.00	20738.85	---	0.014	0.000	0.006
2326	chgTemp As11	0.00	2.00	20740.85	---	15.083	0.000	0.006
2327	chgSi As11	0.00	15.00	20755.85	---	15.080	7.410	0.006
2328	SiAs11	0.00	10.00	20765.85	---	15.078	7.409	0.006
2329	chgSi As11	0.00	10.00	20775.85	---	15.080	0.000	0.004
2330	Ga7Ga5As11	22.64	7.99	20783.84	---	15.078	0.000	0.006
2331	t-432.6	0.00	10.00	20793.84	---	15.078	0.000	0.007
2332	chgTemp As11	0.00	60.00	20853.84	---	32.158	0.000	0.006
2333	startTempAs11	0.00	2.00	20855.84	---	26.409	0.000	0.006
2334	PauseAs11	0.00	120.00	20975.84	---	26.410	0.002	0.006
2335	Al8As11	19.81	22.09	20997.94	---	26.409	0.002	0.006
2336	Al8Ga7Ga5As11	800.00	214.48	21212.41	0.240	26.409	0.001	0.006
2337	Ga7Ga5As11	300.00	105.88	21318.30	---	26.411	0.004	0.006
2338	Al8Ga7Ga5As11	800.00	214.48	21532.77	0.240	26.411	0.002	0.006
2339	t-635.4	0.00	10.00	21542.77	---	26.411	0.003	0.006
2340	Al8As11	19.81	22.09	21564.87	---	26.411	0.002	0.007
2341	Ga7Ga5As11	5.66	2.00	21566.86	---	26.410	0.002	0.008
2342	chgTemp As11	0.00	90.00	21656.86	---	0.015	0.002	0.007
2343	chgTemp As11	0.00	2.00	21658.86	---	15.082	0.002	0.007
2344	chgSi As11	0.00	15.00	21673.86	---	15.083	7.413	0.006
2345	SiAs11	0.00	40.00	21713.86	---	15.079	7.413	0.006
2346	chgSi As11	0.00	10.00	21723.86	---	15.082	0.000	0.006
2347	Ga7Ga5As11	22.64	7.99	21731.85	---	15.080	0.001	0.006
2348	t-430.9	0.00	10.00	21741.85	---	15.080	0.002	0.006
2349	chgTemp As11	0.00	60.00	21801.85	---	32.162	0.002	0.007
2350	startTempAs11	0.00	2.00	21803.85	---	26.410	0.001	0.007
2351	PauseAs11	0.00	120.00	21923.85	---	26.409	0.002	0.006
2352	Al8As11	19.81	22.09	21945.95	---	26.408	0.001	0.007
2353	Al8Ga7Ga5As11	980.00	262.73	22208.68	0.240	26.413	0.002	0.008
2354	Ga7Ga5As11	100.00	35.29	22243.98	---	26.411	0.002	0.008
2355	t-632.8	0.00	10.00	22253.98	---	26.411	0.002	0.008
2356	chgTemp As11	0.00	2.00	22255.98	---	15.085	0.002	0.009
2357	chgSi chgC As11	0.00	60.00	22315.98	---	15.086	0.389	0.399
2358	BeepAs11	0.00	10.00	22325.98	---	15.083	0.389	0.398

total layers: 2358
total time: 22325.98 sec.
total thickness: 28641.2 A.

Figure 2.3.1: Wafer Structure: LP 9-21-07.1

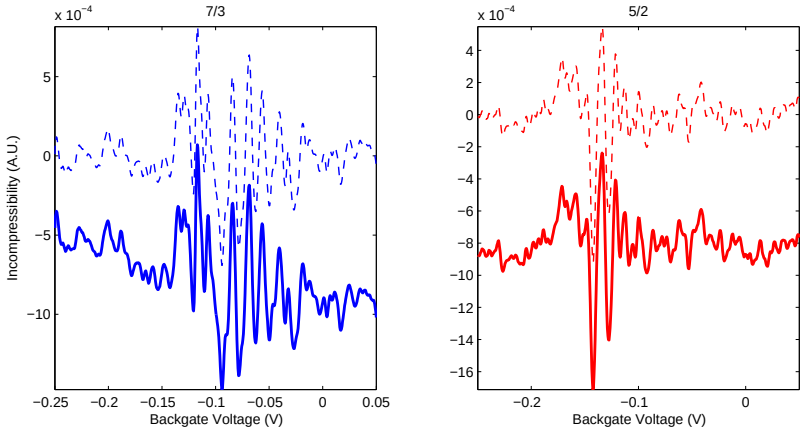

Figure 2.4.1: Incompressibility data from 5/2 and 7/3. The y-scale gives the ratio of SET responses to voltage changes on the backgate and the 2D electron system (ratio of transconductances). Dark lines indicate raw data, and dashed curves are the same data with a quadratic background subtracted.

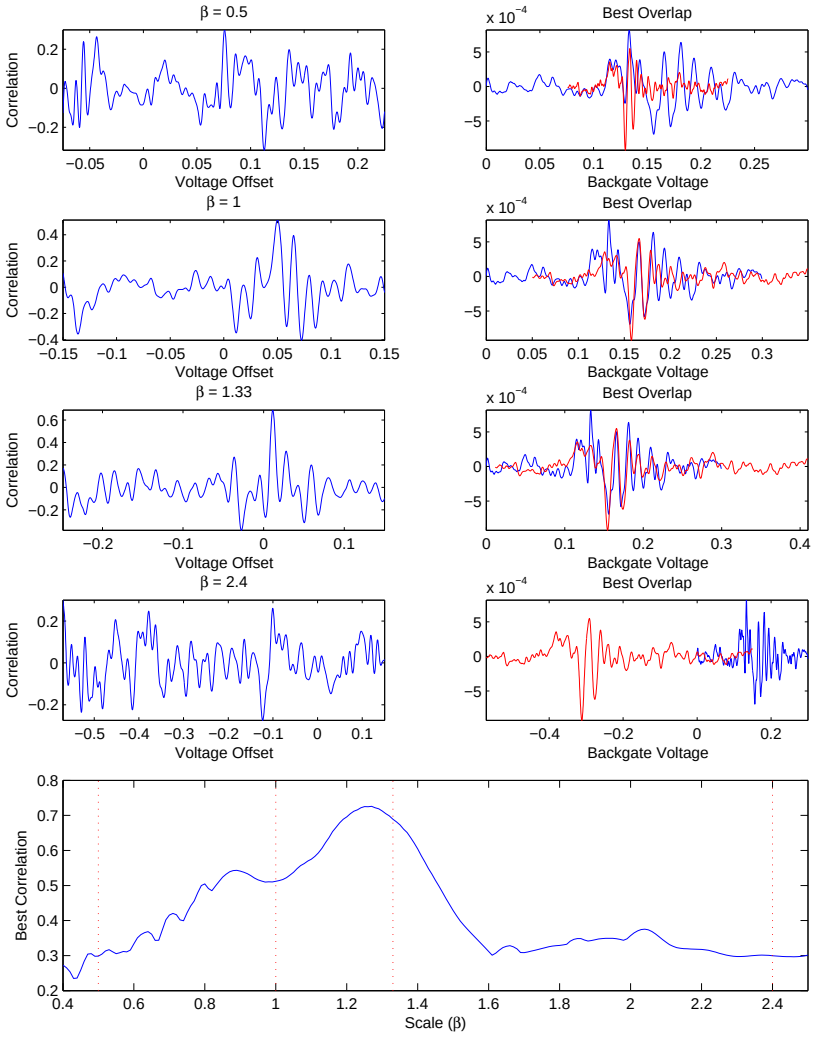

Figure 2.4.2: Overview of fitting procedure for data on 3rd row (from the bottom) on Figure 2.2.1. A scale of $4/3$ appears to qualitatively produce the best overlap, and the analysis agrees.

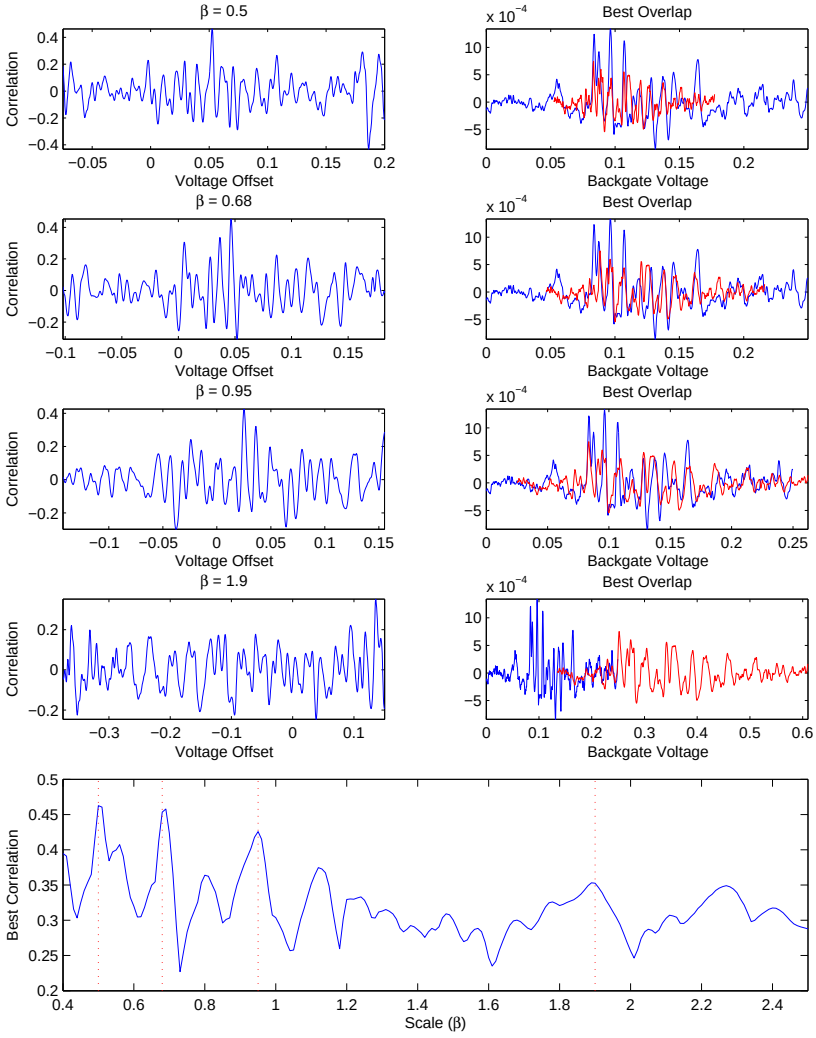

Figure 2.4.3: Overview of fitting procedure for data on 4th row (from the bottom) on Figure 2.2.1. No scale stands out, qualitatively or quantitatively.

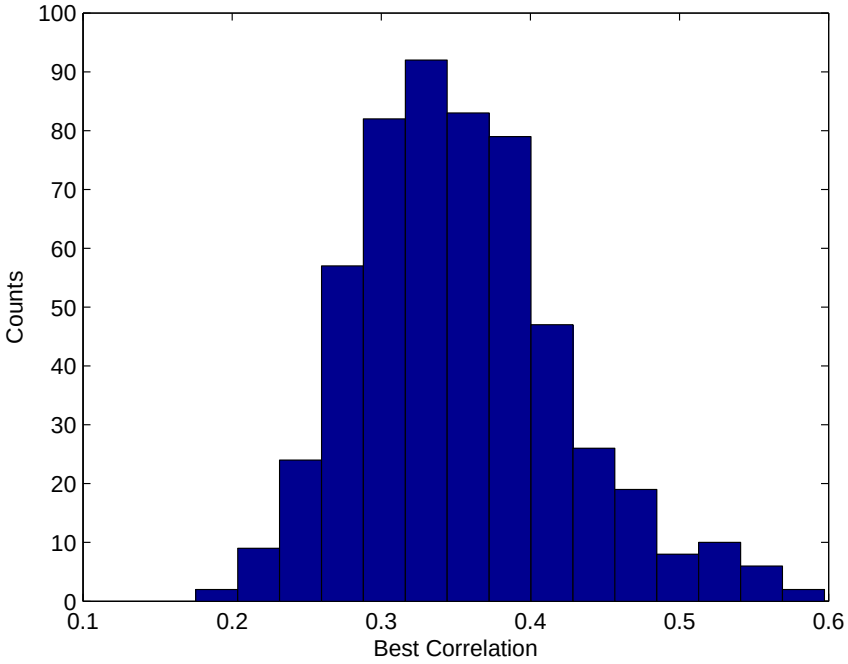

Figure 2.4.4: Histogram of best correlation values for uncorrelated data, scaled by 1.33. This distribution has $\mu = 0.36$ and $\sigma = 0.073$, giving a standard error of the mean (for a 20 sample average) of $0.073/\sqrt{20} = 0.016$. This is what is displayed in red on figure 2.2.1b of the main paper.

Coming back to where you started is not the same as never leaving.

Terry Pratchett

3

Local Probes of Non-Abelian Statistics at $\nu = 5/2$

The observation of localized quasiparticles that may possess exotic quantum properties begs the question of what we can do with them. Clearly the $e/4$ objects described in Chapter 2 interact via a Coulomb interaction to provide the observed charging spectra. If this was the only observable interaction between particles, there would be no need to describe them with anything beyond classical electromagnetism. This chapter will describe possible future experiments to study properties beyond Coulomb physics. As this topic of is one of the main motivations for continued studies of the $\nu = 5/2$ FQH state, there are many exciting proposals for how one may go about identifying "statistical" (non-Coulomb) interactions between quasiparticles ([12, 52]). Most proposals involve attempting to entangle $e/4$ quasiparticles on the edge with particles localized in the bulk to dephase an interferometer. Several experiments ([45, 49, 60, 63]) have begun to make progress towards this goal.

This chapter will focus on signatures that can be obtained directly from bulk

measurements, using our knowledge that $e/4$ objects are electrostatically confined to quantum dots by the bare disorder potential. For a given equilibrium distribution of $e/4$ objects in puddles throughout the bulk of a sample, the existence of non-Abelian statistics requires a degenerate ground state associated with a chargeless degree of freedom in these quasiparticles. If the temperature is low enough and measurements are fast enough, it may be possible to watch and manipulate the system as it moves through this manifold of ground states. This is precisely what is needed to use the system for topological quantum computation, and is the subject of Section 3.4. First we will focus on the other regime, more readily accessible to experiments, in which the system explores the entire ground state manifold in an incoherent way on a timescale faster than we measure. Even here, the appearance of additional quantum states as particles are added has thermodynamic signatures, first pointed out in [18]. We'll begin by summarizing the predictions of that work before discussing possible experiments to identify ground state degeneracies.

3.1 Measuring Entropy via Chemical Potential

Increasing the temperature of a system biases it to explore classical macrostates with more internal configurations (entropy), even if those states have a slightly larger bare energy. This can be taken into account by requiring the system to minimize its free energy $F = E - TS$ instead of the bare energy E. If adding a particle to a system creates a macrostate with more entropy, the free energy for that macrostate will be lowered as the temperature is increased. This is summarized in a Maxwell relation:

$$\left.\frac{\partial \mu}{\partial T}\right|_n = -\left.\frac{\partial s}{\partial n}\right|_T \tag{3.1}$$

Here s is the entropy per area and n is the areal particle density. The most likely case of having Majorana modes localized to the cores of the $e/4$ particles would create a ground state degeneracy of $2^{N_{qp}/2-1}$. This corresponds to one two-state system per pair of Majorana modes, with the overall fermion parity fixed.

The corresponding entropy per unit area for the Majorana modes is then $s_M = k_B n_{qp} \frac{1}{2} \ln 2$. The density of charge $e/4$ quasiparticles is given by $n_{qp} = 4\left|n - n_{5/2}\right|$, where $n_{5/2}$ is the density required for a filling of exactly $5/2$. Note that the density of quasiparticles increases as the density is varied in either direction

starting from $n_{5/2}$, corresponding to the addition of holes or particles. We can rewrite the Maxwell relation for quasiparticles as follows:

$$\left.\frac{\partial \mu}{\partial T}\right|_n = -\frac{ds_M}{dn_{qp}} \left.\frac{\partial n_{qp}}{\partial n}\right|_T = \mp k_B 2 \ln 2 \tag{3.2}$$

3.2 Directly Measuring $\mu(T)$

The simplest approach to measuring entropy involves measuring μ with a single electron transistor (SET) while modulating the temperature. By fabricating an SET with a large island ($1\mu m \times 1\mu m$), above a 2DES 200 nm below the surface, we have typical voltage (chemical potential) sensitivities of 30 nV/$\sqrt{\text{Hz}}$ or temperature sensitivities (using 3.2) of 0.25 mK/$\sqrt{\text{Hz}}$.

To perform the measurement, one would vary the temperature while monitoring the electrostatic potential φ of the 2DES with an SET. By continually adjusting the electrochemical potential of the 2DES (V) to keep φ (and therefore n) fixed, we will have a measurement of $\mu(T)$ at fixed n, as desired. The small temperature modulations required provide hope that this approach will work.

3.3 Measuring $\mu(T)$ locally

An alternative approach is to fix the number of quasiparticles on a given puddle (or group of puddles) located near a charge sensor (SET). As the temperature is increased, the required electrostatic incentive for a quasiparticle to create a high-entropy state is decreased. For particles (negatively charged), this would correspond to addition at lower gate voltages. For holes, this would correspond to addition at higher gate voltages. The expected spectrum would therefore be a crisscross of charging lines corresponding to particles and holes, all with a slope given by Equation 3.2 (see Figure 3.3.1A).

This picture becomes slightly more complicated if particles are added to the same puddle. The Majorana modes associated with two $e/4$ quasiparticles can hybridize as they're brought close together, creating a gap and eliminating their contribution to the ground state entropy. In this situation, only configurations with an odd number of quasiparticles will have an increased entropy. As the temperature is increased, we can

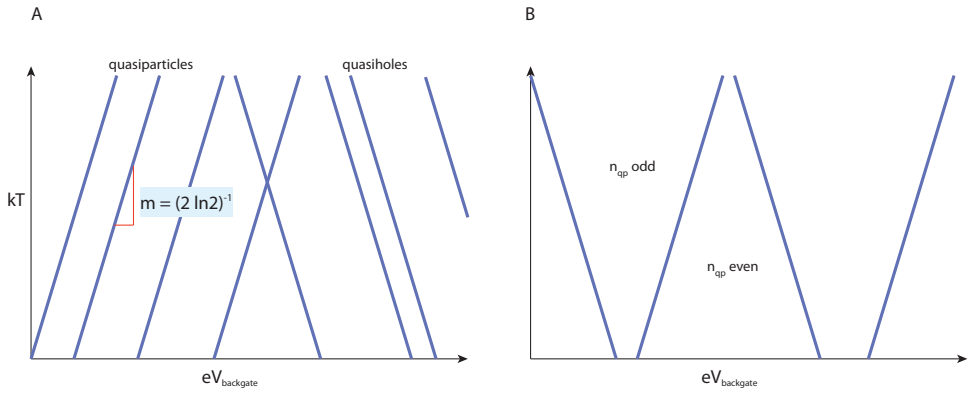

Figure 3.3.1: A, A charging spectrum where each line corresponds to an isolated quasiparticle being added to a separate disorder site. At higher temperatures, non-Abelian particles tend to add sooner due to entropic gains. **B,** In an isolated puddle, we would only expect an entropic gain if there is an odd number of quasiparticles on the island. The paired Majoranas would split in energy and no longer contribute to a ground state degeneracy. Thus, regions with odd numbers of quasiparticles would be favored at higher temperatures.

expect those regions with odd quasiparticle occupation to grow as regions with even occupation shrink[7]. Such an entropic effect on the size of charge stability regions has been observed in the shell structure of vertical quantum dots [17]. It has been predicted to show up in quantum dot transport [6], but has not yet been demonstrated.

Samples with built-in backgates (as used to obtain the data in Chapter 2) have been consistently poor in transport quality (see Figure 3.3.2). By using a bromine/methanol etchant to thin wafers to a thickness of 80 μm and subsequently evaporating a metal gate on the backside, we have been able to get good density control of high quality materials that hold promise for the entropy measurements described above.

We've made some preliminary attempts to see the predicted movement of Coulomb blockade peak locations as a function of temperature in a this high-quality sample (see Figure 3.3.3). The first attempt involved heating the fridge while watching a few charging events (3.3.3b). While the charging events were stable prior to applying heat, they moved in a very dramatic (and untraceable) fashion upon heating by even a small amount (the data shows heating from an electron temperature of roughly 20 mK to 27 mK). A better approach is to heat the electrons directly. To attempt this, we added a microwave source to the voltage signal supplied to the 2D. By controlling the

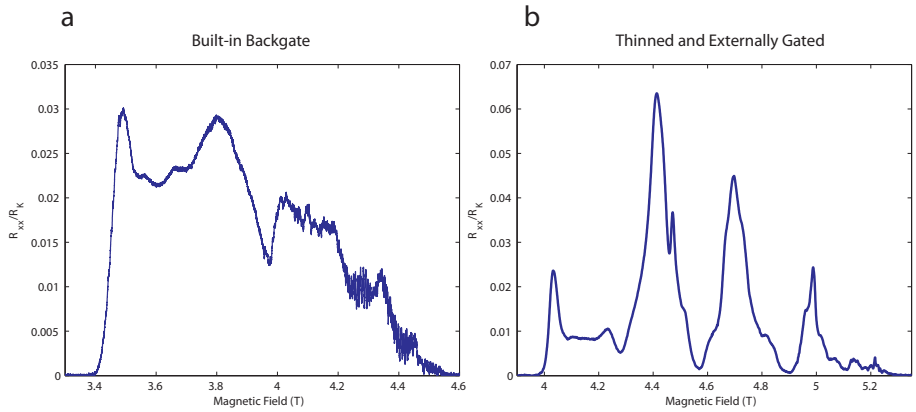

Figure 3.3.2: a, R_{xx} for LP 9-21-07.1, the best backgated sample grown at Bell Labs or Princeton that we've studied. The gate is a heavily doped, thick (3DES) region roughly 2 μm beneath the 2DES. The region between $\nu = 5/2$ and $\nu = 2$ in all backgated samples routinely show many mesoscopic fluctuations along with a diminished value of R_{xx} compared to the region between $\nu = 5/2$ and $\nu = 3$, which is typically closer to what is seen in high quality non-backgated materials. **b,** LP 7-27-10.1, a standard symmetrically doped well. This sample was thinned down to roughly 80 μm and a metallic gate was added to the back to control density. The quality still has the same asymmetry described above, but prominent fractions are well-developed and hints of reentrant behavior can be seen. Both samples have roughly the same range of density tunability.

microwave power on this line, we can hope to effectively heat the 2DES without affecting the lattice. The downside of this approach is that we cannot exactly determine the temperature. Figure 3.3.3a shows results from a first attempt at this strategy. Here peaks are traceable, but they appear to broaden and lose contrast before any motion can be detected. No strong conclusions should be drawn from these preliminary measurements.

3.4 Topological Quantum Computing With Disorder Localized Quasiparticles

If the quasiparticles at $\nu = 5/2$ state do indeed have some non-Abelian statistical interactions, and if those quasiparticles explore the resulting ground state subspace slowly (compared to measurement and manipulation times), it should be possible to use these statistical interactions to build a quantum computer. Just for fun, we will

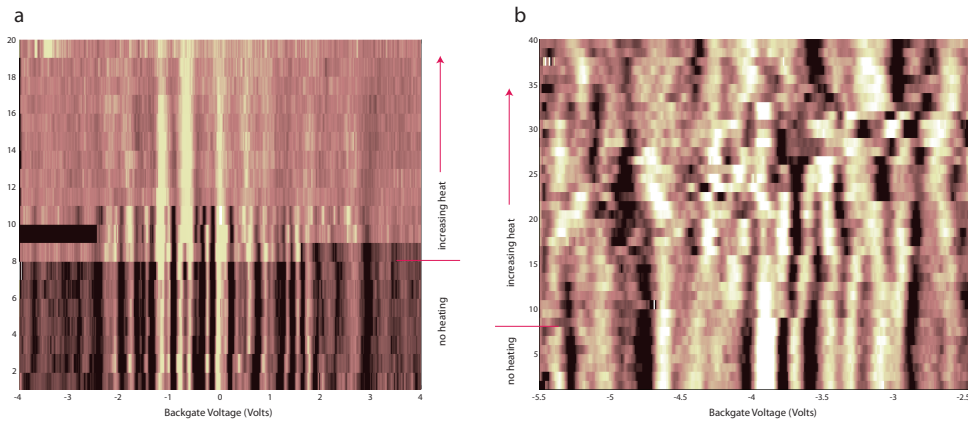

Figure 3.3.3: Two attempts to measure a charging spectrum evolve with increasing temperature. Both measurements were done on the material LP 7-27-10.1 containing a high-mobility ($\mu = 27 \times 10^6$ cm^2/Vs, $n = 2.7 \times 10^{11}$ cm^{-2}) 2DES buried 420 nm beneath the surface. The wafer was thinned to 50 μm and Ti/Au gate was evaporated to control the density from the backside. The starting electron temperature in both cases (bottom line) was roughly 20 mK. **a,** Repeated charging spectra obtained by heating the electron system with microwaves sent to the 2DES. This technique is good for quickly controlling the electron temperature without affecting the lattice temperature. However, it is hard to associate a quantitative temperature to any given line. Charging events broaden and lose contrast, but do not appear to move (versus gate voltage) more than they did prior to heating. **b,** Repeated charging spectra while applying heat directly to the still of our dilution refrigerator (the mixing chamber heater was broken at the time). The total change in electron temperature here (from bottom to top) is roughly 10 mK. Charging events move around dramatically, but not in a trackable way.

briefly sketch out how one may go about building a topological quantum computer by pushing around disorder-localized quasiparticles and sensing charge.

3.4.1 What is a Topological Quantum Computer?

A quantum system that doesn't interact with its environment evolves according to a simple rule:

$$|\psi(t)\rangle = U(t)\,|\psi(0)\rangle \tag{3.3}$$

where $U(t)$ is a unitary operator on the Hilbert space for the system. To make a quantum computer, we need to do two things. First, we need to manipulate the system by controlling $U(t)$. Second, we need to entangle the system with a probe to extract information from the system. These so-called decohering operations are necessary to

initialize the system and read out the results of a computation [48].

Suppose we have a set of analog inputs to the system, described by a vector $\mathbf{x}(t)$, that affect the evolution of the system without destroying coherence. For simplicity we will assume that $\mathbf{x}$ has a finite temporal extent and that $\mathbf{x}(t_{\text{end}}) = \mathbf{x}(0) \equiv 0$. The evolution of the system, as controlled by the experimenter, is then given by $|\psi(t)\rangle = U(\mathbf{x}(t))\,|\psi(0)\rangle$.

A conventional quantum computer typically has $|\psi(t)\rangle$ depending sensitively on small changes to $\mathbf{x}$. For a certain class of Hamiltonians (such as charges moving in magnetic fields), the evolution can depend only the path a particle takes (similar to a Berry or geometrical phase). In this case, $U(\mathbf{x}(f(t))) = U(\mathbf{x}(t))$ where $f(t)$ provides a reparametrization of the original path. Being insensitive to time dilations of this sort necessarily means that all the states participating in computation must have the same energy, for a difference in energy between states induces a strict time-dependence in evolution.

This geometric quantum computer, with its energy-degenerate computational Hilbert space, is protected against a small class of input noise. However, changing the input slightly from $\mathbf{x}$ to $\mathbf{x} + \boldsymbol{\delta}\mathbf{x}$ will generally provide a close, but non-identical, unitary operation. The small errors afforded by this are a source of decoherence that have to be addressed by error-correction schemes.

A topological quantum computer can be described as a geometric quantum computer whose evolution is insensitive to precisely these types of fluctuations in inputs [47]. As a result, large sets of inputs that produce identical evolution can be grouped into equivalence classes $\mathbf{X}^{(i)}$ as depicted in Fig. 3.4.1.

The protection afforded by a topological quantum computer naturally makes it challenging to initialize and readout information. Generally, inputs near the boundary regions (red in Fig. 3.4.1a) will be unprotected and therefore good candidates for entangling the system with a probe for readout.

3.4.2 A Quantum Computer at $\nu = 5/2$

For Ising anyons (which would be relevant for the Moore-Read state at $\nu = 5/2$), these protected inputs correspond to braiding quasiparticles around each other[46]. The resulting protected unitary operations would correspond to single qubit rotations by $\pi/2$ around one of the x, y, or z axes of the Bloch sphere, along with a controlled-NOT

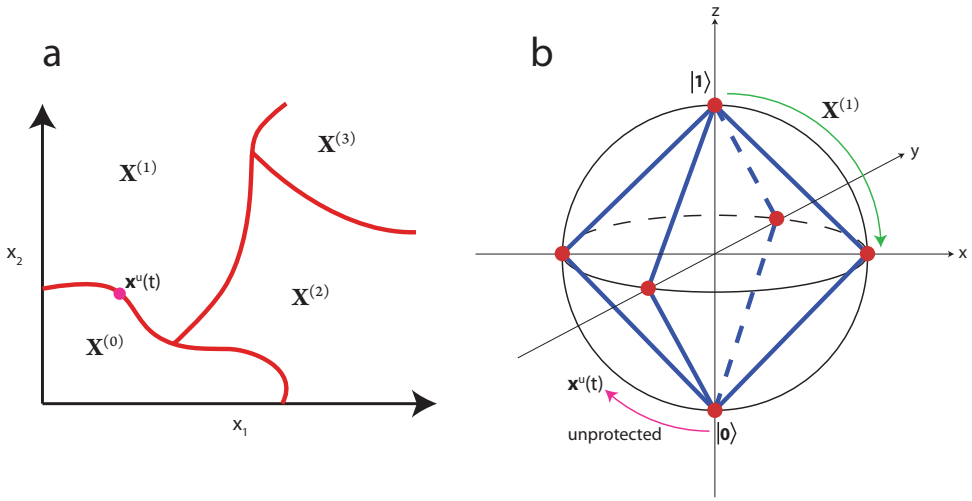

Figure 3.4.1: Control Space for a Topological Qubit. **a**, Large classes of similar inputs result in the exactly same unitary evolution of the system, denoted here by $\mathbf{X}^{(i)}$. **b**, For Ising anyons, the allowed single qubit operations correspond to rigid rotations of the Bloch sphere by $\pi/2$ around one of the x, y, or z axes. The state $|1\rangle$ can be taken to any of the red points on the Bloch octahedron drawn in blue. A protected operation from $\mathbf{X}^{(1)}$ is shown in green. Other non-Abelian systems (such as Fibonacci anyons) allow full access to the Bloch sphere with repeated operations. Input signals arbitrarily close to the boundary between equivalence classes (magenta dot, arrow) can be used to implement unprotected operations.

gate between any pair of qubits. These operations, however, are not sufficient to make a universal quantum computer. An additional unprotected unitary gate is needed[13]. This may be provided by bringing particles close together to break the ground state degeneracy and using the resulting time evolution to implement an unprotected unitary operation [5, 14]. Such operations would fall on the boundary between input classes in Figure 3.4.1a.

This operation of bringing particles close together can be used for initialization and readout as well. Each $e/4$ particle would have to pay a certain charging energy to enter a puddle occupied by another particle. There will be an additional energy cost which depends on the collective state of the two Majorana cores associated with the quasiparticles [5, 14]. If gates are tuned such that the particle will only enter if it is in the lower energy collective state, we can then read out the charge of the puddle using an SET to determine which collective state the particles were in. This is analogous to the approach of using spin-blockade to convert spin information to charge information

in spin qubits [33].

With these ingredients, we can imagine a stochastic approach to building a quantum computer using disorder-localized quasiparticles at any non-Abelian quantum Hall state. First, we would pattern a grid of gates on top of the sample, with a pitch matching the average spacing of disorder puddles (1 micron). Charge-sensing SETs for initialization and readout could be placed periodically at some larger interval. To determine what the gates do, they would have to be energized in some arbitrary way (ideally with some spatial continuity) followed by readout with an SET. With luck, certain inputs will generate a significant change in the distribution of readout values at the SET, indicating a change in the final state of the system.

To establish that this was a topologically protected operation, one could vary the input by small amounts while monitoring readout distributions. If output distributions are stable for large regions of inputs, we would have good evidence for topological protection. To establish that a given input changes the system in a unitary way, we would have to vary the number of times the input was given to the system. If the output distribution varied periodically with the number of times the input was applied, we would know that the input was unitary.

A cartoon of this type of computer is presented in Figure 3.4.2. Though such a device is a long way off (perhaps infinitely far off), the prospect of studying statistical interactions via local probes is certainly very exciting.

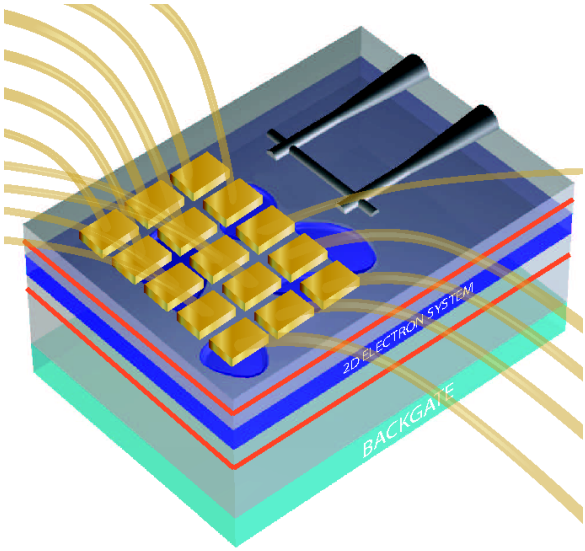

Figure 3.4.2: Sketch of a disorder based topological quantum computer. Localized quasiparticles of a non-Abelian quantum Hall state are in puddles of disorder. A grid of gates can be used to push them around in some arbitrary manner. Readout can be be accomplished via topological blockade using a charge sensor near one of the puddles. Using readout and tomography to calibrate the arbitrary inputs, the space of equivalent (protected) input classes can be determined.

Remember, a dead fish can float downstream, but it takes a live one to swim upstream.

W.C. Fields

4

Local Thermometry of Neutral Modes on the Quantum Hall Edge

When a two-dimensional electron system (2DES) is subject to a strong perpendicular magnetic field and tuned such that the ratio of electrons to magnetic flux quanta in the system (ν) is near certain integer or fractional values, the bulk of the system develops a gap due to either quantization of kinetic energy (the integer quantum Hall, or IQH, effect) or strong correlations arising from non-perturbative Coulomb interactions (the fractional quantum Hall, or FQH, effect) [27]. While the bulk (2D) is gapped and incompressible, the edge (1D) of the system contains compressible regions with gapless excitations that carry charge chirally around the system, in a direction determined by the external magnetic field. Compressible edge states have gained more attention recently due to their ability to serve as a bus for quasiparticles that exist in exotic FQH phases[12, 52]. These edges, however, can have considerable internal structure that is not apparent from bulk transport measurements.

The spatial structure of edges is dictated by the interplay between the external confining potential which defines the edge, an additional harmonic confinement from

the magnetic field, and Coulomb interactions. It was predicted [15] and verified [30, 61, 64] that for a smooth, topgate-defined confining potential, it is energetically favorable for the electron density to redistribute slightly to create alternating compressible and incompressible strips. This has the effect of spatially separating edges corresponding to different filling factors. Such an effect is not present in sharper edges [29].

Perhaps more surprising than this spatial structure is the possibility of modes that carry energy (or heat) upstream, even as the magnetic field carries the injected charge downstream. The edge of the $\nu = 2/3$ FQH state was originally predicted to consist of a $\nu = 1$ edge of electrons going downstream with a $\nu = 1/3$ edge of holes going upstream [42, 59]. However, this edge structure would suggest a two-terminal conductance of $G_{2T} = \frac{4}{3}\frac{e^2}{h}$. Scattering between the edges would lead to non-universal values in the range of $\frac{2}{3}\frac{e^2}{h} \leq G_{2T} \leq \frac{4}{3}\frac{e^2}{h}$. Experimentally, however, no such two terminal conductance has been measured. Direct approaches to look for upstream charge transport in the time domain have similarly turned up no evidence [4]. This motivated a picture in which disorder induces scattering and equilibration between the edges, forcing the charge to travel exclusively downstream. Heat, however, would be allowed to travel diffusively upstream and downstream, leading to a nonzero thermal Hall conductivity and partial upstream heat transport at $\nu = 2/3$ [34, 35].

Evidence for upstream heat transport in a $\nu = 2/3$ edge was recently obtained by performing modified shot noise measurements [9]. Our approach studies the same state by directly placing thermometers upstream and downstream of a current-source heater to observe charge and heat transport along the edge.

4.1 Charge Transport

As our heater, we use a lithographically fabricated quantum point contact (QPC), tuned to the tunneling regime (Fig. 4.1.1C). Tunneling of electrons through this QPC at elevated energy locally excites the outermost compressible component of a gate-defined edge. We then place quantum dots 20 μm upstream and downstream of the QPC to measure charge and heat transport (Fig. 4.1.1A). The edge itself is defined by a separate pair of gates (green in Fig. 4.1.1A), and the perpendicular magnetic field defines a clockwise charge-propagation direction (with respect to Fig. 4.1.1). All measurements were carried out in a dilution refrigerator with a minimum electron

temperature of 20 mK, measured with Coulomb blockade thermometry.

To first characterize the structure of the edge that we are tunneling charge into, we energize a subset of gates upstream (blue) and downstream (red) of the central QPC to create additional point contacts that serve as imperfect voltage probes ($R \sim 100\ \mathrm{k}\Omega$). This ensures that we only measure the chemical potential of the outermost edge component [56]. Current is injected through the central QPC (10 pA sourced through O3 and drained at O6). The upstream chemical potential, $V_1 - V_7$, was observed to be immeasurably small in all measurements, indicating that no charge is transported upstream on a 20 μm scale. The downstream chemical potential, $V_5 - V_7$, can be used to determine the resistance of the edge connecting the source to the probe (the "local Hall" resistance R_L). This resistance is plotted in blue in Fig. 4.1.2. Additional measurement details can be found in Section4.3.

For magnetic fields (B) between 2 T and 8 T, the measured value $R_L = 1\frac{h}{e^2}$ indicates that the charge is carried between the injector and detector by electronic modes that behave similarly to an IQH $\nu = 1$ edge. Inner edges can (and must, at fields below 6 T) be present, as can be seen by comparing R_{xy} with R_L. These inner edges, however, do not carry any of the injected charge. Above 8 T, we find that R_L is quantized to $R_L = \frac{3}{2}\frac{h}{e^2}$ even though the bulk is at $\nu = 1$[38]. This suggests that the edge has additional structure consisting of alternating compressible and incompressible regions which are spatially separated, as indicated in Fig. 4.1.2 (IV). In this situation, we only access the outermost edge of the incompressible $\nu = 2/3$ strip located outside the $\nu = 1$ bulk. The robust quantization that we observe indicates that no charge leaks out of this outermost $\nu = 2/3$ edge over the 20 μm separating the injector from the detector.

The edge-deflecting gates (green in Fig. 4.1.1A) can be deenergized to deflect the edges into floating ohmic contacts located 250 μm away (O2 and O4), where they will chemically equilibrate and thermally cool (though some equilibration and cooling may occur before the edges reach the ohmic contacts). If we repeat this charge transport measurement with the deflector gates deenergized, we continue to monitor no upstream charge transport. However, the downstream resistance is observed to match exactly the bulk value of R_{xy}, plotted in black in Fig. 4.1.2. This indicates that our deflection process does, indeed, force all edges to fully chemically equilibrate in ohmic contacts O2 and O4, providing an important control for the heat transport

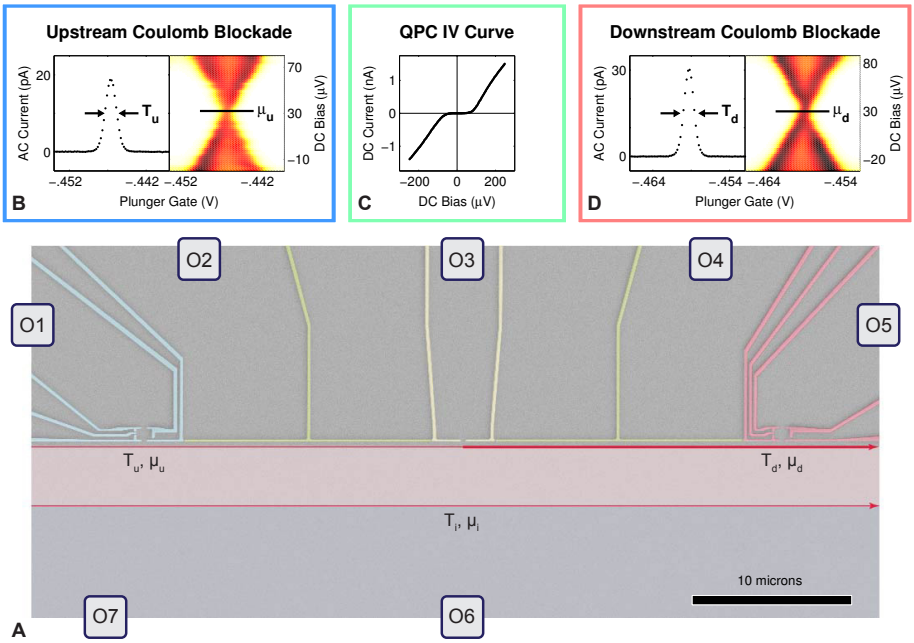

Figure 4.1.1: A) Scanning electron micrograph showing the gate geometry of the device. O1-7 denote ohmic contacts. Injection of current through the central quantum point contact (QPC) populates the outermost quantum Hall edge channel, creating a non-equilibrium distribution. Deflector gates adjacent to the injection site define the edge or can be de-energized to deflect edge channels to floating ohmic contacts (O2 and O4). A quantum dot located 20 microns downstream of the injection site is used to measure the temperature T_d and chemical potential μ_d of the outer edge channel. Similarly, an upstream dot measures T_u and μ_u. B, D) Coulomb blockade (CB) peaks and diamonds for the quantum dots. The temperature is determined from the CB peak width. The chemical potential is determined by zeroing the voltage bias across the quantum dot. C) The IV characteristic of the QPC. For charge transport, the QPC was operated just beyond blockade. Heat transport measurements were taken at all points of the IV curve.

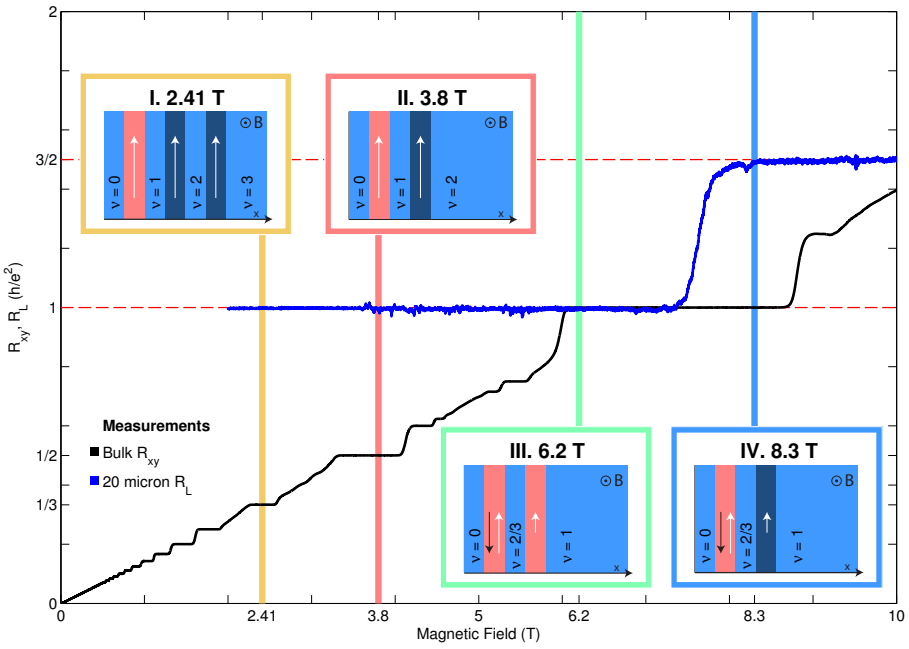

Figure 4.1.2: Magnetic field dependence of the Hall resistance R_{xy} (black), and the local Hall resistance R_L (blue). The local Hall resistance is measured using the central QPC as a current source ($\sim$ 10 pA) and a downstream QPC as a voltage probe. Plateaus in R_L reveal the structure of the edge, and also indicate which edge channels participate in charge transport. The insets depict the qualitative structure of the sample edge at various magnetic fields, with incompressible regions shown in light blue and labeled by filling factor. In the intervening compressible channels, white arrows point in the direction of charge flow, while the arrow length specifies a charge conductance of $G = 1$, $2/3$, or $1/3$ in units of e^2/h. Black arrows indicate neutral modes that carry energy upstream. The channels highlighted in red contribute to charge transport at the voltage probe. I,II) When the bulk filling factor is $\nu = 2$ or $\nu = 3$, the edge is composed of integer channels with the outermost channel having conductance $G = 1$. At the voltage probe, the excess current is carried solely by the outermost channel. III,IV) Outside the bulk $\nu = 1$ state the edge is reconstructed, resulting in an outermost $G = 2/3$ charge channel. The remaining $1/3$ conductance can be found on a spatially separated inner edge located in the compressible region between the $\nu = 2/3$ and $\nu = 1$ incompressible regions. At 8.3 T, the excess current is carried to the voltage probe only by the outermost channel. At 6.2 T, the edge channels come to the same potential before reaching the voltage probe, resulting in $R_L = 1$.

measurements discussed below.

4.2 Heat Transport

To characterize heat transport, we energize all of the gates upstream and downstream of the central QPC to form quantum dots, which serve as thermometers to measure the temperature of the edge. This is similar to another recent spectroscopic approach [1, 2, 54]. The width of the Coulomb blockade peak as a function of gate voltage can be translated into the temperature of the leads (Fig. 4.1.1B, details in Section 4.3).

With the thermometers active, we inject current through the QPC set to an average transmission of 15%[1] to create a non-equilibrium population in the outermost edge (Fig. 4.1.1C). The low transmission ensures that we inject solely electrons into the edge (no FQH edges are fully transmitted). These energetic electrons, however, are not necessarily the elementary excitations of the edge and will therefore excite the natural edge modes as they decompose. By increasing the bias across the QPC, we vary the current (and therefore the power) being delivered to the edge. We monitor both the chemical potential and temperature of the edge at the upstream and downstream dots (Fig. 4.1.1B and 4.1.1D).

Measurements are first performed with the deflector gates energized, to measure heat transport associated with the edge (red and blue curves in rows 1 and 2 of Fig. 4.2.1). We then repeat the procedure with the deflector gates off, to measure any background heating not associated with the edge (cyan and magenta curves in rows 1 and 2 of Fig. 4.2.1). The difference between these two temperatures gives us a measure of the excess heat carried by the edge (bottom row in Fig. 4.2.1, red is downstream and blue is upstream temperature).

At the two lowest fields that were measured (2.41 T and 3.8 T), our charge transport measurements indicate that we are injecting charge into a $\nu = 1$ edge sitting outside an incompressible bulk at filling $\nu = 3$ or $\nu = 2$ respectively. This is depicted schematically in Fig. 4.1.2 (I,II) and in Fig. 4.2.2 (II). By monitoring the chemical potential as we vary the injected power, we find that charge is carried exclusively by the outermost $\nu = 1$ edge over the entire range of measurement (Section 4.3).

[1] This can be obtained by subtracting the series Hall resistance from the resistance depicted in Fig. 4.1.1C and converting the remainder to a transmission

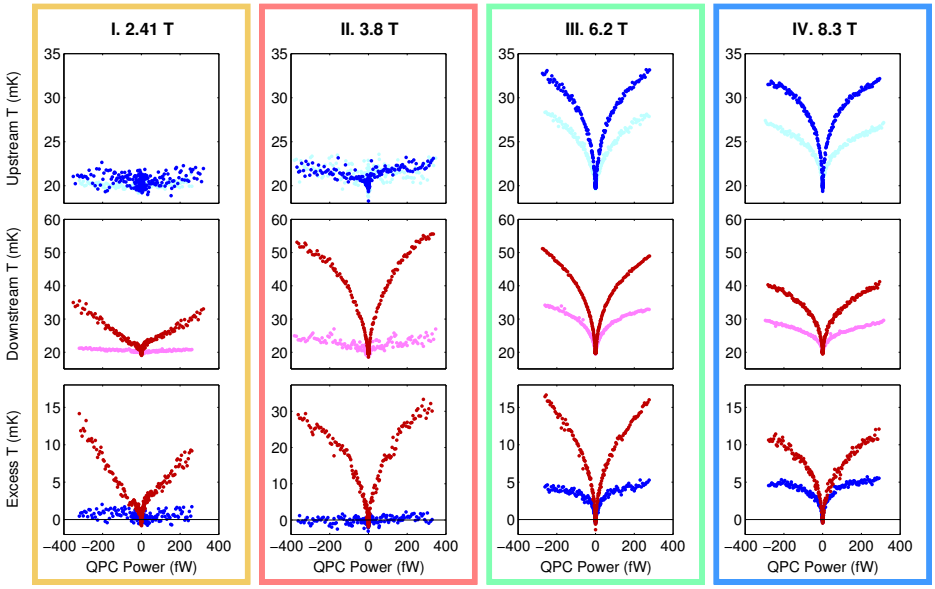

Figure 4.2.1: Dependence of the local edge temperature on the power dissipated in the QPC ($|I| \cdot \Delta V_{QPC}$), at different magnetic fields. Negative (positive) QPC powers correspond to the injection of holes (electrons). For each magnetic field, the upstream and downstream temperatures were measured with (blue, red) and without (cyan, magenta) the deflector gates energized. With the deflectors at zero voltage the edge channels are directed to floating ohmic contacts where equilibration occurs. The difference between temperatures with and without the deflectors energized, for the same dot, yields the local change in temperature due to the heat carried by the edge. This excess temperature for the downstream (red) and upstream (blue) dots is plotted across the bottom row, for each magnetic field. For I and II, corresponding to an integer outermost edge, heat is carried chirally downstream with no upstream heat transport. For IV, where we measure a 2/3 outermost edge, the heat is carried downstream and upstream. For III, heat is also carried in both directions, while $R_L = 1$. We attribute this behavior to reconstruction outside the bulk $\nu = 1$ edge, which allows upstream heat transport without 2/3 charge transport.

At 2.41 T, when the bulk is at $\nu = 3$, there is no measurable background heating either upstream or downstream. When the deflectors are turned on, we find heating downstream but none upstream. When the bulk is at $\nu = 2$, we find about 2-3 mK of background heating that is perfectly cancelled in the upstream direction. Thus, in both cases, we find that heat carried by edge modes is transported exclusively downstream. While this strict downstream heat transport in the IQH regime is expected and matches previous measurements [9, 28], surprisingly, the magnitude of the temperature observed does not agree with what one would expect from quantized thermal transport (assuming an equilibrated edge):

$$K_H \equiv \frac{\partial J_E}{\partial T} = n\frac{\pi^2}{3}\frac{k_B^2}{h}T \implies T = \frac{\sqrt{6hJ_E/n}}{\pi k_B},$$

where J_E is the power carried by the edge and n is the number of IQH edges participating in transport [34]. At $\nu = 2$, for an injected power of 350 fW, we expect an edge temperature between 430 mK and 608 mK, depending on how well the two edges thermally equilibrate ($n = 2$ or $n = 1$). Our measured temperature of 30 mK indicates that a substantial quantity of heat is transferred out of the edge[2]. We can model the behavior of heat transport for out-of-equilibrium Fermi systems (Section 4.4), which indicates a similar temperature deficiency. Both models, however, give the correct shape for the temperature versus power curves presented in Fig. 4.2.1.

At the highest measured field, 8.3 T, charge transport (Fig. 4.1.2) indicates that we have an incompressible $\nu = 2/3$ strip outside a $\nu = 1$ bulk, depicted schematically in Fig. 4.1.2 (IV). Here we see substantially more background heating, both upstream and downstream. This bulk heating at $\nu = 1$ is unexpected and hasn't previously been observed, though a similar result at $\nu = 4/3$ has recently been reported [3]. Additional details can be found in Section 4.5. After subtracting contributions from the bulk (deflectors energized) we still find an upstream temperature rise of 5 mK at 300 fW, compared to a downstream rise of 11 mK. Such upstream heating is consistent with the predicted upstream thermal conductivity of the outer $\nu = 2/3$ edge[34], though the assymmetry between upstream and downstream temperatures suggests that the inner $\nu = 1 \to 2/3$ edge (which carries heat preferentially downstream) is partially participating in heat transport.

At the second highest measured field, 6.2 T, one would expect, based on charge transport, behavior similar to what we find when the bulk is at $\nu = 2$ or $\nu = 3$, with all

heat being carried downstream by the integer $\nu = 1$ edge. Instead, we find a behavior similar to what was observed at 8.3 T, with heating both upstream and downstream and a slight asymmetry between the two. This surprising result can be understood if we allow for the presence additional structure in the $\nu = 1$ edge that does not affect charge transport. Perhaps the simplest such structure would be the presence of an incompressible strip of $\nu = 2/3$, much like what we see at 8.3 T, but with charge equilibrating between the two separated edges of this strip (Fig. 4.1.2 (III)). With these edges equilibrated, we measure a local Hall resistance of $R_L = \frac{h}{e^2}$. However, the diffusive heat transport provided by the outer $\nu = 2/3$ edge could still carry heat to the upstream thermometer (edge IV in Fig. 4.2.2). Additional evidence for such an edge structure is presented in Section 4.6. Importantly, this mechanism of upstream heating by an apparent $\nu = 1$ edge would not be universal and would depend sensitively on the spatial reconstruction of that edge. A sharper mesa-defined edge with a larger density gradient [9, 28] or a lower-mobility 2DES may not allow an incompressible strip of $\nu = 2/3$ to form outside the $\nu = 1$ bulk. In Section 4.6, we present a device with a mesa-defined edge that shows no upstream heat transport at 6.2 T (edge III in Fig. 4.2.2).

By studying the charge and heat transport properties of the outermost component of a gate-defined quantum Hall edge, these measurements paint a picture in which such edges contain considerable structure. Charge transport along the edge shows that correlated FQH modes can exist outside an IQH bulk. Even when these charge signatures are not present (Fig. 4.1.2 (III) and edge IV in Fig. 4.2.2), heat transport suggests that density reconstructions can still create additional edge components that carry heat upstream. In addition to this, by separating bulk and edge contributions, we have been able to observe bulk heat transport at $\nu = 1$ which is absent at $\nu = 2$ and $\nu = 3$, the origin of which remains an open question.

More generally, our system provides a framework to extract quantitative information about charge and heat transport at the boundary of any two-dimensional topological insulator. Such a system can be essential to discriminate between topological states of matter that have identical charge transport behavior. For example, with the $\nu = 5/2$ FQH state, the presence or absence of these neutral modes would allow us to discriminate between distinct ground states that are particle-hole conjugates of each other [24, 40, 41].

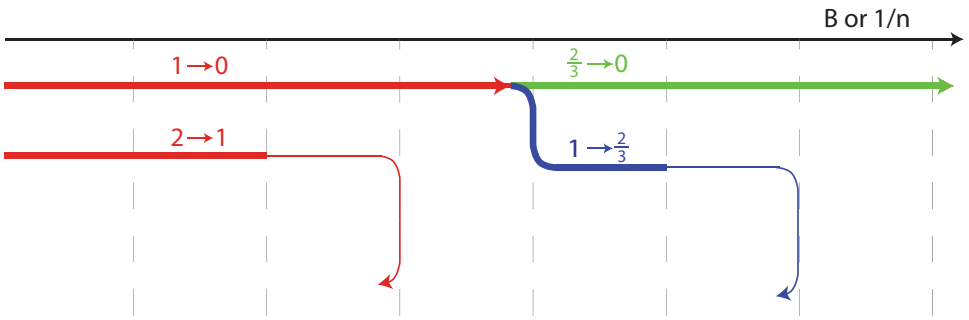

	(I)	(II)	(III)	(IV)	(V)	(VI)
R_{xy}^{-1}	2	2	1	1	1	2/3
R_L^{-1}	2	1	1	1	2/3	2/3
upstream heat	no	no	no	yes	yes	yes

Figure 4.2.2: One possible evolution of edge structure as a function of magnetic field. Three types of edges are present in this experiment, denoted by different colors, with the topmost edge being the outer edge. Only edge structures II, IV, and V are present in the device in Fig. 4.1.1. Edge III is presented in Section 4.6. All resistances are given in units of $\frac{h}{e^2}$. A measurement of R_{xy} allows one to determine the total conductance of all edges. A measurement of R_L allows one to determine which edges chemically equilibrate when charge is injected into the outer edge (denoted by bold lines in the figure). Only the $\frac{2}{3} \rightarrow 0$ edge transports heat upstream, and can be identified by our thermometry measurements. Detecting upstream heat allows us to discriminate between edges III and IV (see Section 4.6).

Acknowledgments: We acknowledge financial support from Microsoft Corporation Project Q, the NSF GRFP, and the DOE SCGF Program.

Author Contributions: V.V. and S.H. conceived and designed the experiments, prepared samples, carried out the experiments and data analysis and wrote the paper. A.Y. conceived and designed the experiments, carried out data analysis and wrote the paper. L.N.P. and K.W.W. carried out the molecular beam epitaxy growth.

4.3 Chemical Potential Measurements and Thermometry

I. Chemical Potential Measurement

As the DC current I injected through the QPC increases, the downstream chemical potential of the outermost edge component must correspondingly rise. Unless a DC voltage bias V_{ZB} is applied to O5 to exactly compensate this altered chemical potential, a DC current will flow through the dot whenever the Coulomb blockade is lifted. Tuning the dot to this zero bias condition allows us to measure the chemical potential of the outermost edge component. In principle an upstream charge current may cause a similar rise in chemical potential at the upstream dot. For all measurements, the upstream chemical potential was indistinguishable from that of the ground contact (O7), suggesting that upstream charge transport does not occur on a 20 μm scale.

The dependence of V_{ZB} on the current I, at a particular value of magnetic field, measures the total conductance of the edge channels participating in charge transport at the quantum dot. For the deflector gates energized, this conductance matches $1/R_L$. When the deflector gates are at zero voltage, however, all edges carry charge and the total conductance matches the Hall conductance. These observations corroborate the assertion that the deflector gates are able to direct the flow of edge channels. When the deflector gates are energized, the data also show that charge remains in the outermost edge on a 20 μm scale even during thermometry measurements. An example of edge resistances determined using the quantum dot zero bias condition is presented in Fig. 4.3.1.

II. Coulomb Blockade Thermometry

At each value of the magnetic field, quantum dots were tuned to the Coulomb blockade (CB) regime. The typical charging energy was 50 μeV, while the typical spacing between CB peaks corresponded to 20 mV on the plunger gate. We calibrated each dot individually for thermometry measurements by extracting the slopes m_1 and m_2 of CB diamonds adjacent to the conductance peak of interest, as shown in Fig. 4.3.2. The lever arm $\alpha = C_G/C$ was then determined by

$$\alpha = \frac{|m_1 m_2|}{|m_1| + |m_2|}, \tag{4.1}$$

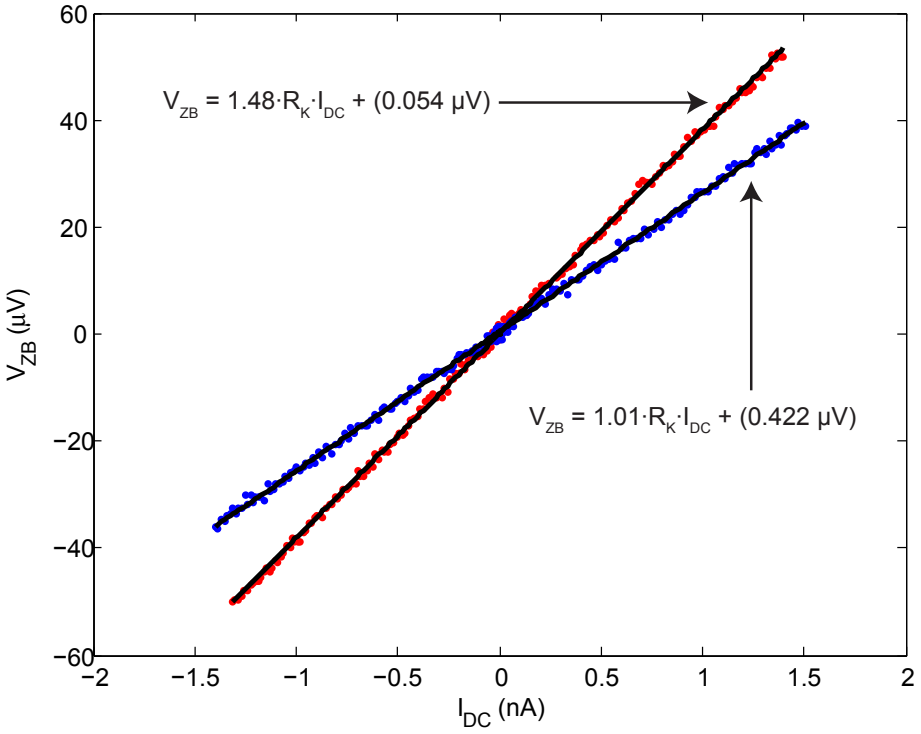

Figure 4.3.1: The voltage V_{ZB} applied to O5 in order to zero the bias across the downstream quantum dot, as a function of the current I_{DC} injected through the QPC. Data were acquired at a magnetic field of 8.3 T. For the deflector gates energized, V_{ZB} is shown in red, with a slope corresponding to current carried by a $\nu = 2/3$ outermost edge. When the deflector gates are set to zero, V_{ZB} is shown in blue, indicating conduction of current by edges with total conductance $G = 1$.

where C_G is the capacitance between the dot and the plunger gate, and C is the total capacitance. Knowing α allows the use of the conductance peak width as a sensitive thermometer. Our dots are in the metallic regime $\Delta E \ll k_B T \ll e^2/C$, where the temperature exceeds the dot level spacing ΔE. The temperature of the leads is then found through the formula for the lineshape of a conductance peak centered at gate voltage V_R :

$$G \propto \cosh^{-2}\left(\frac{e \cdot \alpha \cdot |V_R - V_G|}{2.5 k_B T}\right). \tag{4.2}$$

During the experiment, we applied a fixed 4 μV AC voltage bias and a variable DC voltage bias to each dot (contacts O1 and O5 in Fig. 4.1.1). The different AC frequencies used for each dot were typically 215 and 315 Hz. To determine the temperature T of the leads coupled to a single dot, we first tuned the DC voltage bias V_{DC} applied to the dot so that the chemical potentials of the two leads were equal, as described above. Then the plunger gate voltage V_G was swept through a conductance peak while the resulting AC current was monitored using lockin techniques. The typical AC dot resistance was $>$ 100 kΩ, resulting in AC currents of $\sim$ 10 pA. For each DC current I injected through the QPC, the temperature of the leads was extracted using equation 4.2. Representative scans over conductance peaks in the downstream dot, for two different injected currents, are plotted in Fig. 4.3.3.

A data set consisted of one sweep of the DC voltage bias V_{bias} applied to the QPC (contact O3), between -250 μV and 250 μV. At each value of V_{bias} we recorded the injected current I, as well as the temperature T and chemical potential μ for both dots. The QPC power was defined as the vector $P_{QPC} = I \cdot V_{bias} - I^2(h/\nu e^2)$, where ν was the bulk filling factor. For each sweep, the electron temperatures found using equation (4.2) were normalized such that the minimum electron temperature was always 20 mK, equivalent to an effective rescaling of α. This minimum electron temperature of 20 mK was measured at the base temperature of our dilution refrigerator via Coulomb blockade thermometry, for quantum dots with cold leads sourced directly from ohmic contacts. We assume in our experiment that all edges are at this minimum temperature when $V_{bias} = 0$. For a dot coupled to a fractional edge, electronic correlations may alter the temperature extracted using equation 4.2. As long as the peak width remains linear in temperature as a result of such behavior, our procedure accurately reports

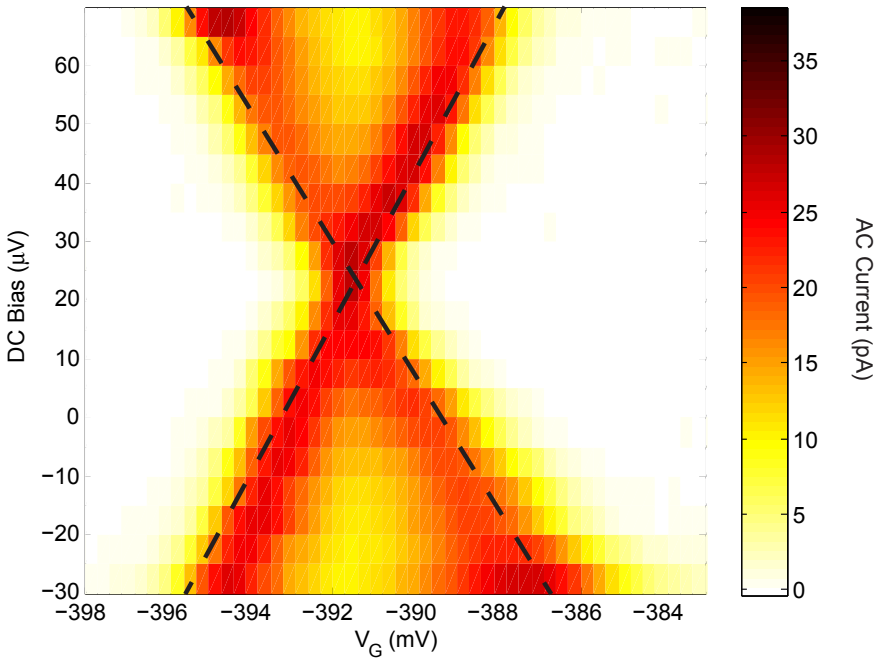

Figure 4.3.2: Coulomb blockade data used to calibrate the downstream quantum dot at a magnetic field of 8.3 T. The lever arm α is calculated from the slopes of the zero-conductance regions, marked by dashed lines.

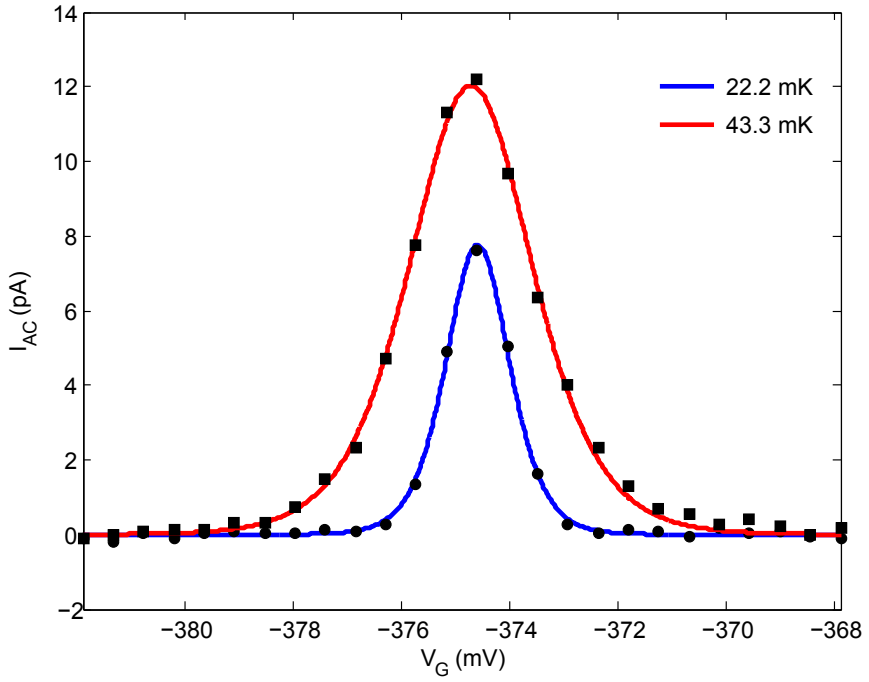

Figure 4.3.3: AC current I_{AC} through the downstream quantum dot as a function of the plunger gate voltage V_G, measured at a magnetic field of 8.3 T. Black circles (squares) correspond to data taken for an injected QPC current $I = 0$ nA ($I = 1.5$ nA). The best fits of the data to equation (2) are shown in blue and red, and give temperatures of $T = 22.2$ mK for $I = 0$ nA and 43.3 mK for $I = 1.5$ nA.

relative edge temperatures. The absolute fractional edge temperatures may then differ from our reported data by an overall normalization.

While all of our reported Coulomb blockade temperatures use the above rescaling to normalize the base temperature to 20 mK, it is also possible to calibrate temperatures using the resistive RuO thermometer on the mixing chamber. In Fig. 4.3.4 such a calibration is plotted, showing how the temperature deduced from Coulomb blockade peaks corresponds to the mixing chamber temperature. The behavior is linear at high temperatures and saturates to the minimum dot temperature of 20 mK at low temperatures due to the decoupling of the electronic system from the lattice. Because the mixing chamber thermometer is not directly coupled to the two-dimensional electronic system, we have chosen to normalize minimum temperatures to 20 mK rather than calibrate using the mixing chamber. From this data we see that a calibration using the mixing chamber thermometer does not significantly alter our results beyond a 140% temperature rescaling at the highest reported temperatures. None of our qualitative claims are changed by such a rescaling, and this temperature increase cannot explain the temperature deficiency discussed in the main text and Section 4.4.

We accumulated several normalized data sets at each value of magnetic field, both with the deflector gates energized and at zero voltage. To determine the increase in temperature at the downstream dot due to heat carried by the outermost edge component, we first separated the data sets into two groups, depending on whether the deflectors were energized or at zero voltage while the data was taken. For each group, the normalized downstream temperatures were then averaged to obtain two vectors containing the mean downstream temperatures for both deflector settings. The QPC powers were similarly averaged, resulting in the power-dependent mean temperatures plotted in Fig. 4.2.1. The difference between the mean downstream temperatures, for equal QPC power, was reported as the excess downstream dot temperature. This procedure was also used for the upstream dot, and for all reported values of the magnetic field. The excess temperatures determined in this way are plotted in the third row of Fig. 4.2.1 of the main paper.

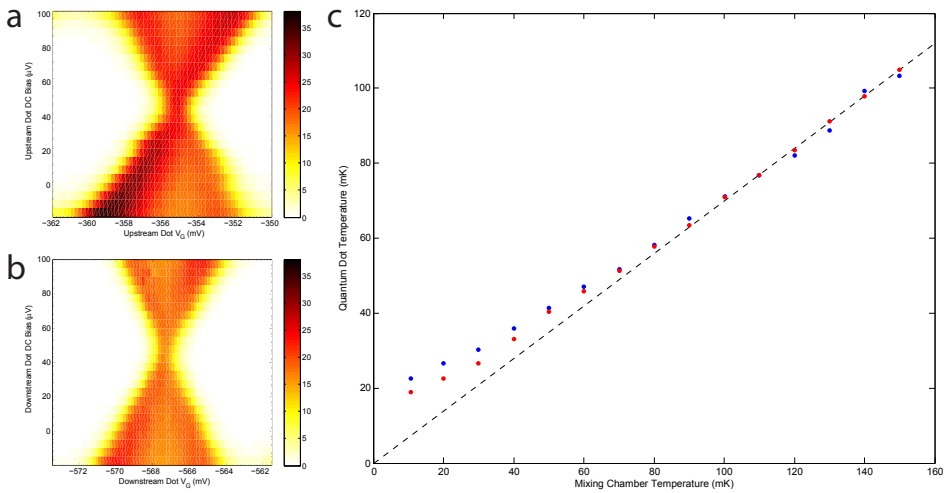

Figure 4.3.4: Comparison of Mixing Chamber and Coulomb Blockade Thermometry, at 6.15 T. Heat is applied to the mixing chamber and temperatures are measured using a resistive RuO thermometer attached to the mixing chamber along with the two patterned quantum dots. a,b) Widths for the CB thermometers are calibrated using the diamonds. c) The widths of our CB peaks are linear in temperature, except for a saturation at 20 mK as the mixing chamber is cooled to 10 mK.

In our experiment, we tune the bulk quantum Hall state to filling factor ν, and apply a voltage V between ohmic contacts O3 and O6. These two contacts are separated by a QPC tuned to have resistance $R \sim 100\ \mathrm{k}\Omega$. When a net current I is injected through the QPC, the electronic occupation of the outermost compressible edge channel deviates locally from its equilibrium distribution. Quantum dots placed 20 μm upstream and downstream of the QPC probe the chemical potential and temperature of this outermost edge. The form of Coulomb blockade peaks monitored during our heat transport measurements suggests that the outer edge internally reaches thermal equilibrium over a distance smaller than 20 μm. However, our charge measurements indicate that chemical equilibration of the outer edge with inner edge channels starts to occur at a distance greater than 20 μm. Thus, at the downstream measurement point the outermost edge has a Fermi occupation function and carries all of the injected current I. For the measurements at magnetic fields of 2.41 T and 3.8 T (bulk $\nu = 3$ and $\nu = 2$), the electrical conductance of this edge is consistent with downstream charge transport by a single integer quantum Hall (IQH) edge. Furthermore, our thermometry measurements show strict downstream heat transport, also consistent with the IQH regime. To determine the expected quantitative outcome of our measurements in the IQH regime, we analyze charge and heat transport by IQH edges in the experimental system described above.

The chemical potential μ of an IQH edge is related to the current I_E that it carries:

$$I_E = \frac{e}{h}\mu. \tag{4.3}$$

In our model, the total number of edge channels on each side of the QPC is equal to the bulk filling ν. However, since only the outermost channel contributes to charge transport on a 20 μm scale, we treat inner channels as inert and consider only the behavior of the outer channel. The two outer edges that carry charge toward the QPC originate in ohmic contacts O3 and O6. The occupations of these incoming edges are therefore Fermi functions,

$$\begin{aligned} f_{in}^{O3}(E) &= f(E - \mu_{in}^{O3}, T_{base}) \\ f_{in}^{O6}(E) &= f(E - \mu_{in}^{O6}, T_{base}), \end{aligned} \tag{4.4}$$

where $\mu_{in}^{O3} = \mu + eV$ and $\mu_{in}^{O6} = \mu$ are the chemical potentials of O3 and O6 and T_{base} = 20 mK is the electron base temperature. At the QPC, the electronic occupations of the outgoing edge modes are forced out of equilibrium. At a distance 20 μm from the QPC these outgoing edges reach thermal equilibrium, with chemical potentials $\mu_{out}^{O3} = \mu + eV - (h/e)I$ and $\mu_{out}^{O6} = \mu + (h/e)I$ determined using equation 4.3. While these chemical potentials can be found simply by considering charge transport, a more detailed analysis of scattering at the QPC is necessary to determine the temperatures of the outgoing edges.

The equilibrium temperature T of an IQH edge is related to the power J_E carried by its excitations according to

$$J_E = \frac{(\pi k_B)^2}{6h} T^2. \tag{4.5}$$

In general J_E can also be calculated from the occupation $n(E)$ and chemical potential μ of an edge, by integrating the power:

$$J_E = \frac{1}{h} \int_0^{\mu} dE \cdot (\mu - E) \cdot (1 - n(E)) + \frac{1}{h} \int_{\mu}^{\infty} dE \cdot (E - \mu) \cdot n(E). \tag{4.6}$$

Here the first integral corresponds to the contribution of hole-like excitations, while the second integral corresponds to particle-like excitations. The 1D relation $g(E) \cdot v(E) = 1/h$ between the velocity $v(E)$ and density of states $g(E)$ was used to simplify the integrals.

Since the outgoing edges in our model have non-equilibrium distributions $n_{out}^{O3}(E)$ and $n_{out}^{O6}(E)$ immediately after the injection of current I, their respective energy currents are determined using equation 4.6. At a distance 20 μm from the QPC, the outgoing edges are in equilibrium. If no energy escapes from the edge as it equilibrates, equation 4.5 then provides a calculation of the expected edge temperatures. With the goal of ultimately finding these temperatures, we therefore consider the forms of the non-equilibrium edge distributions, which depend on the energy-dependent QPC transmission probability $\tau(E)$. This transmission is determined by the differential conductance dI/dV of the QPC, as follows:

$$I = \int_0^{\infty} dE \cdot \tau(E) \cdot (f_{in}^{O3}(E) - f_{in}^{O6}(E)). \tag{4.7}$$

Using τ and the distributions of the incoming edges (equation 4.4), we find

expressions for the non-equilibrium distributions:

$$\begin{aligned} n_{out}^{O3} &= (1-\tau)\cdot f_{in}^{O3} + \tau \cdot f_{in}^{O6} \\ n_{out}^{O6} &= (1-\tau)\cdot f_{in}^{O6} + \tau \cdot f_{in}^{O3}. \end{aligned} \tag{4.8}$$

From these distributions we can then deduce the partitioning of power among the outgoing edges, as well as the outgoing equilibrium temperatures T_{out}^{O3} and T_{out}^{O6}. We find that each outgoing edge carries an equal energy current. Conservation of energy provides a constraint on the total outgoing power:

$$I \cdot V - I^2(h/e^2) = \frac{(\pi k_B T_{out}^{O3})^2}{6h} + \frac{(\pi k_B T_{out}^{O6})^2}{6h} - \frac{(\pi k_B T_{base})^2}{3h}. \tag{4.9}$$

This relationship holds as long as the inner edges remain decoupled from the outermost edge modes. Here the left-hand side specifies the power dissipated by the QPC, while the right-hand side represents the net power carried away by edge excitations. The term $I^2(h/e^2)$ refers to energy dissipated at ohmic contacts, and does not contribute to heating the edge. For completeness, the distributions of the outgoing edges, 20 μm from the QPC, are given below:

$$\begin{aligned} f_{out}^{O3}(E) &= f(E - \mu_{out}^{O3}, T_{out}^{O3}) \\ f_{out}^{O6}(E) &= f(E - \mu_{out}^{O6}, T_{out}^{O6}), \end{aligned} \tag{4.10}$$

In Fig. 4.4.1, numerical calculations of the outermost edge occupation functions are plotted during each stage of scattering at the QPC, for an applied voltage $V = 175$ μV and at bulk filling $\nu = 2$. In panel B, the incoming distributions are shown with the QPC transmission τ extracted from IV data. In panels C and D, the non-equilibrium and equilibrium distributions are plotted for outgoing edges on each side of the QPC. For the equilibrium outgoing distributions, we extract the temperatures T_{out}^{O3} and T_{out}^{O6} over a range of V to determine the dependence of edge temperatures on the QPC power $P_{QPC} = I \cdot V - I^2(h/e^2)$. As shown in Fig. 4.4.2, our model qualitatively explains the cusp in temperature that is observed at $P_{QPC} = 0$.

Using this model, we expect the downstream quantum dot to measure a maximum temperature of 560 mK for $\nu = 2$ and 545 mK for $\nu = 3$. The actual observed maximum temperatures were 55 mK for $\nu = 2$ and 35 mK for $\nu = 3$. Although we observe no charge leakage to inner edge channels on a 20 μm scale, the loss of heat to inner edges is still

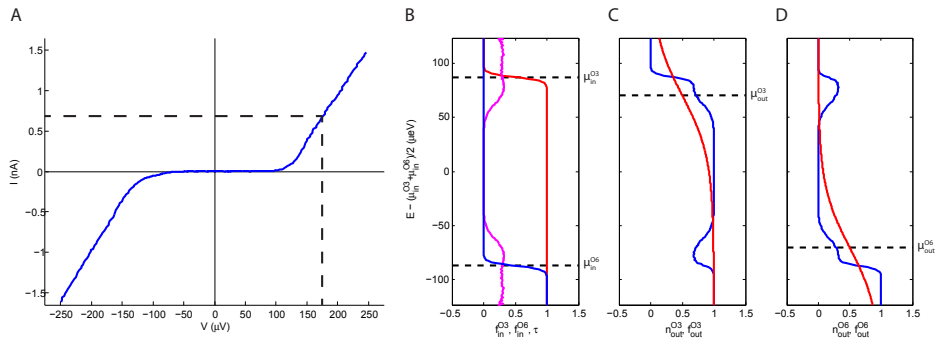

Figure 4.4.1: A) The IV curve of the QPC at bulk filling $\nu = 2$. An applied voltage $V = 175\ \mu$V was used to calculate the distributions shown in (B-D). This voltage and the corresponding injected current are marked with dashed lines. B) The QPC transmission probability τ, calculated from the QPC IV curve, is shown in magenta. In blue (red), the occupation f_{in}^{O6} (f_{in}^{O3}) of the incoming outer edge mode originating at ohmic contact O6 (O3). The chemical potentials differ by $eV = 175\ \mu$eV. C) In blue, the non-equilibrium occupation n_{out}^{O3} of the outermost edge immediately after the injection of current through the QPC. This edge component carries charge toward O3. 20 μm from the QPC, the edge is in equilibrium with the distribution f_{out}^{O3}, shown in red. C) The edge component carrying charge toward O6 has the non-equilibrium occupation n_{out}^{O6}, shown in blue, immediately after current is injected. 20 μm downstream the edge has equilibrated to the distribution f_{out}^{O6}, shown in red.

possible and would decrease the expected temperatures. If all edges equilibrate thermally over a distance smaller than 20 μm, we expect that the power J_E carried by the outermost edge will be divided by the filling factor ν. Using equation 4.5, it follows that the temperature will be divided by $\nu^{1/2}$. For this type of thermal equilibration we thus expect to measure 395 mK for $\nu = 2$ and 315 mK for $\nu = 3$. Whether or not heat escapes to the inner edges, it is still clear from this analysis that in our experiment the majority of the power dissipated in the QPC does not find its way to the outermost edge.

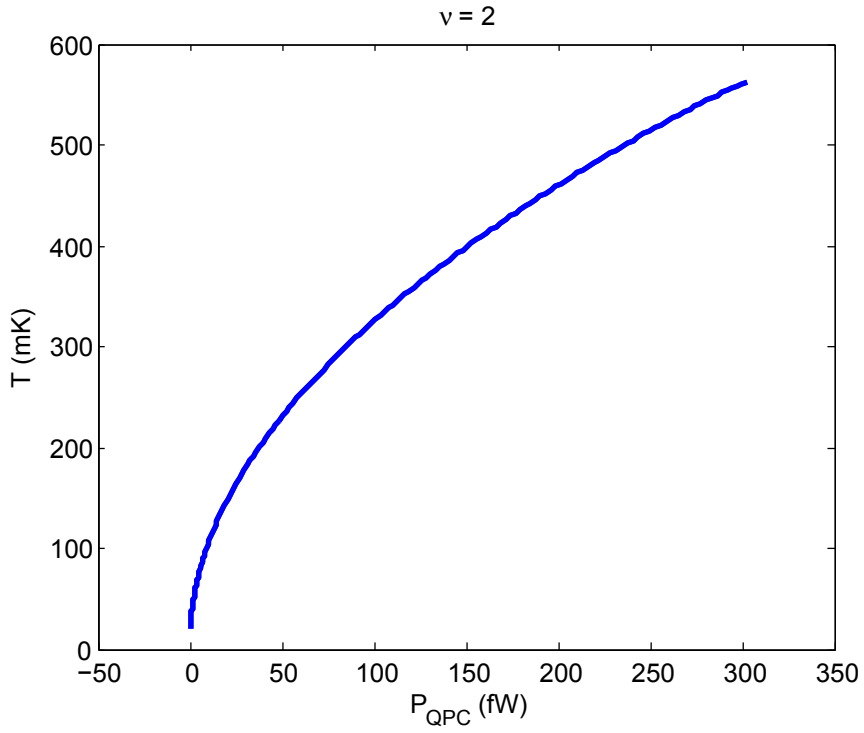

Figure 4.4.2: Expected equilibrium temperatures of the outgoing outermost edges, calculated using the measured QPC transmission τ at $\nu = 2$. Both outgoing edges are expected to have the same temperature. The $\nu = 3$ data give the same temperature as a function of QPC power.

4.5 Bulk Heat Transport

As mentioned in the main text and Section 4.4, we observe temperatures well below what is expected for a system of quantum Hall edges with no energy dissipation. This necessarily means that heat diffuses out of the edges into additional modes in either the bulk of the 2D electronic system or the surrounding crystalline solid. Because we see a bulk contribution to heating when the bulk is at $\nu = 1$ (Columns III and IV of Fig. 4.2.1), but not when the bulk is at $\nu = 2$ or $\nu = 3$ (Columns I and II), and because we don't expect a change of magnetic field to significantly affect heat conduction through the solid, we can attribute the heating at high fields to the $\nu = 1$ electronic system. While we don't know the mechanism of this bulk heat transport in such a strongly insulating state, we suspect it may be associated with low energy spin degrees of freedom that exist at $\nu = 1$.

The presence of this bulk heat transport in the two measurements where we see upstream heat transport attributed to edges requires some additional discussion.[2] Specifically, we need to rule out the possibility that turning our deflectors on and off affects the quantity of heat transported by the bulk to the thermometers, thereby producing a signal unrelated to edge heat transport. Below we describe two experiments specifically designed to address this possibility. Our findings provide two important observations. Firstly, our gates are not completely effective at preventing the flow of heat. We inferred this from the shape of our Coulomb blockade peaks, and checked it explicitly by attempting to block heat flow with a gate. Secondly, if we reduce the length of the deflector gates to the point where there is much less bulk $\nu = 1$ region for heat to diffuse upwards into when the deflectors are off, we observe the same qualitative and quantitative behavior that was presented in the main body of the paper. Both of these observations are discussed more carefully below.

I. Diffusion of heat through gated regions

When our topgates are energized to completely deplete carriers from the underlying 2D electron system, we would expect that energy can no longer be transported by that system. However, heat that manages to diffuse into the lattice can still propagate. Here we will present data suggesting that some heat does indeed diffuse across the depleted

[2] A measurement where bulk heat transport is present without edge heating is given in Section 4.6

regions.

The first indication of such diffusion is taking place can be seen in the form of our Coulomb blockade peaks. The fits we used in the experiment assume that the temperatures of the two quantum dot leads are identical. However, since we are only explicitly heating one side of the dot, a simple model suggests that we should expect leads with different temperatures. This temperature asymmetry should show up as an increased kurtosis in the CB peak shape. In Fig. 4.5.1, we show the one-temperature fit that was used in the main body of this paper along with two alternatives that allow for asymmetric lead temperatures. This particular peak corresponds to the downstream measurement at a magnetic field of 6.2 T and an injected power of 274 fW. The deflector gates are energized, so this peak includes both edge and bulk contributions.

Fig. 4.5.1b presents an alternative fit with an additional fit parameter that allows for different temperatures in the two leads. While the one-temperature fit suggests lead temperatures of 51 mK, the two temperature fit suggests that one of the leads is hotter (60 mK) and the other is colder (39 mK). However, even though the fits are consistently better with the extra parameter, the residuals are not systematically cleaner. Fig. 4.5.2 presents a comparison of the one-temperature and two-temperature fits for the entire range of injected powers that we studied. Below 50 fW of injected power, the one-temperature and two-temperature fits agree exactly, suggesting equal temperature leads. At higher powers, the two temperature fit does suggest a difference in the lead temperatures. Even this asymmetry, however, has to be considered carefully. Because there are nearby peaks (roughly 800 mK away from the peak center, when translated from gate voltage as in Fig. 4.5.1), at high temperatures we can expect them to artificially distort our peak and increase the quality of an asymmetric-temperature fit.

Fig. 4.5.1c presents yet another fit which assumes that the cold lead has the naively expected temperature of 20 mK, corresponding to the observed base temperature for electrons with no intentional heating. The temperature of the hot lead is allowed to vary. With this constraint, the best fit suggests a hot lead temperature of 59 mK. Here, however, the residuals have a pronounced trend that persists for all fits with the 20 mK constraint.

Without strong evidence that a two-temperature fit better describes our measurements, we opted to use a single-temperature fit for the main data presented. None of the qualitative observations of bulk heat transport or upstream heat transport by a neutral edge mode are affected by using the hotter temperature from

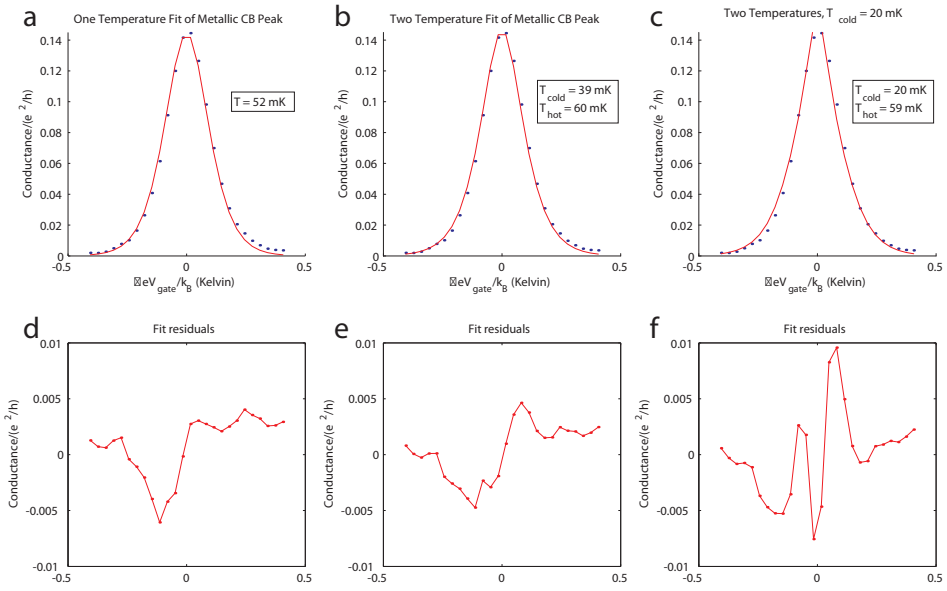

Figure 4.5.1: a) One temperature fit of the CB peak seen downstream at 6.2T and 274 mW of injected power. The deflector gates are energized, so this peak includes both edge and bulk contributions. Additional peaks are centered roughly 800 mK to the left and right of the center of this peak. **b)** Fit obtained by adding an additional parameter allowing for asymmetric lead temperatures. There is no systematic improvement in the residual trend by using such a fit (though the quality of fit obviously improves slightly). **c)** Fit obtained using the same form as panel b, but fixing the cold lead to a 20 mK distribution. This produces a low quality of fit and certainly doesn't describe our data well. **d,e,f)** Fit residuals plotted below the associated fit.

two-temperature fits. Furthermore, the two-temperature fit doesn't solve the temperature deficiency alluded to in the main text or Section 4.4.

We can go further and explicitly test for heat transport across depleted regions by placing a strip of such a region between our heater and our thermometers, as in the device pictured in Fig. 4.5.3. Any heat detected at the thermometers would necessarily have to diffuse through depleted region beneath the vertical gates. Results of this test are depicted in Fig. 4.5.4. Here, we can clearly see that some heat flows through these narrow depleted regions. At the highest injected power, we see the temperature rise from 20 mK to 28 mK with an uninterrupted 2D and a temperature rise to 22 mK with

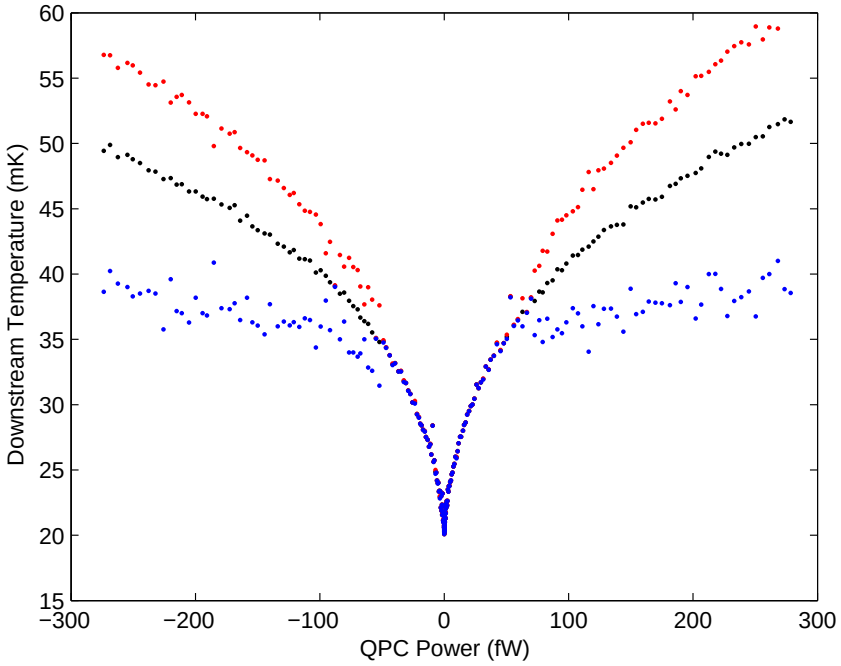

Figure 4.5.2: Temperature fit of the CB peak seen downstream at 6.2T as a function of injected power. Black denotes the one-temperature fit (as in Fig. S7a), and red and blue denote the hot and cold temperatures of a two-temperature fit (as in Fig. S7b). They agree perfectly at low injected powers, but begin to diverge beyond 50 fW.

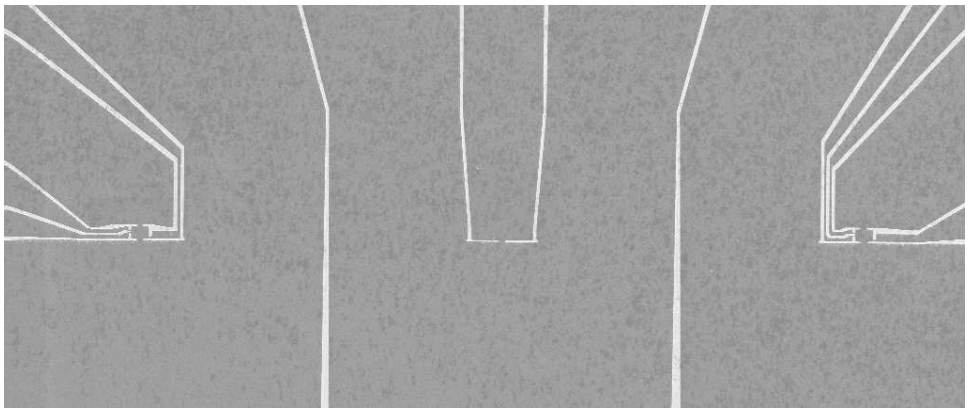

Figure 4.5.3: Device designed to explicitly test for heat leakage across a depleted barrier. When the vertical gates are energized, the 2D systems on the left and right are completely isolated (electrically) from the 2D system with the heater in the center.

the 2D depleted beneath the vertical gates. This small heat diffusion through gated regions is qualitatively consistent with our observation of heating in the cold leads of our quantum dots, as mentioned above. The fact that the temperature is reduced from the ungated value (22 mK versus 28 mK) provides additional evidence that the 2D electron system is responsible for the observed bulk heat transport at high fields.

II. Geometric Diffusion Considerations

Because we only detect neutral mode heating when there is a bulk contribution to the heating signal, we have to ensure that there is no significant change in the bulk contribution as we energize and deenergize the deflector gate. It would appear plausible, for instance, that by turning on the deflector gate we reduce the area over which the bulk heat can diffuse. Specifically, with the deflector gate on, heat can no longer diffuse up into the 2D region between our heater and our thermometers. As a result, one may conjecture that more heat will be directed towards the thermometers resulting in a higher temperature unassociated with quantum Hall edge physics. The first indication that this redirection of heat isn't relevant is the above observation (from CB peak shapes and direct measurements) that heat does indeed partially diffuse through depleted regions. A more convincing test, however, consists of altering the

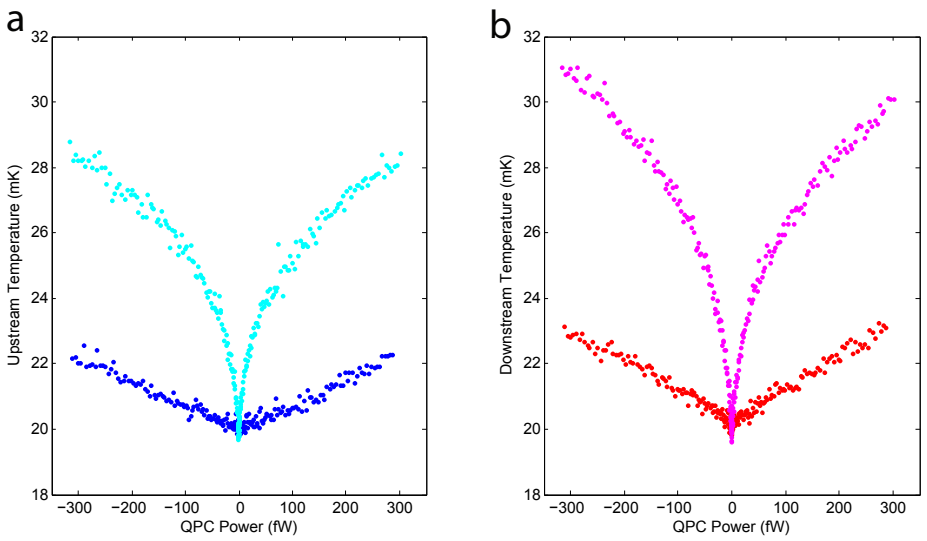

Figure 4.5.4: Heat transport across a depleted barrier. The cyan curve depicts temperature measured upstream from the heater when the vertical gates are deenergized. The blue curve depicts the temperature when the vertical gate is energized, so heat must diffuse across a depleted region. The magenta and red curves are the corresponding traces for the downstream dot. All data was taken at 8.3 T, corresponding to column IV in Fig. 4.2.1.

geometry of the bulk to reduce the effect of this geometric distortion.

To this end, consider the device shown in Fig. 4.5.5b. It is identical to the devices used for measurements in the main body of the paper, but with a shorter deflector gate length (8 um instead of 15 um). At 8.3 T, we expect an edge structure as shown in Fig. 4.5.5, with two separated edges: one corresponding to the boundary between vacuum and $\nu = \frac{2}{3}$ and the other corresponding to the boundary between $\nu = \frac{2}{3}$ and $\nu = 1$, as $\nu = 1$ is the bulk filling factor and $\nu = \frac{2}{3}$ is the edge that we detect with our local injection measurements. In the 8 um deflector device, with the deflector deenergized, we measure a slightly elevated resistance ($1.19\, R_K$), indicating that the inner edge corresponding to the transition from $\nu = \frac{2}{3}$ to $\nu = 1$ is being backscattered (transmission coefficient of 52% for that inner edge). This indicates that the $\nu = 1$ bulk is largely closed off in this deflected region, so we would expect very little bulk heat to diffuse upwards through this narrow constriction. If the difference in upstream heating displayed in Fig. 4.2.1(IV) of the main paper is due to a redirection of bulk heat flow, we would expect almost the same difference between the temperature measured in the 15 um deflector device (Fig. 4.5.5a) and the 8 um deflector device (Fig. 4.5.5b).

The data from these measurements are presented in Fig. 4.5.6. The blue and red points correspond to temperatures measured in the device from Fig. 4.5.5a with deflectors off. The cyan and magenta points correspond to temperatures measured in the device from Fig. 4.5.5b, also with deflectors off. These undeflected temperatures in the two devices are very close, to within the data spread. For reference, the temperature associated with turning on the deflectors (which results in the same geometry for the two devices) is displayed in green and orange.

From these, we can infer that the excess temperature found in the green and orange traces is indeed associated with a hot $\nu = \frac{2}{3}$ edge, as this edge is the only component of the system that is significantly altered as deflector gates are turned on in the device from Fig. 4.5.5b.

In Section 4.6, we present yet another device, where the gate-defined edge is replaced by a sharp mesa-defined edge. If the excess upstream heat was due to a redirection of bulk heating, we would expect an elevated temperature in that situation, given that the device possesses a nearly identical bulk geometry compared with the gate-defined edge. Here, however, we don't see any heat associated with the edge at 6.2 T (Fig. 4.6.2a). This provides even further evidence that the observed upstream heat is due to FQH edge structure and is independent of the measured bulk heat transport at

$\nu = 1.$

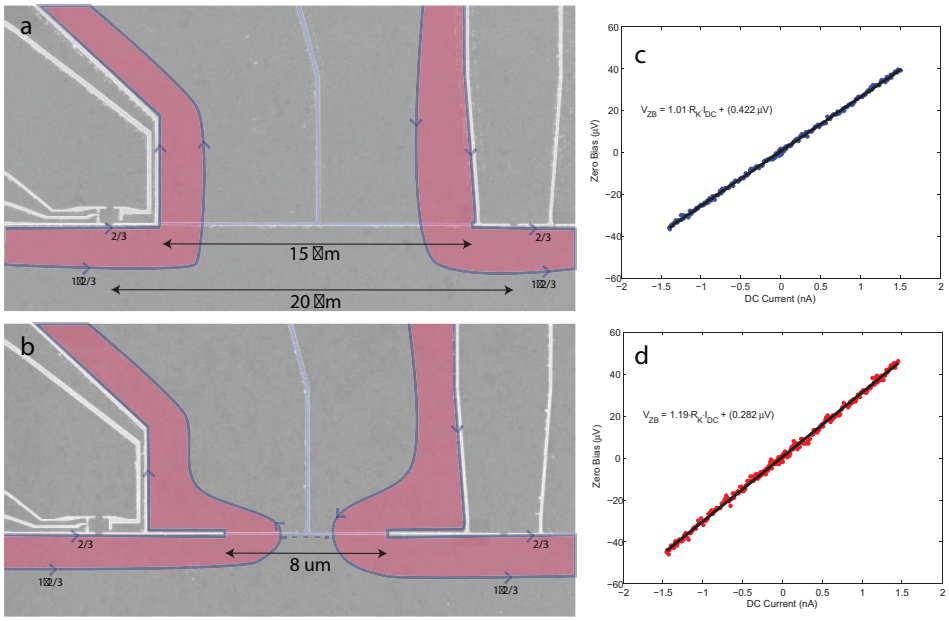

Figure 4.5.5: A device to test the effect of geometric diffusion considerations. **a)** SEM image of device identical to that used for data in the main paper. Edge labels correspond to what is expected at a field of 8.3T, based on our local and global R_{xy} measurements. **b)** SEM image of a device with a narrower region through which edges can be deflected. From the elevated resistance shown in panel d, we know that the inner edge is partially backscattered. **c)** Copy of the ΔV_{ZB} versus I_{DC} curve from Fig. 4.3.1, demonstrating that the resistance in the deflector channel is the same as the bulk value $(1.01R_K)$, indicating that the $\nu = 1$ state is fully connected from the top to the bottom of the image in panel a. **d)** A corresponding ΔV_{ZB} versus I_{DC} curve for the device in panel b. The elevated resistance $(1.19R_K)$ indicates that the inner edge, which has a conductance of $\frac{e^2}{3h}$ is 52% transmitted. This suggests that the $\nu = 1$ state is connected through a narrow channel in this device, providing much less room for heat to diffuse upwards compared to the device in panel **a**.

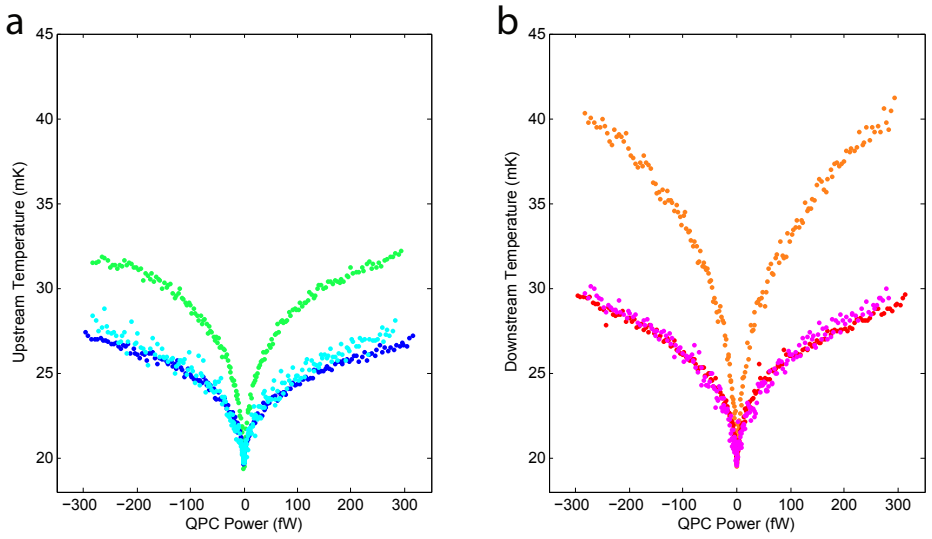

Figure 4.5.6: The blue and red points correspond to temperatures measured in the device from Fig. 4.5.5a with deflectors off. The cyan and magenta points correspond to temperatures measured in the device from Fig. 4.5.5b, also with deflectors off. These undeflected temperatures in the two devices are very close, to within the data spread. For reference, the temperature associated with turning on the deflectors (which results in the same geometry for the two devices) is displayed in green and orange. From this we can conclude that the observed upstream heating is not due to a redirection of bulk heating upon energizing of deflector gates. **a)** Upstream. **b)** Downstream.

4.6 The Fractional Quantum Hall Edge at $\nu = 1$

The spatial separation between compressible edges is determined largely by the sharpness of the confining potential. At $\nu = 1$, the presence of FQH edge structure requires a shallow confining potential (compared to the magnetic length or Fermi wavelength), as well as a high mobility 2DES (as is always required for FQH physics). In this section, we will present data from an edge defined through a mesa etch, creating a steeper confining potential than what was presented in the main paper. As a result of the steeper confinement, we find edges of type III and IV (from Fig. 4.2.2) when the bulk is at $\nu = 1$. The gate-defined edge, as a reminder, had edges of type IV and V at bulk filling $\nu = 1$. From the table in Fig. 4.2.2, we can see that charge transport (R_{xy} and R_L) cannot discriminate between the type III and type IV edges. In this section, we will present evidence that both types of edge can exist in a single sample, and that they can be distinguished by monitoring upstream heat transport.

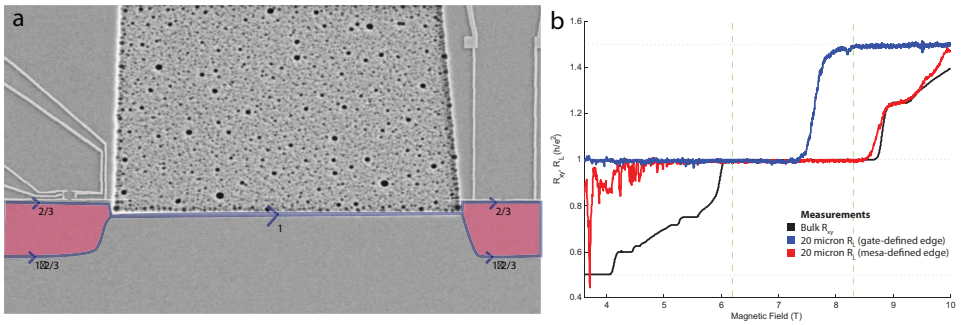

Figure 4.6.1: a) Modified device to study heat transport along a sharper edge. The gate defined edge (studied in the main paper) allowed for a $\nu = 2/3$ edge to form outside the $\nu = 1$ bulk (blue trace in panel **b**). The mesa-defined edge here is sharper, and the sharp density gradient may preclude FQH edge structure outside the $\nu = 1$ bulk. This image is of a device with 40 μm between heater and thermometer, while the device measured had 20 μm between heater and thermometer, to match the device presented in the main paper. **b)** R_L (red) for the device in panel **a**. The reduced resistance of the edge (red versus blue) at 8.3 T when switching from a gate-defined to a mesa-defined edge suggests that the originally separated FQH ($\nu = 2/3$ and $\nu = 1 \rightarrow 2/3$) channels are brought close together, allowing charge to equilibrate between them. While the device is drawn with an edge of type III (from Fig. 4.2.2 of the main paper), an edge of type IV cannot be ruled out from charge transport, either locally (R_L) or globally (R_{xy}).

In Fig. 4.6.1, we present an SEM image of the device under consideration. The

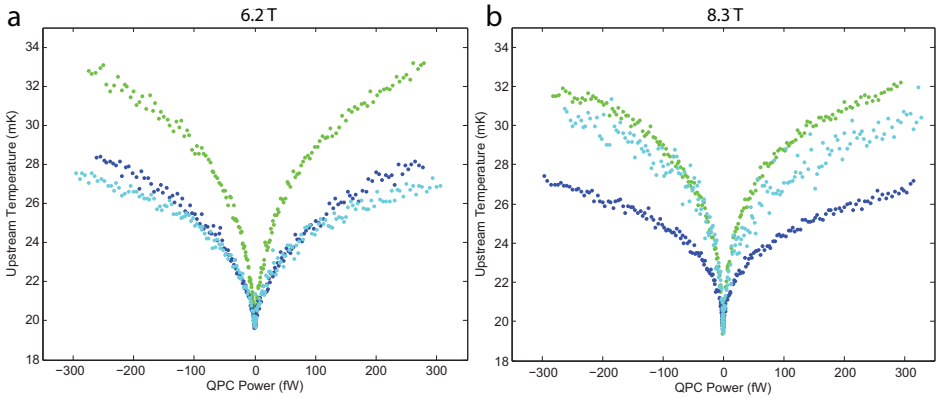

Figure 4.6.2: Upstream thermometry to identify FQH structure in the $\nu = 1$ edge. Dark blue curves depict background upstream heating, which we attribute to the bulk. The green curve depicts the heat observed with a gate-defined edge connecting heater and thermometer. The light blue curve depicts upstream heat observed with a sharper mesa-defined edge connecting heater and thermometer. **a)** At low fields, the upstream heating from the mesa-defined edge closely matches the background, suggesting no excess heat is carried by the edge. **b)** At high fields, there is a similar amount of upstream heating by both sharp and shallow edges, both appreciably above the background.

device geometry and substrate used are identical to those used for the device presented in the main paper. Using a wet-etching procedure, we are able to remove material between the QPC heater and the QD thermometer. This creates a physical boundary to the sample along which the edge propagates. The density in the 2DES must drop to zero across this edge, which can be happen over a shorter length scale than for an edge created by depleting the 2DES via electrostatic gating.

To demonstrate that this edge is sharper, we can repeat our local charge transport measurements (Fig. 4.6.1b, R_L in red). The observed enhanced conductance at any given field (red compared to blue) is a result of either more edges participating in transport, or a greater conductance of those edges participating. This is precisely what is expected if the edges are confined with a steeper potential. Here we will focus on behavior on the edge of the $\nu = 1$ bulk (6.2 T and 8.3 T). From the charge transport measurements, we cannot distinguish the exact edge structure at either field (see edges III and IV in Fig. 4.2.2).

To distinguish between these two possible edge structures, we can perform

upstream thermometry measurements. Because we have created our edge via etching the mesa, we cannot control for bulk heating by energizing and deenergizing deflection gates. However, by using an identical geometry to the gate-defined device, we can still identify the presence or absence of excess heat due to the edge. This thermometry measurement is presented in Fig. 4.6.2, with data from the edge-defined device in light blue. For comparison, data from the gate-defined device taken at the same fields is reproduced in dark blue and green (identical to upstream data in columns III and IV of Fig. 4.2.1 in the main paper).

At 6.2 T, we see that the temperature detected upstream (light blue) closely matches the temperature associated with bulk heating in the original device (dark blue). This is consistent with no heat being transported by the edge. The lack of upstream heat carried by the edge allows us to classify it as a simple IQH $\nu = 1$ edge (type III in Fig. 4.2.2), similar to what was observed at bulk fillings of $\nu = 2$ and $\nu = 3$ in the original device.

At 8.3 T, the temperature measured upstream (light blue in Fig. 4.6.2b) appears to be elevated, closely matching the temperature seen when a $\nu = 2/3$ edge connects the heater to the upstream thermometer in the original device (green curve). Recall that in the original device, this $\nu = 2/3$ edge was detectable via measurement of R_L (blue curve in Fig. 4.1.2). Here the charge signature has vanished ($R_L = R_{xy}$), but the nearly identical upstream heating strongly suggests that the $\nu = 2/3$ edge is still present (edge IV in Fig. 4.2.2). These measurements increase our confidence in assigning edge IV to our observations at 6.2 T in the original device.

4.7 Length Dependence of R_L

If two separated co-propagating edge channels are filled to different chemical potentials, we expect charge to slowly equilibrate between them. By varying the length between injector (the central QPC), and detector (a downstream QPC), we can learn how this equilibration takes place.

Data from 3 separate samples, all from the same wafer, are shown in Fig. 4.7.1. At 6.2 T, R_L is always found to be quantized to 1 (though it isn't so clear for the 1 μm device due to large conductance fluctuations). Focusing on data from sample 3 only, we see that a transition from $R_L = 1$ to $R_L = 3/2$ occurs at 7.2 T, for lengths between 10 μm and 40 μm. The fact that all the R_L curves from sample 3 lie on top of each other

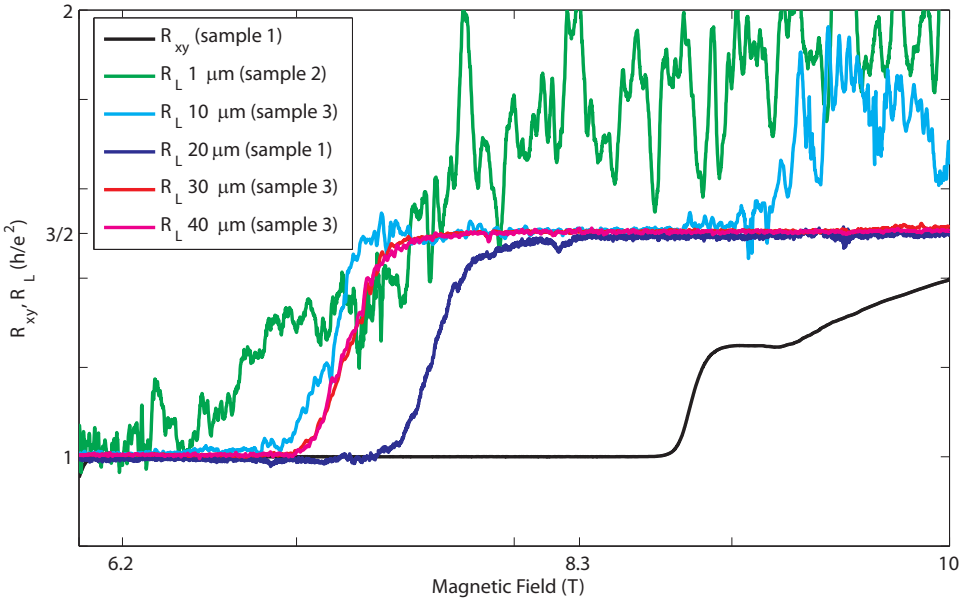

Figure 4.7.1: Length dependence of R_L using data obtained from 3 different samples. No evidence of charge equilibration is observed over 10s of microns.

indicates that the edges can maintain different chemical potentials over 10s of microns without equilibrating.

The slightly higher transition field for sample 1 (20 μm) compared to sample 3 is likely due to a slightly different density frozen in beneath the gates during cooldown. From the difference in transition fields (7.2 T versus 7.6 T) we can estimate that there is 5% more density frozen in near the gates in sample 1 compared to sample 3. Bulk R_{xy} values do not vary by such a large amount between samples in this wafer.

4.8 Molecular Beam Epitaxy Information

All samples used in this experiment were obtained from the wafer LP 11-18-08.1, grown at Bell Laboratories in Murray Hill, NJ, by Loren Pfeiffer and Kenneth West. Fig. 4.8.1 has the details of the growth.

11_18_08.1 - Actual Results

39

Substrate: F-87246 B3
As Temp: 289
As Set: 9.5e-6
Comments: Einstein quiet & gatable
For Jim Eisenstein

label	relay	rate	temp	set pt
Ga7	2	2.8187	878.000	877.500
Ga5	3	1.8668	970.000	969.000
Al4	5	0.8944	971.000	970.000

Layer#	Layer Type	Thickness	Time	Total Time	Al4	Sub (V)	Si (A)	C (A)
1	chgSi chgC As10	0.00	60.00	60.00	---	28.114	0.003	0.008
2*	Ga7As10	500.00	177.39	237.39	---	28.109	0.003	0.009
3* (10)	PauseAs10	0.00	50.00	287.39	---	28.106	0.004	0.010
22*	Ga5As10	30.00	16.07	2349.94	---	28.109	0.002	0.009
23*	PauseAs10	0.00	10.00	2359.94	---	28.106	0.002	0.008
24* (100)	Ga5Al4As10	100.00	36.22	2396.15	0.324	28.106	0.002	0.008
322	t-652.0	0.00	10.00	8572.51	---	28.105	0.003	0.008
323	Ga5Al4As10	2500.00	905.40	9477.91	0.324	28.108	0.002	0.010
324	chgTemp As10	0.00	110.00	9587.91	---	0.010	0.002	0.011
325	chgTemp As10	0.00	2.00	9589.91	---	14.564	0.002	0.010
326	chgSi As10	0.00	15.00	9604.91	---	14.564	6.913	0.011
327	SiAs10	0.00	25.00	9629.91	---	14.566	6.913	0.009
328	chgSi As10	0.00	10.00	9639.91	---	14.566	0.000	0.010
329	Ga5Al4As10	14.00	5.07	9644.98	0.324	14.564	0.002	0.010
330	t-430.3	0.00	10.00	9654.98	---	14.563	0.002	0.008
331	chgTemp As10	0.00	85.00	9739.98	---	29.843	0.002	0.009
332	startTempAs10	0.00	2.00	9741.98	---	28.103	0.002	0.010
333	PauseAs10	0.00	120.00	9861.98	---	28.104	0.002	0.009
334	t-642.1	0.00	10.00	9871.98	---	28.108	0.002	0.010
335	Ga5Al4As10	600.00	217.30	10089.28	0.324	28.110	0.002	0.008
336	Ga7Al4As10	700.00	188.52	10277.80	0.241	28.110	0.002	0.008
337	Ga7As10	300.00	106.43	10384.23	---	28.108	0.002	0.007
338	PauseAs10	0.00	100.00	10484.23	---	28.105	0.002	0.010
339	Ga7Al4As10	700.00	188.52	10672.76	0.241	28.108	0.002	0.011
340	Ga5Al4As10	600.00	217.30	10890.05	0.324	28.109	0.003	0.010
341	chgTemp As10	0.00	110.00	11000.05	---	0.010	0.002	0.009
342	chgTemp As10	0.00	2.00	11002.05	---	14.567	0.003	0.009
343	chgSi As10	0.00	15.00	11017.05	---	14.566	6.913	0.009
344	SiAs10	0.00	60.00	11077.05	---	14.563	6.913	0.009
345	chgSi As10	0.00	10.00	11087.05	---	14.563	0.000	0.010
346	Ga5Al4As10	14.00	5.07	11092.12	0.324	14.564	0.004	0.009
347	t-428.4	0.00	10.00	11102.12	---	14.564	0.002	0.011
348	chgTemp As10	0.00	85.00	11187.12	---	29.843	0.006	0.010
349	startTempAs10	0.00	2.00	11189.12	---	28.104	0.006	0.010
350	PauseAs10	0.00	120.00	11309.12	---	28.104	0.003	0.008
351	Ga5Al4As10	866.00	313.63	11622.75	0.324	28.109	0.002	0.009
352	Ga5As10	100.00	53.57	11676.32	---	28.105	0.002	0.008
353	t-650.6	0.00	10.00	11686.32	---	28.106	0.004	0.009
354	chgTemp As10	0.00	2.00	11688.32	---	8.059	0.004	0.010
355	chgSi chgC As10	0.00	60.00	11748.32	---	8.059	0.392	0.399
356	BeepAs10	0.00	10.00	11758.32	---	8.057	0.392	0.399

EISENSTEIN

total layers: 356
total time: 11758.32 sec.
total thickness: 24394.0 A.

SAMPLE: 11-18-08.1 STRUCTURE: 2Dx1 MEASURED: 11/24/2008 1:42 PM
POSITION: A DARK CONTACTS: corners MANUAL CONTROL
COMMENTS:
SOURCE CURRENT: 10.0uA MAGNET CALIBRATION (G/A): 153.0 MAGNET CURRENT (A): 3.0
T: 297.2 Ro: 3.5573E+3 Rh: 2.6179E+7 M: 7.3591E+3 D: 2.3874E+11
T: 77.5 Ro: 1.6486E+2 Rh: 3.5620E+7 M: 2.1607E+5 D: 1.7546E+11
T: 3.8 Ro: 3.3998E+0 Rh: 4.0316E+7 M: 1.1858E+7 D: 1.5502E+11
AFTER LIGHT
T: 3.8 Ro: 2.5385E+0 Rh: 2.2876E+7 M: 9.0115E+6 D: 2.7321E+11

17.8M 2.32"

Figure 4.8.1: Wafer Structure: LP 11-18-08

5

The Quantum Spin Hall Effect in HgTe Quantum Wells

The quantum Hall effect creates chiral edge channels that carry currents around the perimeter (edge) of a sample in a direction governed by the magnetic field. Positively charged particles will circulate clockwise, and negatively charged antiparticles will circulate counterclockwise. Both contribute to a clockwise current. Switching the field direction switches the direction of this current. Furthermore, backscattering of injected particles is prohibited because of the lack of backwards-moving channels on a any given edge. To turn around, a particle would have to tunnel across the incompressible bulk of a quantum Hall sample.

It is hard to imagine this occurring at zero magnetic field. However, in systems with strong spin-orbit interactions, such a phenomenon is indeed possible. The spin-orbit interaction creates a strong correlation between the spin of an electron and the direction it is traveling. Clockwise-moving electrons will prefer to have their spin point up, and counterclockwise-moving electrons will prefer to have spin down. To turn around, an electron will have to either flip its spin (and stay on the same edge), or

tunnel across the sample (and maintain its spin). Scattering between the counter-propagating Kramers pairs within an edge is predicted to be impossible without explicitly breaking time-reversal symmetry.

For such a phenomenon to be observable, this one dimensional channel must be the only component carrying charge in a sample (as is the case in the quantum Hall effect). The bulk gap in the quantum Hall effect arises from the quantization of kinetic energy by a magnetic field. The gap in the HgTe samples we use to measure the quantum spin Hall effect is a conventional insulating gap that arises from Bragg scattering of electrons in a periodic potential. However, the strong atomic spin-orbit interaction induced by heavy atoms (strong core electric fields in mercury atoms) switches the energetic ordering of two bands at the location of the gap in the Brillouin zone.[8][1]

Without the strong spin-orbit interaction, those bands would have the opposite ordering (in energy), creating a gap with more conventional ordering. At any transition between these gaps will force the formation of a one-dimensional channel that has a conductance of e^2/h. The prevention of backscattering should make this quantization robust and independent of the length of that 1D channel. Indications of such a channel (the quantum spin Hall or QSH effect) was first reported in [36]. Two good reviews are [37, 43].

5.1 Outline of previous work

We'll begin by discussing the most important observations from early QSH experiments carried out at the University of Würzburg. After this, we'll describe a systematic way to probe the conductance of a topologically protected, bi-directional edge (this is different from the unidirectional QHE edge). By using this technique on samples grown in Würzburg (lithography done at Harvard), we have been able to identify and characterize the resistance of quantum spin Hall edges.

The original work [36] describing the QSH effect clearly demonstrated that samples with a wide quantum well, in which band inversion was expected, showed a dramatically lowered resistance compared to samples with a thinner well (no band inversion, no edge channels). This was accomplished using the geometry shown in Figure 5.1.1.

[1] Actually, HgTe is a semimetal with no gap. However, confinement in one dimension (as in a 2DES) can create the desired inverted bandgap. Strain also should work.

In such a geometry, the ohmic contacts are supposedly connected by ideal one dimensional QSH edges, each with a resistance of R_k. Thus, the two terminal resistance between opposite contacts is $3R_k \parallel 3R_k = \frac{3}{2}R_k$. The resistance obtained by dividing the voltage drop across two middle contacts ($I/2 \cdot R_k$) by the total current flowing across the sample (I) should be $\frac{1}{2}R_k$.

In samples with small dimensions ($L \approx 1\,\mu$m), the transverse resistance was found to be very close to the measured value of $\frac{1}{2}R_k$. This can be taken as evidence that, in these small samples, the edge channels behave almost as ideal (non-backscattering) channels connecting ohmics. Even in these small samples, however, the measured resistance was never sharply quantized (as compared to typical data from quantum point contacts or the quantum Hall effect) over any range of topgate voltage (corresponding to tuning the Fermi energy through the gap).

The elevated resistance observed in larger samples (and some 1 μm samples as well) suggests that some scattering can occur. From data in [36], we see that a sample with mobility in the range of $\mu = 10^5 \frac{\text{cm}^2}{\text{Vs}}$ and an edge length of 20 μm has a resistance of roughly $6 - 7\,R_k$ (data from Figure 4 of [36], assuming equal partitioning of current between the top and bottom edges of sample as depicted in Figure 5.1.1). No scattering along the edge would provide an ideal conduction channel with resistance $1\,R_k$. The higher resistance would correspond to roughly $5 - 6$ sites along the edge at which the edge fully equilibrates (or even more sites with partial equilibration). This, in turn, corresponds to a scattering length of a few microns.

Note that calculating resistances for ideal QSH samples depends only on the number and configuration of contacts around the edge (topology) and not the actual spacing of these contacts (geometry). This can be tested by warping the geometry between contacts and identifying nonlocal transport signals, and was checked in [51].

Finally, it was observed that large perpendicular magnetic fields were effective at increasing the resistance of the sample, suggesting that breaking time-reversal symmetry may destroy the protection of edge channels.

5.2 Measuring Quantum Spin Hall Electrical Resistances

The sample we used to quantify QSH behavior were grown in the group of Laurens Molenkamp at the University of Würzburg. Lithography was carried out in the

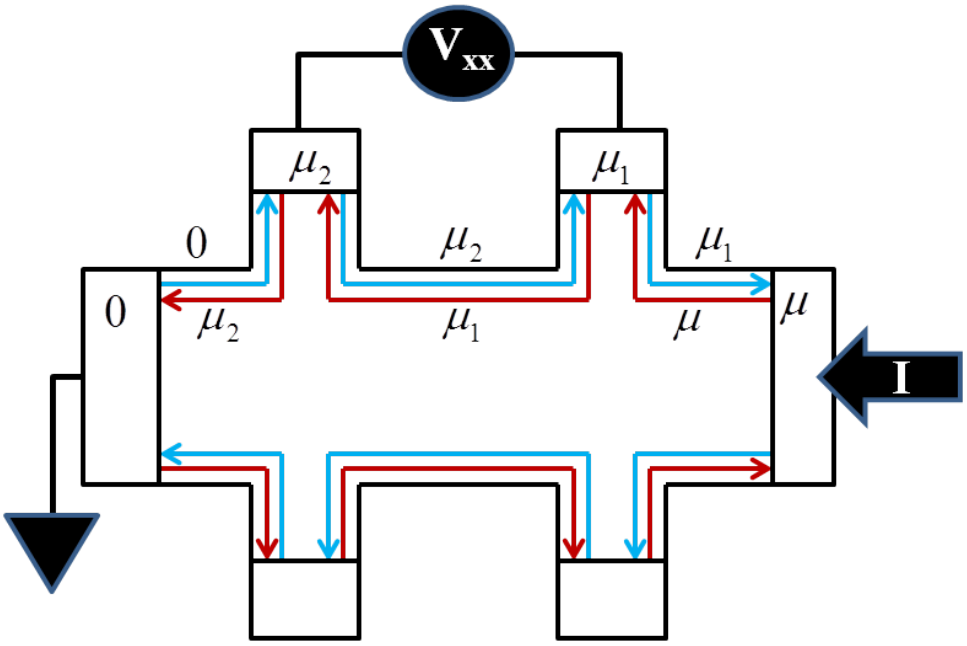

Figure 5.1.1: In a simple Hall bar geometry with six contacts, half of the injected current will flow along the top edge of the sample, with the other half flowing along the bottom. Each edge connecting adjacent ohmics has a resistance of $R_k = h/e^2$. The measured voltage ($V_{xx} = I/2 \cdot R_k$) divided by the total current gives a resistance of $R_{xx} = h/(2e^2)$. Note that this should only depend on the number and configuration of the contacts (topology) not on the actual spacing of them (geometry).

cleanroom at Harvard, and measurements were done here as well. The growth structure of the wafer is provided in Figure 5.2.1. For the (001) orientation of growth in the z-direction, a well thickness of over 6.3 nm should correspond to an inverted band structure in the 2D bulk. The sample has a mobility and density of $\mu = 94,000 \frac{\text{cm}^2}{\text{Vs}}$ and $n = 3.78 \times 10^{11} \text{cm}^{-2}$.

The wafer was grown with intrinsic doping, creating a metallic 2DES prior to intentional depletion of carriers via the gate effect. The devices we created are depicted in Figure 5.2.2. Mesas are defined via reactive ion etching, and ohmics are made by depositing titanium and gold. Without etching, contact resistances of $\approx 5\,\text{k}\Omega$ are obtainable on $(300\,\mu\text{m})^2$ areas. Lower resistances (in the range of Ohms) can be obtained by removing material via RIE before depositing metal.

To define the regions of the mesa that will be [topologically] insulating, we put

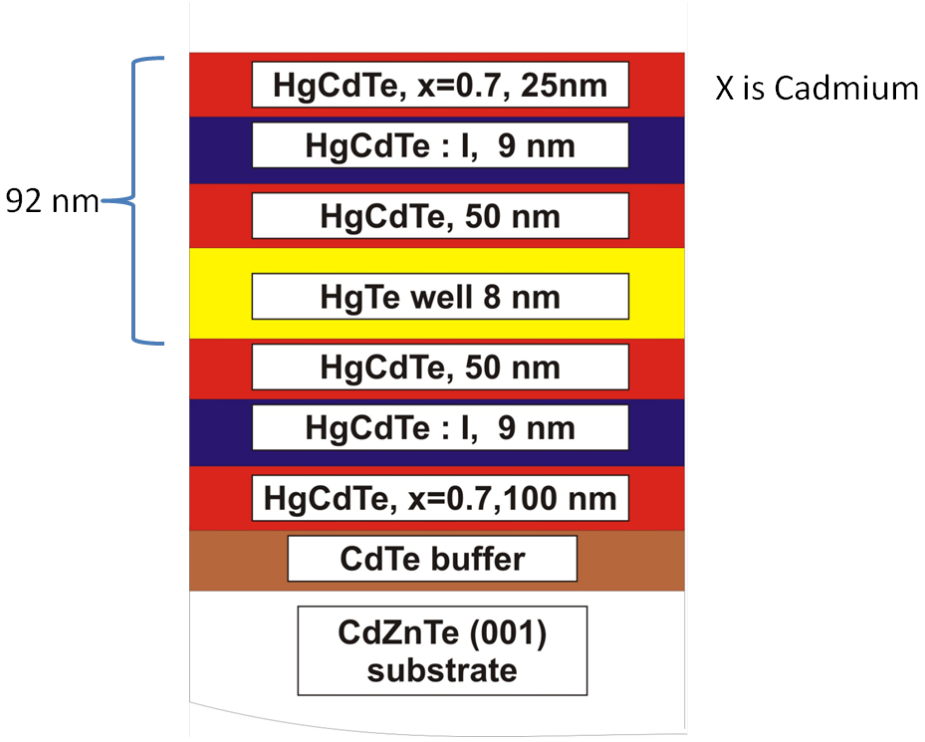

Figure 5.2.1: Growth structure of HgTe/CdHgTe wafer used for measurements.

down a topgate (insulated from the sample with silicon oxide). Energizing the gate (red in Figure 5.2.2) removes carriers and can be used to tune the Fermi energy of the sample to lay within the gap. The geometry is designed to create short edges (roughly 2 μm) between each Ohmic contact. Assuming the bulk is insulating, we would expect these QSH edge states to provide one conduction channel ($R = R_k$) between each pair of contacts. Every edge is lithographically identical, allowing us to obtain many measurements of this QSH resistance.

To obtain the six-contact topology used in the original QSH measurements with this eight-contact sample, we can simply ground three adjacent contacts (and draw current from all three). We can then repeat the measurement described in Figure 5.1.1. As we change the chemical potential in the gated (red) region to lie inside the gap, we find that the transverse resistance of the device approaches $V_{xx}/I = R_k/2$ (Fig. 5.2.3b). However, at various gate voltages (while still remaining in the gap), the resistance is higher or lower than the expected value.

A lower resistance is only possible if additional transmission channels are present (Fig. 5.2.3d). This can occur if the effect of the gate is not uniform, or if the disorder potential is very rough. A higher resistance can only occur if the edge is not perfectly transmitted. This can occur if there is a time-reversal breaking defect present. However, because edges are spin-polarized, partial reflection of an electrical current will require a sink for the spin current. The resulting spin accumulation would have to relax (perhaps to phonons) or diffuse out of the region.

However, there are other ways to obtain the observed resistance of $R_k/2$. If the edge between the voltage probes has a high resistance $> R_k$, but current is partitioned preferentially towards the other side, a similar voltage drop may be recorded. To proceed, it would be better to extract the resistance of a single edge directly, instead of an agglomerate of many edges at once.

The simplest strategy that identifies the resistance of individual edges (in a situation where contact resistances are high) is to make two measurements with different current injection configurations (Fig. 5.2.4a,b). By measuring V_4, V_1, U_1, and U_4 it is possible to extract both R_1 and R_4. By repeating similar measurements for all edges, a map of edge resistances can be made (Fig. 5.2.4c). From here, it is clear that the resistances are distributed over a large range, from close to 1 R_k to roughly 4 R_k. These resistances were averaged over a range of gate voltages within the gap. A plot of resistance for a single edge as a function of gate voltage is given in Figure 5.2.5.

5.3 Characterizing Fluctuations

Perhaps the most prominent feature in all of this data are the large fluctuations in conductance. Understanding these is vital to engineering clean devices (eventually with superconducting contacts). In the first sample measured (all the data presented so far), these fluctuations were always a function of gate voltage (and not time), but they wouldn't reproduce upon sweeping back and forth. This is presumably due to charging at either the oxide interface or within the dopant layer of the grown structure.

In a more recent sample, we were able to reproduce gating behavior and follow the conductance oscillations of an edge while changing the magnetic field and DC current bias (Fig. 5.3.1). From these measurements, we find that there is no indication of

periodic B-dependence (as would be expected from ballistic resonances enclosing some area). The sharp decrease in the amplitude of fluctuations (Fig. 5.3.1a) with a small DC current bias (10 nA) remains unexplained.

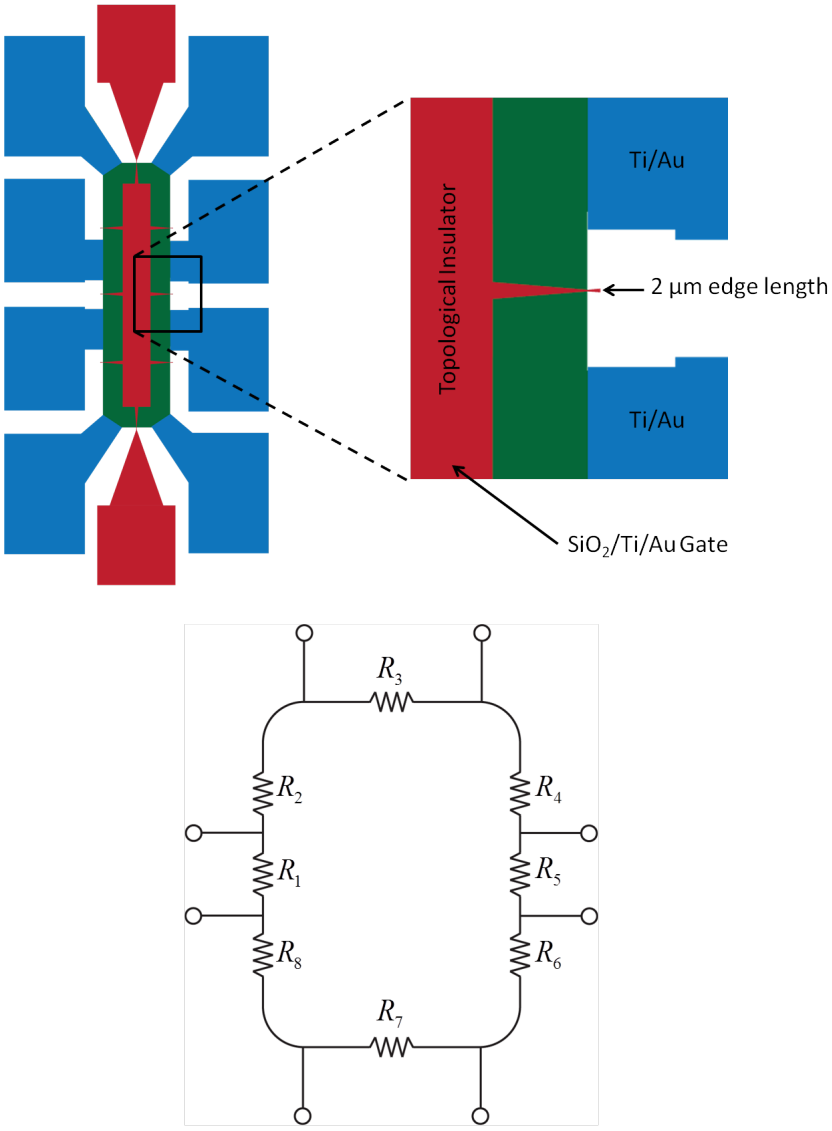

Figure 5.2.2: Schematic of QSH edge devices. Large ohmic contacts (blue) were made by depositing Ti/Au on a sample with a buried HgCdTe quantum well. By gating very small regions of the edge, we can create a series of well-defined QSH edges, each 2 μm in length, to study the variability of conductance. Also provided is an equivalent resistor network for the sample. Each ideal QSH edge has a resistance of R_k.

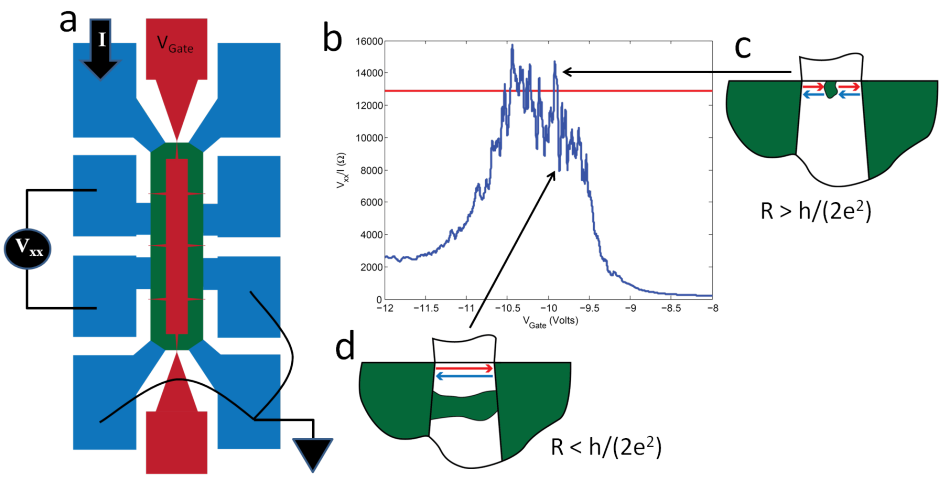

Figure 5.2.3: Transverse resistance in the quantum spin Hall effect. **b**, Resistance shown in **a** plotted versus gate voltage. The red line corresponds to the expected value (assuming ideal QSH edges) of $R_k/2$. Puddles can create parallel channels to increase conductance, and time-reversal breaking impurities can create backscattering to decrease conductance.

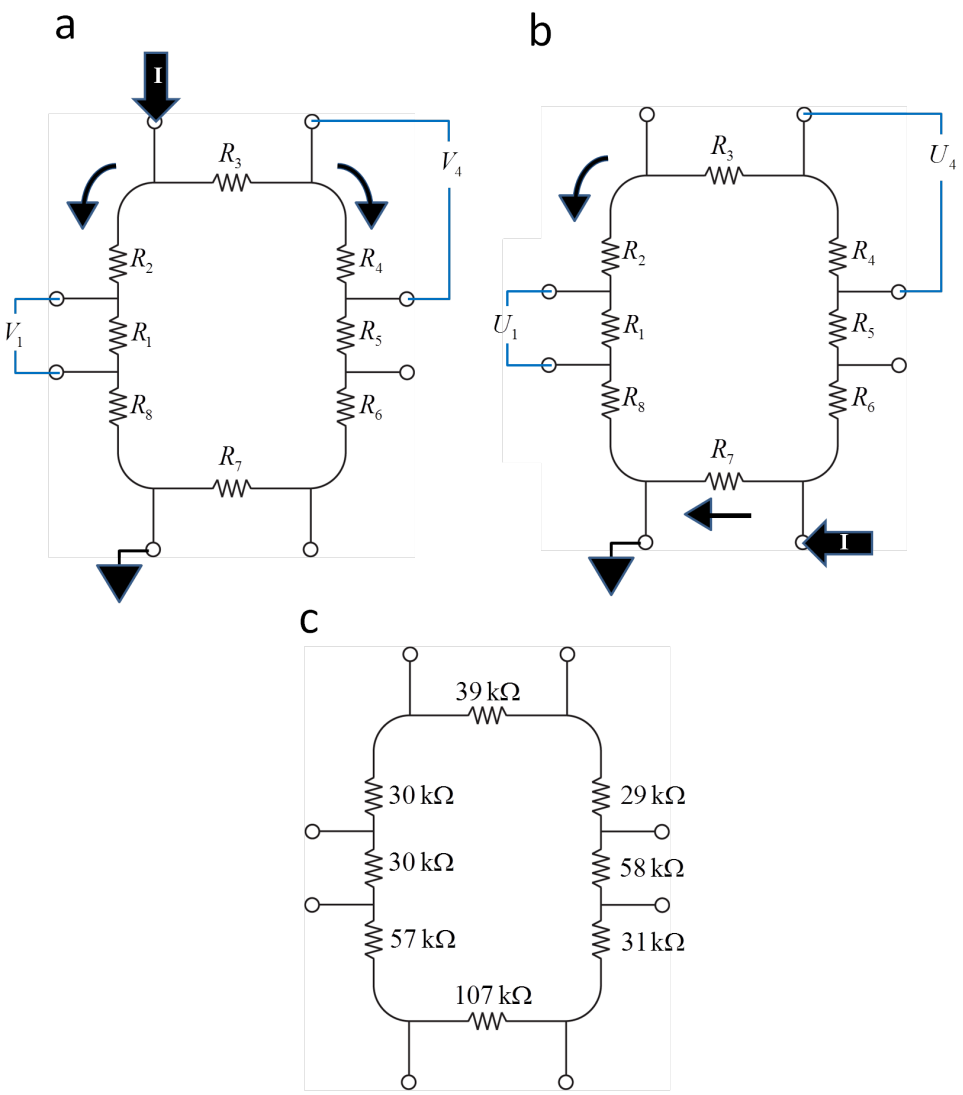

Figure 5.2.4: a, b, Two measurement configurations that allow us to extract the resistance R_1. **c,** The resulting QSH edge resistances for eight 2 μm edges.

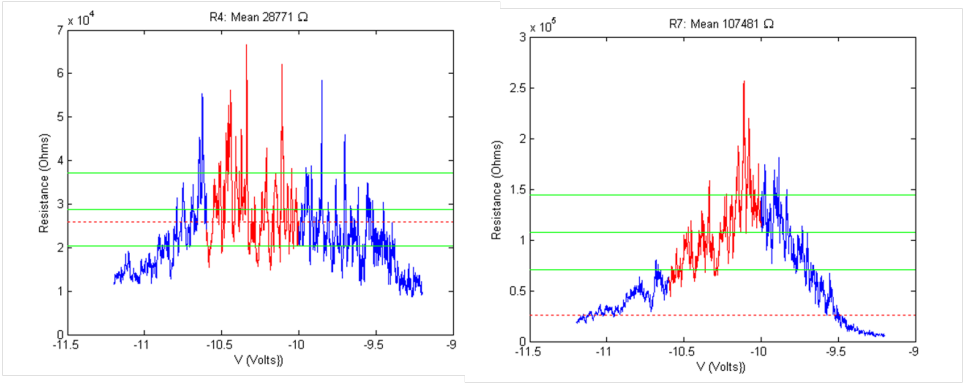

Figure 5.2.5: QSH Edge Resistances versus Gate voltage for resistors 4 (left) and 7 (right) in Fig. 5.2.4. The red region is the region determined to be the center of the gap in gate voltage, and the green lines indicate the mean of the red data along with the standard deviation (plus and minus). The dashed red line indicates the conductance expected for an ideal QSH edge.

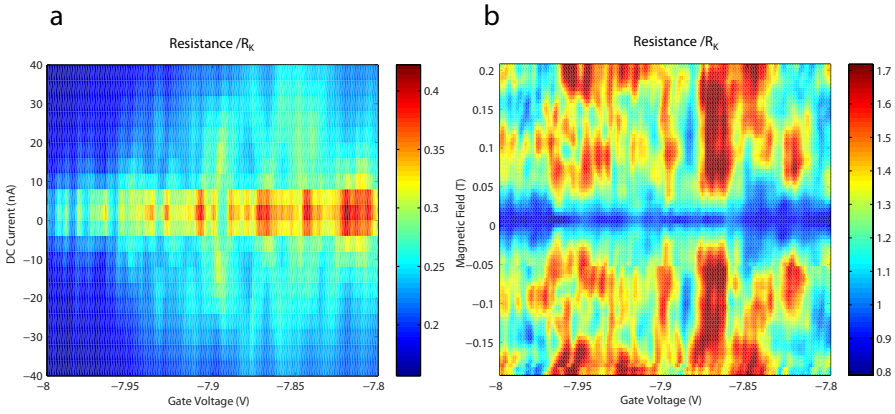

Figure 5.3.1: Gate-dependent QSH resistances versus DC current bias (**a**) and magnetic field (**b**). Color scales are resistances in units of R_k. The expected resistance (given the contact topology and assuming ideal QSH edges) for the plot on the left is 0.375 R_k and the expected resistance on the right is $0.5R_k$. No clear periodicity is seen versus B.

A

Fabrication Procedures

Here I'll briefly describe the fabrication recipes used to make samples measured as part of this thesis. This shouldn't be taken as an up-to-date reference. Look on the Yacoby group server for more current recipes.

Before processing any wafers, it is a good practice to clean the backside (using hot methanol and a cotton swab, for example). Cleaving can be done with a scriber, followed by brief sonication in trichloroethylene, acetone, and methanol (in that order).

A good strategy for spinning resist on small pieces is to glue the small piece on a larger wafer, and then spin the larger wafer with the small piece off-center. Using CrystalBond 555 to glue the small piece to the large piece works very reliably.

A.1 Photolithography

This process is sufficient for making patterns using using the positive tone Shipley resists. They are sufficient for defining regions to be etched, and provide resolutions on the order of 1 μm.

A.1.1 Shipley Resist Photolithography for Etching

Use this process to identify regions of a wafer from which you want to remove material. It will not provide enough undercut for liftoff processes.

1. Spin Shipley 1805 at 5000 RPM for 40 seconds.
2. Bake the wafer at 80 C for 5 or so minutes.
3. Expose for 4 or so seconds on MJB4 in constant power mode.
4. Develop the sample in MIF 319 (a TMAH developer) for 10 or so seconds.
5. Hard Bake the sample for a few minutes at 100 C. I've skipped this a few times with no ill effects for acid etching.

A.1.2 Shipley Resist Photolithography for Metal Deposition and Liftoff

This process creates good undercut but has less resolution than the standard recipe above.

1. Spin Shipley 1818 at 5000 RPM for 40 seconds.
2. Bake the wafer at 80 C for 5 or so minutes.
3. Expose for 8 seconds on MJB4 in constant power mode.
4. Soak sample in chlorobenzene for 4 minutes. Be sure to carefully dispose of the chlorinated solvent.
5. Develop the sample in MIF 319 (a TMAH developer) for 2 minutes.

A.1.3 Image reversal (AZ514 IR)

This is a negative resist that works very well as a liftoff resist. The most sensitive step is a brief bake at 120 C, which should be done on a well-calibrated hotplate (ideally to within 1 degree Celsius). This is sadly too hot to use for HgTe samples.

1. Spin AZ5214 IR at 5000 RPM for 40 seconds.
2. Bake the wafer at 100 C for 45 seconds.

3. Expose for 0.4 seconds on MJB4 in constant power mode.
4. Bake the sample for 55 seconds at 120 $\pm$ 1 C (very sensitive to temperature).
5. Flood expose the sample (no mask) for 45 seconds. This isn't sensitive
6. Develop the sample in AZ 726 IR for 20 seconds.

If features don't seem fully developed, or if the undercut appears inadequate, repeat the flood exposure and developing steps one more time.

A.2 Electron Beam Lithography

These are the parameters for the Elionix 7000. Writing with the Elionix F-125 is strictly easier (600 μm write fields for 20 nm features works well).

A.2.1 Small Gates on GaAs Samples (Normal Evaporation): Elionix 7000

1. Spin PMMA 950K A4 or A2 at 5000 RPM for 40s.
2. Bake at 180 C for $>$ 5 minutes.
3. Write small features, then large features:
   (a) Smallest features (<1 μm): write at 100 pA with a 75 μm chip size and 60,000 dots.
   (b) Larger features (bewteen 1 and 10 μm): write at 2 nA with 600 μm chip size and 60,000 dots.
4. Develop in MIBK/IPA (1:3) at 0 C (ice bath) for 1 minute

A.2.2 SETs (Angle Evaporation): Elionix 7000

1. Spin MMA(8.5)MAA diluted 6% in Ethyl Lactate at 5000 RPM for 40s (120 - 150 nm)
2. Bake at 180 C for $>$ 5 minutes.
3. Spin PMMA 950K A4 at 4000 RPM for 40s (about 200 nm)

4. Bake at 180 C for $>$ 5 minutes.
5. Write at 50 pA with a 75 μm chip size and 60,000 dots. With these settings, doses of about 0.75μs expose both layers of resist, and doses of about 0.2μs expose just the lower layer.
6. Develop in MIBK/IPA (1:3) at 0 C (ice bath) for 1 minute

A.2.3 Low Voltage Process for HgTe: Raith

1. Spin PMMA 950K A4 at 4000 RPM for 40s.
2. Bake at 80 C (!) for $>$ 10 minutes.
3. Write small features, then large features:
   (a) 3 kV accelerating voltage
   (b) 30 μ aperture for 130 pA, 60 μm aperture for 650 pA.
   (c) Working distance of about 11 mm
   (d) Dose: 80 μC/cm^2
4. Develop in MIBK/IPA (1:3) at 0 C (ice bath) for 1 minute

A.3 Removing Material (Etching, Polishing, and Milling)

A.3.1 Phosphoric Acid Etch for GaAs

Use this to remove up to a few microns of material from the topside of a wafer after performing photolithography (typically with positive Shipley resist).

1. Mix H_3PO_4:H_2O_2:H_2O in a 1:1:25 ratio. A good amount is 4 mL of H_3PO_4, 4 mL of H_2O_2, and 100 mL of H_2O. Stir thoroughly, or the etch will not be uniform in time.
2. Swirl sample around in etchant. A typical rate is 180-200 nm/min, and you should shoot to eliminate the top donor layer in a symmetrically doped well. For asymmetrically doped wells, eliminate the 2DES layer.
3. To hit target, use the profilometer.
4. Rinse sample in H_2O.

A.3.2 Bromine/Methanol Etch for thinning wafers

This works on both GaAs and HgTe samples. We use it to thin samples down prior to evaporating metal on the back to make a backgate. Typically, a 100 μm sample is easy to handle while a 50 μm sample is challenging.

1. Process the top side of your sample completely. It is hard to do additional topside processing after thinning.
2. Prepare a second wafer (we use insulating GaAs) with annealed metal on the surface (easily bonded to). This should be larger in area than your sample.
3. Mount your wafer upside down (!) using crystal bond on a small piece of glass (ideally 2 x 2 inches or so). Take a tray, some cleanroom wipes, and a large glass piece (8 x 8 inches or so) into a plastic hood.
4. Add bromine to methanol to get a final solution of 10% bromine. This should be done in a plastic hood after clearing it with any safety controllers. It is a very dangerous and pungent mixture.
5. Place a cleanroom wipe on the large glass piece, then pour a small amount of the bromine mixture on the wipe. Rub your sample in a figure 8 on the soaked region for about 30 seconds. Wash it off with methanol, then check the thickness. (This can be done using the z micrometer on an optical microscope). Use the measured difference to calibrate your rate and continue until you hit your target thickness (we've been able to handle 100 μm, and we've failed to handle 40 μm).
6. Clean up carefully.

A.3.3 Reactive Ion Etching for HgTe: Nexx RIE

This is used to define mesas and improve ohmic contacts in our HgCdTe materials. It should follow photolithography with Shipley resist.

1. Start the recipe `burnin.rcp` for 20 minutes immediately. This can be done while preparing your sample.
2. Next run the recipe `ch4h2ar.rcp` for 5 minutes without your sample

3. Attach your sample with cooling paste to the holder, and run `ch4h2ar.rcp` once more. The rate should be about 1.5 nm/sec. The mesa etch should be deeper than the mesa depth (this isn't true for GaAs), and the ohmic etch should be about 10 nm shallower than the mesa depth.

4. Remove cooling paste with IPA.

5. Remove resist with acetone, then methanol. Ultrasonic cleaning may be necessary to cleanly remove all resist.

A.4 Metal Evaporation

These are all quite straightforward.

1. GaAs ohmics: 7 nm Ni, $x/3$ nm Ge, $2x/3$ nm Au, 20 nm Ni, 100 nm Au. x is the depth of the 2DES in nm. After liftoff, anneal at 120C (1 min), 340C (1 min), ramp from 340C to 460C in 30 sec, then hold at 460C for 2 sec before stopping the heat.

2. GaAs small gates: 30 nm PdAu

3. GaAs large gates (climbing over mesa edge): 20 nm Ti, $x + 10$ nm Au

4. SETs: 20 nm Al for the first evaporation at an angle of 35° from the normal. Oxidize with dry air for 6 minutes at a pressure of 2-3 torr. Turn by 90 degrees, then evaporate another 40 nm of Al. Evaporating the island before legs is somewhat more reliable (minimizes metal-metal shadowing).

B

Fridge Wiring

All of the measurements reported in this thesis were carried out in a commercially available dilution refrigerator (Oxford Instruments MX 400), with a base temperature of 10 mK and 400 μW of cooling power at 100 mK. With the as-sold wiring, electrons in a sample will be cooled to roughly 70 mK. To lower this to 20 mK, we added Thermocoax lines (part 1NcAc05) from room temperature down to the mixing chamber. At the 1K stage, the cold plate, and the mixing chamber, these lines were broken out to thermalize the inner conductor. The boxes used to filter these wires consist of copper cases with sapphire plates (Fig. B.1c shows a version with a diamond film instead of sapphire). The inner conductors of the coaxial lines are connected to meandering gold lines evaporated on the sapphire plates. At the still plate, the coaxial lines are pressed against a thermally anchored copper mount.

To thermally anchor the sample to the mixing chamber, a silver coldfinger with three thin rods (to minimize eddy current heating) was used. The silver was vacuum brazed to form joints, and screwed in tightly to the mixing chamber with brass screws. For mechanical support, two copper plates were added to the sides. High conductivity

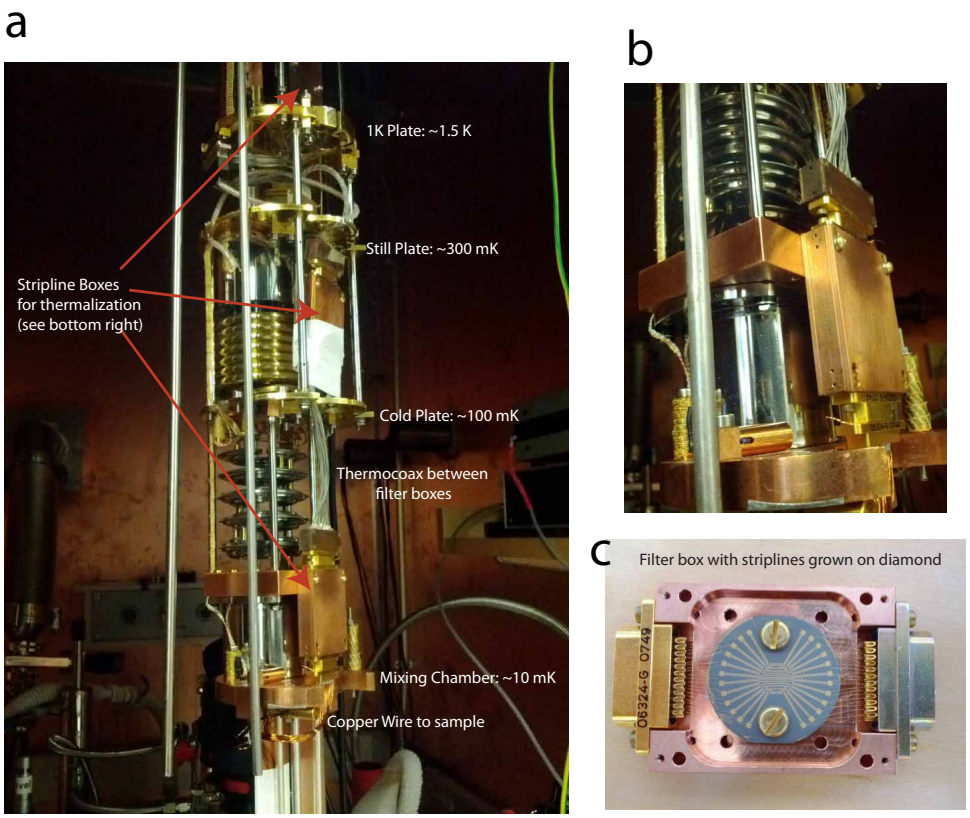

Figure B.1: Wiring of the fridge.

copper wires connect the cold wires at the mixing chamber to the sample (Figure B.2).

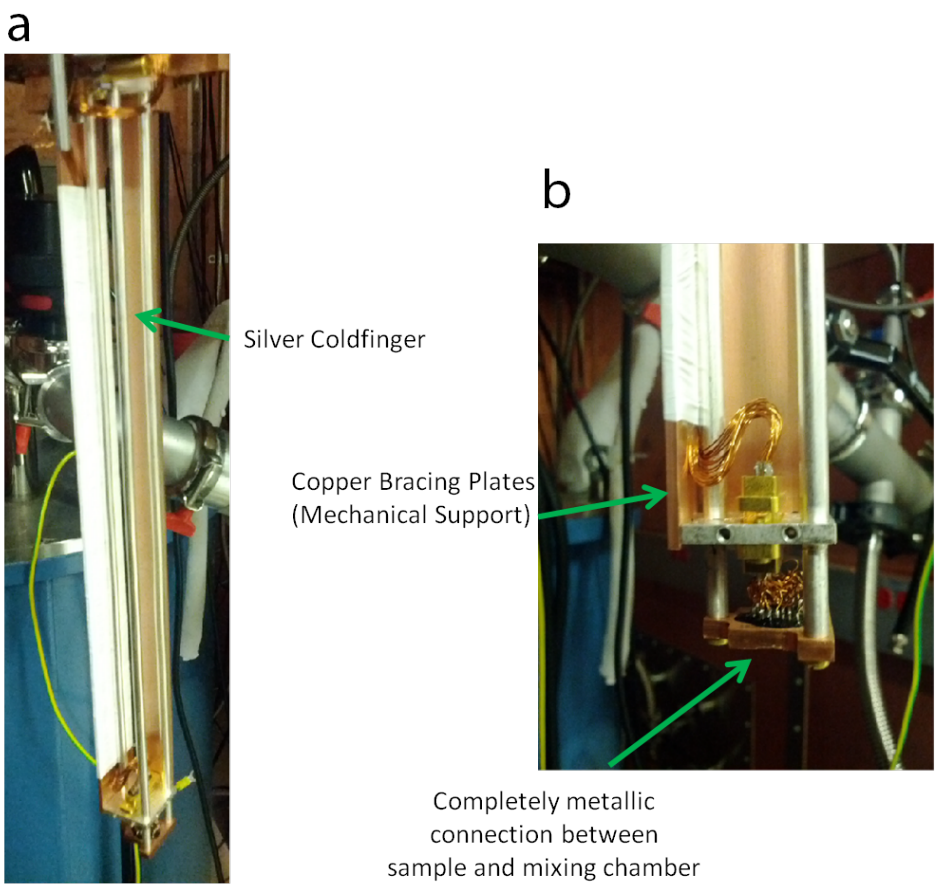

Figure B.2: Coldfinger

C

Special Measure

Special Measure provides a simple frontend for MATLAB's instrument control toolbox, allowing users to quickly set up flexible scans through parameter space with high degrees of control. This section is borrowed from the online Wiki on April 17, 2012, and shouldn't be used as primary documentation. (http://code.google.com/p/special-measure/wiki/SpecialMeasure).

Each hardware device is represented by an instrument (not to be confused with MATLAB instrument objects) that containes information about how to control it and what channels (see below) it provides. This information roughly corresponds to the hardcoded instrument drivers and channel array in Labview SM.

The channel concept is very similar to that of Labview SM - each channel represents some parameter, input or output value of an instrument. In most cases, it will be some physical quantity. There is currently no distinction between write and read channels. All channels should support a read operation, but it is up to the user to make sure that channels that do not support write operations (typically acquisition devices) are not used as set channels. Writable channels should always accept and return a single double, but read-only channels can also return matrices of arbitrary dimension - e.g. a

vector representing a complete scan line. Writable channels can be self ramping, in which case its variable can be ramped by the corresponding instrument. If available, this feature is always used to set channel values (function `smset`), and can also be used for measurements.

Information about instruments, channels (i.e. the rack) and other configuration is stored in the global struct `smdata`. Channels and instruments are stored in the struct array `smdata.channels` and `smdata.inst`. Major changes to smdata.inst are only required when adding new instruments or updating drivers, but it may occasionally be necessary to change certain instrument parameters, such as the data dimension for read channels.

Internally, channels and instruments are identified by their indices to the struct arrays `smdata.inst` and `smdata.channels`. These indices (printed at the beginning of each line by `smprintchannels` and `smprintinst` can also be used to specify channels and instruments in function arguments, including scan definition. Alternatively, channel and instruments names can be used. Lists of names can be given as a char arrays or cell vectors of strings. The conversion from names to indices is typically done with `smchanlookup` and `sminstlookup`. Channel names should always be unique. Instruments can be called by their instrument type identifier (`smdata.inst().device`, e.g. SR830) if there is only one such instrument in the rack, or an optional name, which should be unique amongst instrument types and names. Instruments with a name should generally be called by that name.

C.1 Pseudocode

- Set constant channels
- Call configfn; `scan=configfn(i).fn(scan,configfn(i).args:);`
- Main loop
  - For loops needing update (outer first)
    * Set values and/or program ramps
    * call prefn
    * wait
    * trigger ramped channels if needed

    - end
    - For loops needing readout (inner first)
        * read data
        * call postfn
        * apply procfn
        * display data
        * save data if needed
        * call datafn
    - end
- end
- Save data.

References

[1] C. Altimiras, H. le Sueur, U. Gennser, A. Cavanna, D. Mailly, and F. Pierre. Non-equilibrium edge-channel spectroscopy in the integer quantum hall regime. *Nature Physics*, 6:34–39, 2009.

[2] C. Altimiras, H. le Sueur, U. Gennser, A. Cavanna, D. Mailly, and F. Pierre. Tuning energy relaxation along quantum hall channels. *Phys. Rev. Lett.*, 105(22): 226804, Nov 2010. doi: 10.1103/PhysRevLett.105.226804.

[3] C. Altimiras, H. le Sueur, U. Gennser, A. Anthore, A. Cavanna, D. Mailly, and F. Pierre. Chargeless heat transport in the fractional quantum hall regime, feb 2012. URL `http://arxiv.org/abs/1202.6300v1`.

[4] R. C. Ashoori, H. L. Stormer, L. N. Pfeiffer, K. W. Baldwin, and K. West. Edge magnetoplasmons in the time domain. *Phys. Rev. B*, 45(7):3894–3897, Feb 1992. doi: 10.1103/PhysRevB.45.3894.

[5] M. Baraban, G. Zikos, N. Bonesteel, and S. H. Simon. Numerical analysis of quasiholes of the moore-read wave function. *Phys. Rev. Lett.*, 103:076801, Aug 2009. doi: 10.1103/PhysRevLett.103.076801. URL `http://link.aps.org/doi/10.1103/PhysRevLett.103.076801`.

[6] C. W. J. Beenakker. Theory of coulomb-blockade oscillations in the conductance of a quantum dot. *Phys. Rev. B*, 44:1646–1656, Jul 1991. doi: 10.1103/PhysRevB.44.1646. URL `http://link.aps.org/doi/10.1103/PhysRevB.44.1646`.

[7] G. Ben-Shach, C. R. Laumann, A. Yacoby, and B. I. Halperin. *In Preparation*.

[8] B. Andrei Bernevig, Taylor L. Hughes, and Shou-Cheng Zhang. Quantum spin hall effect and topological phase transition in hgte quantum wells. *Science*, 314 (5806):1757–1761, 2006. doi: 10.1126/science.1133734. URL `http://www.sciencemag.org/content/314/5806/1757.abstract`.

[9] A. Bid, N. Ofek, H. Inoue, M. Heiblum, C.L. Kane, V. Umansky, and D. Mahalu. Observation of neutral modes in the fractional quantum hall regime. *Nature*, 466:585–590, July 2010.

[10] Aveek Bid, N. Ofek, M. Heiblum, V. Umansky, and D. Mahalu. Shot noise and charge at the 2/3 composite fractional quantum hall state. *Phys. Rev. Lett.*, 103 (23):236802, Dec 2009. doi: 10.1103/PhysRevLett.103.236802.

[11] Waheb Bishara, Parsa Bonderson, Chetan Nayak, Kirill Shtengel, and J. K. Slingerland. Interferometric signature of non-abelian anyons. *Phys. Rev. B*, 80 (15):155303, Oct 2009. doi: 10.1103/PhysRevB.80.155303.

[12] Parsa Bonderson, Alexei Kitaev, and Kirill Shtengel. Detecting non-abelian statistics in the $\nu = 5/2$ fractional quantum hall state. *Phys. Rev. Lett.*, 96(1): 016803, Jan 2006. doi: 10.1103/PhysRevLett.96.016803.

[13] Sergey Bravyi and Alexei Kitaev. Universal quantum computation with ideal clifford gates and noisy ancillas. *Phys. Rev. A*, 71:022316, Feb 2005. doi: 10.1103/PhysRevA.71.022316. URL http://link.aps.org/doi/10.1103/PhysRevA.71.022316.

[14] Meng Cheng, Roman M. Lutchyn, Victor Galitski, and S. Das Sarma. Splitting of majorana-fermion modes due to intervortex tunneling in a $p_x + ip_y$ superconductor. *Phys. Rev. Lett.*, 103:107001, Aug 2009. doi: 10.1103/PhysRevLett.103.107001. URL http://link.aps.org/doi/10.1103/PhysRevLett.103.107001.

[15] D. B. Chklovskii, B. I. Shklovskii, and L. I. Glazman. Electrostatics of edge channels. *Phys. Rev. B*, 46(7):4026–4034, Aug 1992. doi: 10.1103/PhysRevB.46.4026.

[16] H. C. Choi, W. Kang, S. Das Sarma, L. N. Pfeiffer, and K. W. West. Activation gaps of fractional quantum hall effect in the second landau level. *Phys. Rev. B*, 77 (8):081301, Feb 2008. doi: 10.1103/PhysRevB.77.081301.

[17] Lynda Cockins, Yoichi Miyahara, Steven D. Bennett, Aashish A. Clerk, Sergei Studenikin, Philip Poole, Andrew Sachrajda, and Peter Grutter. Energy levels of few-electron quantum dots imaged and characterized by atomic force microscopy. *Proceedings of the National Academy of Sciences*, 107(21):9496–9501, 2010. doi: 10.1073/pnas.0912716107. URL http://www.pnas.org/content/107/21/9496.abstract.

[18] N. R. Cooper and Ady Stern. Observable bulk signatures of non-abelian quantum hall states. *Phys. Rev. Lett.*, 102:176807, Apr 2009. doi: 10.1103/PhysRevLett.102.176807. URL http://link.aps.org/doi/10.1103/PhysRevLett.102.176807.

[19] Sankar Das Sarma, Michael Freedman, and Chetan Nayak. Topologically protected qubits from a possible non-abelian fractional quantum hall state. *Phys. Rev. Lett.*, 94(16):166802, Apr 2005. doi: 10.1103/PhysRevLett.94.166802.

[20] C. R. Dean, B. A. Piot, P. Hayden, S. Das Sarma, G. Gervais, L. N. Pfeiffer, and K. W. West. Intrinsic gap of the $\nu = 5/2$ fractional quantum hall state. *Phys. Rev. Lett.*, 100(14):146803, Apr 2008. doi: 10.1103/PhysRevLett.100.146803.

[21] P.A.M. Dirac. Quantised singularities in teh electromagnetic field. *Proceedings of the Royal Society of London. Series A, Containing Papers of a Mathematical and Physical Character*, 133:60–72, 1931.

[22] M. Dolev, M. Heiblum, V. Umansky, A. Stern, and D. Mahalu. Observation of a quarter of an electron charge at the $\nu = 5/2$ quantum hall state. *Nature*, 452 (7189):829–834, 2008.

[23] M. Dolev, Y. Gross, Y. C. Chung, M. Heiblum, V. Umansky, and D. Mahalu. Dependence of the tunneling quasiparticle charge determined via shot noise measurements on the tunneling barrier and energetics. *Phys. Rev. B*, 81(16): 161303, Apr 2010. doi: 10.1103/PhysRevB.81.161303.

[24] M. Dolev, Y. Gross, R. Sabo, I. Gurman, M. Heiblum, V. Umansky, and D. Mahalu. Characterizing neutral modes of fractional states in the second landau level. *Phys. Rev. Lett.*, 107:036805, Jul 2011. doi: 10.1103/PhysRevLett.107.036805. URL `http://link.aps.org/doi/10.1103/PhysRevLett.107.036805`.

[25] A. L. Efros, F. G. Pikus, and V. G. Burnett. Density of states of a two-dimensional electron gas in a long-range random potential. *Phys. Rev. B*, 47:2233–2243, Jan 1993. doi: 10.1103/PhysRevB.47.2233. URL `http://link.aps.org/doi/10.1103/PhysRevB.47.2233`.

[26] J. P. Eisenstein, L. N. Pfeiffer, and K. W. West. Compressibility of the two-dimensional electron gas: Measurements of the zero-field exchange energy and fractional quantum hall gap. *Phys. Rev. B*, 50(3):1760–1778, Jul 1994. doi: 10.1103/PhysRevB.50.1760.

[27] S.M. Girvin and R.E. Prange. *The Quantum Hall Effect*. Springer, 1987.

[28] G. Granger, J. P. Eisenstein, and J. L. Reno. Observation of chiral heat transport in the quantum hall regime. *Phys. Rev. Lett.*, 102(8):086803, Feb 2009. doi: 10.1103/PhysRevLett.102.086803.

[29] M. Huber, M. Grayson, M. Rother, W. Biberacher, W. Wegscheider, and G. Abstreiter. Structure of a single sharp quantum hall edge probed by momentum-resolved tunneling. *Phys. Rev. Lett.*, 94(1):016805, Jan 2005. doi: 10.1103/PhysRevLett.94.016805.

[30] S. W. Hwang, D. C. Tsui, and M. Shayegan. Experimental evidence for finite-width edge channels in integer and fractional quantum hall effects. *Phys. Rev. B*, 48(11):8161–8165, Sep 1993. doi: 10.1103/PhysRevB.48.8161.

[31] S. Ilani, A. Yacoby, D. Mahalu, and Hadas Shtrikman. Microscopic structure of the metal-insulator transition in two dimensions. *Science*, 292(5520): 1354–1357, 2001. doi: 10.1126/science.1058645.

[32] S. Ilani, J. Martin, E. Teitelbaum, JH Smet, D. Mahalu, V. Umansky, and A. Yacoby. The microscopic nature of localization in the quantum hall effect. *Nature*, 427(6972):328, 2004.

[33] A. C. Johnson, J. R. Petta, J. M. Taylor, A. Yacoby, M. D. Lukin, C. M. Marcus, M. P. Hanson, and A. C. Gossard. Triplet-singlet spin relaxation via nuclei in a double quantum dot. *Nature*, 435(7044):925–928, June 2005. ISSN 0028-0836. URL `http://dx.doi.org/10.1038/nature03815`.

[34] C. L. Kane and Matthew P. A. Fisher. Quantized thermal transport in the fractional quantum hall effect. *Phys. Rev. B*, 55(23):15832–15837, Jun 1997. doi: 10.1103/PhysRevB.55.15832.

[35] C. L. Kane, Matthew P. A. Fisher, and J. Polchinski. Randomness at the edge: Theory of quantum hall transport at filling $\nu = 2/3$. *Phys. Rev. Lett.*, 72(26): 4129–4132, Jun 1994. doi: 10.1103/PhysRevLett.72.4129.

[36] Markus König, Steffen Wiedmann, Christoph Brüne, Andreas Roth, Hartmut Buhmann, Laurens W. Molenkamp, Xiao-Liang Qi, and Shou-Cheng Zhang. Quantum spin hall insulator state in hgte quantum wells. *Science*, 318(5851): 766–770, 2007. doi: 10.1126/science.1148047. URL `http://www.sciencemag.org/content/318/5851/766.abstract`.

[37] Markus König, Hartmut Buhmann, Laurens W. Molenkamp, Taylor Hughes, Chao-Xing Liu, Xiao-Liang Qi, and Shou-Cheng Zhang. The quantum spin hall effect: Theory and experiment. *Journal of the Physical Society of Japan*, 77(3): 031007, 2008. doi: 10.1143/JPSJ.77.031007. URL `http://jpsj.ipap.jp/link?JPSJ/77/031007/`.

[38] L. P. Kouwenhoven, B. J. van Wees, N. C. van der Vaart, C. J. P. M. Harmans, C. E. Timmering, and C. T. Foxon. Selective population and detection of edge

channels in the fractional quantum hall regime. *Phys. Rev. Lett.*, 64(6):685–688, Feb 1990. doi: 10.1103/PhysRevLett.64.685.

[39] R. B. Laughlin. Anomalous quantum hall effect: An incompressible quantum fluid with fractionally charged excitations. *Phys. Rev. Lett.*, 50:1395–1398, May 1983. doi: 10.1103/PhysRevLett.50.1395. URL http://link.aps.org/doi/10.1103/PhysRevLett.50.1395.

[40] Sung-Sik Lee, Shinsei Ryu, Chetan Nayak, and Matthew P. A. Fisher. Particle-hole symmetry and the $\nu = \frac{5}{2}$ quantum hall state. *Phys. Rev. Lett.*, 99: 236807, Dec 2007. doi: 10.1103/PhysRevLett.99.236807. URL http://link.aps.org/doi/10.1103/PhysRevLett.99.236807.

[41] Michael Levin, Bertrand I. Halperin, and Bernd Rosenow. Particle-hole symmetry and the pfaffian state. *Phys. Rev. Lett.*, 99:236806, Dec 2007. doi: 10.1103/PhysRevLett.99.236806. URL http://link.aps.org/doi/10.1103/PhysRevLett.99.236806.

[42] A. H. MacDonald. Edge states in the fractional-quantum-hall-effect regime. *Phys. Rev. Lett.*, 64(2):220–223, Jan 1990. doi: 10.1103/PhysRevLett.64.220.

[43] Joseph Maciejko, Taylor L. Hughes, and Shou-Cheng Zhang. The quantum spin hall effect. *Annual Review of Condensed Matter Physics*, 2(1):31–53, 2011. doi: 10.1146/annurev-conmatphys-062910-140538. URL http://www.annualreviews.org/doi/abs/10.1146/annurev-conmatphys-062910-140538.

[44] J. Martin, S. Ilani, B. Verdene, J. Smet, V. Umansky, D. Mahalu, D. Schuh, G. Abstreiter, and A. Yacoby. Localization of fractionally charged quasi-particles. *Science*, 305(5686):980, 2004.

[45] D. T. McClure, W. Chang, C. M. Marcus, L. N. Pfeiffer, and K. W. West. Fabry-perot interferometry with fractional charges. *cond-mat.mes-hall*, arXiv:1112.0538v1 [cond-mat.mes-hall], December 2012.

[46] G. Moore and N. Read. Nonabelions in the fractional quantum hall effect. *Nuclear Physics B*, 360(2-3):362–396, 1991.

[47] Chetan Nayak, Steven H. Simon, Ady Stern, Michael Freedman, and Sankar Das Sarma. Non-abelian anyons and topological quantum computation. *Rev. Mod. Phys.*, 80(3):1083–1159, Sep 2008. doi: 10.1103/RevModPhys.80.1083.

[48] Michael Nielsen. *Quantum computation and quantum information*. Cambridge University Press, Cambridge New York, 2010. ISBN 9781107002173.

[49] Nissim Ofek, Aveek Bid, Moty Heiblum, Ady Stern, Vladimir Umansky, and Diana Mahalu. Role of interactions in an electronic fabry perot interferometer operating in the quantum hall effect regime. *Proceedings of the National Academy of Sciences*, 107(12):5276–5281, 2010. doi: 10.1073/pnas.0912624107. URL http://www.pnas.org/content/107/12/5276.abstract.

[50] I.P. Radu, JB Miller, CM Marcus, MA Kastner, LN Pfeiffer, and KW West. Quasi-particle properties from tunneling in the $\nu = 5/2$ fractional quantum hall state. *Science*, 320(5878):899, 2008.

[51] Andreas Roth, Christoph Brüne, Hartmut Buhmann, Laurens W. Molenkamp, Joseph Maciejko, Xiao-Liang Qi, and Shou-Cheng Zhang. Nonlocal transport in the quantum spin hall state. *Science*, 325(5938):294–297, 2009. doi: 10.1126/science.1174736. URL http://www.sciencemag.org/content/325/5938/294.abstract.

[52] Ady Stern and Bertrand I. Halperin. Proposed experiments to probe the non-abelian $\nu = 5/2$ quantum hall state. *Phys. Rev. Lett.*, 96(1):016802, Jan 2006. doi: 10.1103/PhysRevLett.96.016802.

[53] H. L. Stormer, A. Chang, D. C. Tsui, J. C. M. Hwang, A. C. Gossard, and W. Wiegmann. Fractional quantization of the hall effect. *Phys. Rev. Lett.*, 50: 1953–1956, Jun 1983. doi: 10.1103/PhysRevLett.50.1953. URL http://link.aps.org/doi/10.1103/PhysRevLett.50.1953.

[54] S. Takei, M. Milletarì, and B. Rosenow. Nonequilibrium electron spectroscopy of luttinger liquids. *Phys. Rev. B*, 82:041306, Jul 2010. doi: 10.1103/PhysRevB.82.041306. URL http://link.aps.org/doi/10.1103/PhysRevB.82.041306.

[55] D. C. Tsui, H. L. Stormer, and A. C. Gossard. Two-dimensional magnetotransport in the extreme quantum limit. *Phys. Rev. Lett.*, 48:1559–1562, May 1982. doi: 10.1103/PhysRevLett.48.1559. URL http://link.aps.org/doi/10.1103/PhysRevLett.48.1559.

[56] B. J. van Wees, E. M. M. Willems, C. J. P. M. Harmans, C. W. J. Beenakker, H. van Houten, J. G. Williamson, C. T. Foxon, and J. J. Harris. Anomalous integer quantum hall effect in the ballistic regime with quantum point contacts. *Phys. Rev. Lett.*, 62(10):1181–1184, Mar 1989. doi: 10.1103/PhysRevLett.62.1181.

[57] V. Venkatachalam, S. Hart, L. Pfeiffer, K. West, and A. Yacoby. Local thermometry of neutral modes on the quantum hall edge, Feb. 2012. URL http://arxiv.org/abs/1202.6681.

[58] Vivek Venkatachalam, Amir Yacoby, Loren Pfeiffer, and Ken West. Local charge of the $\nu = 5/2$ fractional quantum hall state. *Nature*, 469(7329):185–188, January 2011. ISSN 0028-0836. URL http://dx.doi.org/10.1038/nature09680.

[59] X. G. Wen. Electrodynamical properties of gapless edge excitations in the fractional quantum hall states. *Phys. Rev. Lett.*, 64(18):2206–2209, Apr 1990. doi: 10.1103/PhysRevLett.64.2206.

[60] R. L. Willett, L. N. Pfeiffer, and K. W. West. Measurement of filling factor 5/2 quasiparticle interference with observation of charge e/4 and e/2 period oscillations. *Proceedings of the National Academy of Sciences*, 106(22):8853–8858, 2009. doi: 10.1073/pnas.0812599106. URL http://www.pnas.org/content/106/22/8853.abstract.

[61] A. Yacoby, H.F. Hess, T.A. Fulton, L. Pfeiffer, and K. West. Electrical imaging of the quantum hall state. *Solid State Communications*, 111:1–13, 1999.

[62] A. Zee. *Quantum field theory in a nutshell*. Princeton University Press, 2003. ISBN 9780691010199.

[63] Yiming Zhang, D. T. McClure, E. M. Levenson-Falk, C. M. Marcus, L. N. Pfeiffer, and K. W. West. Distinct signatures for coulomb blockade and aharonov-bohm interference in electronic fabry-perot interferometers. *Phys. Rev. B*, 79:241304, Jun 2009. doi: 10.1103/PhysRevB.79.241304. URL http://link.aps.org/doi/10.1103/PhysRevB.79.241304.

[64] N. B. Zhitenev, R. J. Haug, K. v. Klitzing, and K. Eberl. Time-resolved measurements of transport in edge channels. *Phys. Rev. Lett.*, 71(14):2292–2295, Oct 1993. doi: 10.1103/PhysRevLett.71.2292.

Colophon

This thesis was typeset using LaTeX, originally developed by Leslie Lamport and based on Donald Knuth's TeX. The body text is set in 11 point Arno Pro, designed by Robert Slimbach in the style of Venitian and Aldine book types, and issued by Adobe in 2007.
A template that can be used to format a PhD thesis with this look and feel is freely available online at `https://github.com/suchow/`.